

INFORMATION TO USERS

This manuscript has been reproduced from the microfilm master. UMI films the text directly from the original or copy submitted. Thus, some thesis and dissertation copies are in typewriter face, while others may be from any type of computer printer.

The quality of this reproduction is dependent upon the quality of the copy submitted. Broken or indistinct print, colored or poor quality illustrations and photographs, print bleedthrough, substandard margins, and improper alignment can adversely affect reproduction.

In the unlikely event that the author did not send UMI a complete manuscript and there are missing pages, these will be noted. Also, if unauthorized copyright material had to be removed, a note will indicate the deletion.

Oversize materials (e.g., maps, drawings, charts) are reproduced by sectioning the original, beginning at the upper left-hand corner and continuing from left to right in equal sections with small overlaps. Each original is also photographed in one exposure and is included in reduced form at the back of the book.

Photographs included in the original manuscript have been reproduced xerographically in this copy. Higher quality 6" x 9" black and white photographic prints are available for any photographs or illustrations appearing in this copy for an additional charge. Contact UMI directly to order.

UMI

A Bell & Howell Information Company
300 North Zeeb Road, Ann Arbor MI 48106-1346 USA
313/761-4700 800/521-0600

Analytic Shape Sensitivities and Approximations of Local and Global Airframe Buckling Constraints

by

Youngwon Shin

A dissertation submitted in partial fulfillment
of the requirements for the degree of

Doctor of Philosophy

University of Washington

1997

Approved by Eric Lindhe
(Co-Chairperson of Supervisory Committee)
[Signature]
(Co-Chairperson of Supervisory Committee)

Program Authorized
to Offer Degree Aeronautics and Astronautics

Date December 16, 1997

UMI Number: 9819301

UMI Microform 9819301
Copyright 1998, by UMI Company. All rights reserved.

**This microform edition is protected against unauthorized
copying under Title 17, United States Code.**

UMI
300 North Zeeb Road
Ann Arbor, MI 48103

In presenting this dissertation in partial fulfillment of the requirements for the Doctoral degree at the University of Washington, I agree that the Library shall make its copies freely available for inspection. I further agree that extensive copying of this dissertation is allowable only for scholarly purposes, consistent with "fair use" as prescribed in the U.S. Copyright Law. Request for copying or reproduction of this dissertation may be referred to University Microfilms, 1490 Eisenhower Place, P.O. Box 975, Ann Arbor, MI 48106, to whom the author has granted "the right to reproduce and sell (a) copies of the manuscript in microform and/or (b) printed copies of the manuscript made from microform."

Signature *Jeimyungwon*

Date December 16, 1997

University of Washington

Abstract

**Analytic Shape Sensitivities and Approximations of Local
and Global Airframe Buckling Constraints**

by Youngwon Shin

Co-Chairpersons of Supervisory Committee:

Professor Eli Livne

Professor Keith A. Holsapple

Department of Aeronautics and Astronautics

An examination of available shell finite elements suitable for buckling analysis of thin walled airframe structures leads to the selection of a simple, accurate, design-oriented element, which is, then, used with slight modifications to obtain explicit, closed form equations for the stiffness and geometric stiffness matrices. In turn, these equations are used to derive explicit expressions for the analytic sensitivities of the stiffness and geometric stiffness matrices with respect to shell shape design variables. With analytic shape sensitivities of structural matrices and corresponding buckling eigenvalues at hand, the resulting new computer capability makes it possible to construct buckling constraint approximations for Approximation-Concepts based structural synthesis, as well as to examine sources of numerical noise which might appear when parametric studies or finite difference sensitivities are carried out using existing FE codes. The simplicity of the shell

elements used and the elimination of the need to carry out numerical integration, lead to computational savings, especially when repetitive analyses have to be carried out during shape design optimization of typical airframes. The new capability is aimed at capturing both local and global modes of buckling failure with the same FE model. Sub-component interaction during buckling can, thus, be taken into account during shape optimization of wing and fuselage structures. Numerical tests involving isotropic and laminated plates, thin walled channel sections and a complete wing box of a typical fighter airplane demonstrate the effectiveness and accuracy of the new design-oriented capability. Also the reduced order eigensystem which takes modeshapes at the reference design variable as the basis vectors for the perturbed design is derived and compared to the Rayleigh Quotient approximation.

TABLE OF CONTENTS

List of Figures	iv
List of Tables	viii
Chapter 1: Introduction	1
1.1 Motivations	1
1.2 Organization	4
Chapter 2: Finite Element Equations For Structural Stability	6
Chapter 3: A Flat Shell Element	8
3.1 Shell Finite Elements	8
3.2 The Flat Shell Element	11
3.3 Bending Stiffness Matrix	13
3.3.1 Discrete Kirchhoff theory	13
3.3.2 Interpolations for Transverse Displacement and Normal Rotations	15
3.3.3 Applications of Shear Constraints	17
3.3.4 The Evaluations of the Stiffness Matrix and Consistent Load Vector	18
3.4 Membrane Stiffness Matrix	19
3.5 Constitutive Equations for Composite Layer	20
3.6 Geometric Stiffness Matrix	23
3.7 Transformation to Global Coordinates	25
Chapter 4: The Explicit Formulations of the Stiffness and Geometric Stiffness Matrices	29
4.1 Introduction	29
4.2 Stiffness Matrix	30
4.3 Geometric Stiffness Matrix	34
Chapter 5: Analytic Sensitivities	37
5.1 Introduction	37

5.2 Sensitivities of Static Displacement and Stresses	40
5.3 Sensitivities of Buckling Loads and Buckling Modeshapes	43
Chapter 6: Order Reduction and Approximations	47
6.1 Introduction	47
6.2 Reduced System of Equations	49
6.3 Selection of Eigenvectors	51
6.4 Approximations	52
6.4.1 Approximations based on analytic sensitivity	54
6.4.2 Order Reduction using the Approximate Eigensystem.	54
6.4.3 Rayleigh Quotient Approximations	55
Chapter 7: Numerical Results (Verification and Sensitivites)	58
7.1 Simply Supported Rectangular Plates with Uniform Compression	58
7.1.1 Isotropic Plates	61
7.1.2 Orthotropic Plates	82
7.1.3 Anisotropic Laminated Plates	88
7.2 Equilateral Triangular Plates under Uniform Compression	93
7.3 Skew Plates under Uniform Compression	100
7.3.1 Isotropic Skew Plates	101
7.3.2 Orthotropic and Anisotropic Laminated Skew Plates	111
7.4 Box Beam under Uniform Compression	116
7.5 Typical Fighter Wing	122
Chapter 8: Numerical Results (Order Reduction)	148
8.1 Simply supported rectangular plates under uniaxial compression	148
8.2 Typical Fighter Wing	156
Chapter 9: Conclusions	162
Bibliography	165
Appendix A Explicit Expressions for $[A]$, $[C_x]$ and $[C_y]$	174
Appendix B Transformation Matrix	178

Appendix C	Flow Chart	181
Appendix D	MATHEMATICA Code for Analytic Integrations	182

LIST OF FIGURES

3.1	Geometry and nodal parameters of element	12
3.2	Displacements and coordinates of the bending element	14
3.3	Rotations of coordinate system for a laminate	21
3.4	Geometry of the laminate	23
3.5	Local coordinate system	25
7.1	Rectangular plate subject to uniform compression	59
7.2	Finite element mesh configurations for rectangular plates	60
7.3	Mode shape for the first symmetric mode of a rectangular plate ($a/b = 1.2$)	66
7.4	Mode shape for the second symmetric mode of a rectangular plate ($a/b = 1.2$)	67
7.5	Mode shape for the third symmetric mode of a rectangular plate ($a/b = 1.2$)	68
7.6	Convergence of buckling load for rectangular plate under uniaxial compression ($a/b = 1.2$)	69
7.7	Convergence of buckling load sensitivity for rectangular plate under uniaxial compression ($a/b = 1.2$)	70
7.8	Normalized buckling load and sensitivity for the rectangular plate under uniaxial compression ($a/b = 1.2$)	71
7.9	The sensitivity of Buckling Load Coefficients for the rectangular plate under uniaxial compression ($b = 10$)	72
7.10	Convergence of buckling load and sensitivity for the rectangular plate under biaxial compression ($a/b = 1.2$)	74
7.11	Mode shape for the first symmetric mode of a rectangular plate ($a/b = 3.2$)	75
7.12	Mode shape for the second symmetric mode of a rectangular plate ($a/b = 3.2$)	76

7.13	Mode shape for the third symmetric mode of a rectangular plate ($a/b = 3.2$)	77
7.14	Convergence of buckling load and sensitivity for rectangular plate under uniaxial compression ($a/b = 3.2$)	80
7.15	Convergence of buckling load and sensitivity for rectangular plate under biaxial compression ($a/b = 3.2$)	81
7.16	Convergence of buckling load and sensitivity for the orthotropic square plate.	85
7.17	Convergence of buckling load and sensitivity for the orthotropic rectangular plate ($a/b = 3.0$).	87
7.18	Buckling load coefficient and sensitivity for the anisotropic rectangular plate under uniaxial force	91
7.19	Buckling load coefficient and sensitivity for the anisotropic rectangular plate under biaxial force	92
7.20	Simply Supported Triangular Plate subject to Uniform Compression	93
7.21	Finite Element mesh configuration for equilateral triangular plate.	95
7.22	Convergence of buckling load and sensitivity for triangular plate ($a = 1$.)	97
7.23	The sensitivity of buckling load for the equilateral triangular plate.	98
7.24	Mode shape for the critical mode of an equilateral triangular plate.	99
7.25	Skew plate subject to uniaxial compression	100
7.26	Finite element mesh configuration for the skew plate.	101
7.27	Buckling load coefficient and sensitivity for the isotropic skew plate	107
7.28	Buckling load coefficient and buckling mode for the isotropic skew plate	108
7.29	Mode shape (Mode A) for the critical mode of the isotropic skew plate ($\Psi = 30$).	109
7.30	Mode shape (Mode B) for the second mode of the isotropic skew plate ($\Psi = 30$).	110
7.31	Buckling load coefficient and sensitivity for the orthotropic skew plate	114
7.32	Buckling load coefficients and sensitivities for the anisotropic laminated skew	

plates	115
7.33 Box beam subject to uniform compression	116
7.34 Finite element mesh configuration for the box beam	119
7.35 Mode shape for the critical mode of the box beam.	120
7.36 Buckling load coefficient and sensitivity for the box beam	121
7.37 Planform for the typical fighter wing	131
7.38 Finite element mesh configuration for the typical fighter wing	132
7.39 Finite element mesh configuration in detail for the typical fighter wing	133
7.40 Variation of planform for the typical fighter wing	134
7.41 Deformed shape of the typical fighter wing under aerodynamic force (9G pull-up)	135
7.42 Wingtip trailing edge deformation and sensitivity for the typical fighter wing.	136
7.43 Stresses and sensitivities at the element 333 for the typical fighter wing.	137
7.44 Comparison of stress σ_x at the element 333 for the typical fighter wing.	138
7.45 Comparison of stress σ_y at the element 333 for the typical fighter wing.	139
7.46 Comparison of stress τ_{xy} at the element 333 for the typical fighter wing.	140
7.47 Mode shape (Mode A) for the critical mode of the wing ($\alpha = 35.125$).	141
7.48 Mode shape (Mode B) for the second mode of the wing ($\alpha = 35.125$).	142
7.49 Mode shape (Mode C) for the third mode of the wing ($\alpha = 35.125$).	143
7.50 Mode shape (Mode D) for the fourth mode of the wing ($\alpha = 35.125$).	144
7.51 Mode shape (Mode E) for the fifth mode of the wing ($\alpha = 35.125$).	145
7.52 Buckling load coefficients and sensitivities for the two lowest modes of the wing	146
7.53 Buckling load coefficients and modes for the wing	147
8.1 The buckling load coefficients from order reduction analysis for the rectangular	

plate.	151
8.2 The buckling load coefficients from order reduction analysis with first order approximation of system matrices for the rectangular plate.	155
8.3 The buckling load coefficients from order reduction analysis for the wing.	159
8.4 The buckling load coefficients from order reduction analysis with first order approximation of system matrices for the wing.	161

LIST OF TABLES

7.1 Buckling coefficients for rectangular plate under uniaxial compression ($a/b = 1.2$).	64
7.2 Buckling coefficient sensitivity for rectangular plate under uniaxial compression ($a/b = 1.2$)	65
7.3 Buckling load coefficients for rectangular plate under biaxial compression ($a/b = 1.2$)	73
7.4 Buckling coefficient sensitivity for rectangular plate under biaxial compression ($a/b = 1.2$)	73
7.5 Buckling load coefficient and sensitivity for rectangular plate under uniaxial compression ($a/b = 3.2$)	79
7.6 Buckling load coefficient and sensitivity for rectangular plate under biaxial compression ($a/b = 3.2$)	79
7.7 Buckling load for the orthotropic square plate.	84
7.8 Buckling load sensitivity for the orthotropic square plate.	84
7.9 Buckling load for the orthotropic rectangular plate ($a/b = 3.0$).	86
7.10 Buckling load sensitivity for the orthotropic rectangular plate ($a/b = 3.0$).	86
7.11 Material properties of DLP single layer.	89
7.12 Comparison of Buckling Loads for Anisotropic Composite Plates	89
7.13 Buckling Loads and Sensitivities for Anisotropic Composite Plates Under Uniaxial compression ($(30/-30)_{5,5}$)	90
7.14 Buckling Loads and Sensitivities for Anisotropic Composite Plates Under Biaxial Compression ($(30/-30)_{5,5}$)	90
7.15 Critical buckling load and sensitivity for the equilateral triangular plate ($a = 1.$)	96

7.16	Buckling Load coefficient k for clamped isotropic plates, $a/b = 1$	103
7.17	Buckling Load coefficient k for simply supported isotropic plates, $a/b = 1$	104
7.18	Buckling Coefficeient and Sensitivity for simply supported isotropic skewed plates, $a/b = 1$	106
7.19	Buckling Coefficeient and Sensitivity for simply supported orthotropic skewed plates ($a/b = 1$)	112
7.20	Buckling loads and sensitivity for simply supported laminated skewed plates ($a/b = 1$)	113
7.21	Buckling load coefficient and sensitivity for the box beam	118
7.22	Transver deflection at the trailing edge wing tip and sensitivity	123
7.23	Membrane stresses and sensitivities at gaussian points for element 338 ($\alpha = 35.125$)	124
7.24	Buckling load coefficients and sensitivity ($\alpha = 35.125$)	126
7.25	Comparison of λ between global and local analysis for sp1	128
7.26	Comparison of λ between global and local analysis for sp6	128
7.27	Buckling load coefficients and sensitivities for the first two critical modes	129
8.1	Comparison of Buckling Load and Sensitivity from order reduction for the rectangular plates	150
8.2	Comparison of buckling load from order reduction with first order approximations of system matrices for the rectangular plates (Fixed mode method).	154
8.3	Comparison of buckling load and sensitivity from order reduction for the wing	158
8.4	Comparison of Buckling Load from order reduction with first order approximations of system matrices for the wing (Fixed mode method).	160

ACKNOWLEDGMENTS

I am very much indebted to Professor Eli Livne and Keith A. Holsapple for their thoughtful guidance and unceasing support throughout this study. I wish to express gratefulness to Professors Kuen Lin and Albert S. Kobayashi for their valuable advice and suggestions. I also thanks to Yeonseok Jeong, Maenghyo Cho, Israel Navarro and Refung Lee at the University of Washington for their valuable discussions.

Finally, I wish to give my special thanks to my parents, my wife and children, Sang-jin and eun-a, for their patience and unbelievable support.

DEDICATION

To my wife, Okran

and parents

Chapter 1

Introduction

1.1 Motivations

Buckling of thin walled structures is one of the most important structural failure modes considered during the design synthesis of flight vehicles. Typically, in the case of conventional airframes, buckling analyses of skin and fuselage panels are carried out under the assumption that individual panels, whether flat or curved, buckle independently of each other. The edge boundary conditions for the buckling analysis of those individual panels are assumed to be simply supported. This represents a conservative approach necessitated by the uncertainty associated with precise simulation of the flexibility of edge supports contributed by the panel's connections to adjoining panels and the stringers, frames, ribs and spars which surround the panel.

In a typical evaluation of linear buckling constraints in the context of structural optimization, stress analysis of the entire airframe will be usually followed by buckling analyses of buckling-critical individual panels. The dependence of buckling constraints on sizing-type design variables can be complex and quite nonlinear, since the local variation of panel structural designs will affect not only the panels themselves, but also the stress distribution in the complete structure. The same happens during conceptual design when airframe shape design variables are considered when the shape of an aircraft is to be

synthesized. Variations of overall shape design variables such as wing sweep or aspect ratio affects not only the stress distribution under load, but also the shape of individual panels, as spars and ribs change positions. Panels which start by being buckling-critical at the outset of the design process might become non-critical, while other panels might become critical as the design evolves. Moreover, strong interactions among neighboring panels, or among panels and webs of supporting ribs and spars, can arise if a configuration changes shape significantly compared to its initial design. Therefore, it is highly desirable to have a design oriented analysis capability which includes automatic mesh generation and mesh variation as well as behavior sensitivities and approximations, and which can effectively track the modes of buckling failure during the sizing and/or shape optimization of airframes.

Numerous references published over the last thirty years address the problems of panel buckling optimization and the interplay between the local buckling optimization of individual panels and the global optimization of the complete airframe (HG91, SR78, SH79, SM82, MC83, HMR90, LP87, AHA92, BHW94, ESH92). However, research efforts to examine the significance of global buckling analysis in airframe structural optimization and which allow for sub-component interactions during buckling are scarce (RG93, RGS94), and are limited to sizing-type design variables and to structural configurations made of rectangular sub-components. Of course, any finite element based buckling analysis capability can be used for shape optimization if behavior sensitivities are calculated by finite differences or by semi-analytic differentiation. However, the computational cost and numerical problems associated with finite differences are well known (HG91) as are potential accuracy problems associated with the semi-analytic method. Research efforts to develop design oriented structural modeling techniques with

analytic shape sensitivities for airframe shape optimization have also been very scarce (LIV94, HA93, LL97), even though structural shape optimization is a well established technology and has been applied successfully to many design synthesis problems in the car, ship, machine part and civil engineering industries (BOT82, HG86, DI86, BB86, BOT94, HG91). In Ref. LM95 a design oriented skin buckling analysis for the shape optimization of wing structures was presented. It took into account the local and global effects of variations in panel design variables and included skin panels of general trapezoidal planform, but it was still limited to single panels simply supported on all edges.

The present research presents a finite element based design-oriented airframe buckling analysis capable of predicting buckling modes involving interactions among sub-components as well as buckling of single stiffened panels with geometric configurations made of general trapezoidal segments. While this type of *analysis* can be carried out today with general purpose finite element codes (SK92), the new capability presented here includes *sensitivities* of buckling constraints with respect to panel and overall shape design variables which are obtained *analytically*.

Careful selection of the shell elements used makes it possible to obtain stiffness and geometric stiffness matrices, as well as their sensitivities with respect to shape, in closed analytical form and without the use of numerical quadrature. There are significant computational gains associated with the increased speed when element matrices are calculated using explicit closed form formulation. Test cases involving plates, thin walled channels, and a fighter wing structure are used to assess the computational effectiveness, accuracy and convergence of the buckling analysis; the successful capturing of buckling modes involving sub-component interactions; sources of numerical noise in parametric results; and the accuracy of the sensitivity analysis and associated approximations. The

resulting capability is constructed for integration into a Nonlinear Programming/Approximation Concepts (NLP/AC) based structural optimization (SCH81).

1.2 Organization

This study consists of two parts, the derivation of analytic shape sensitivity based on explicit formulations of system matrices, and the approximation of buckling load coefficient using order reduction technique.

At the beginning of each chapter, related works are reviewed. The finite element formulations for linear buckling analysis are derived based on the energy method in Chapter 2. Chapter 3 describes the derivation of a flat shell finite element for stress and buckling analysis. The element stiffness matrix is formulated by the superposition of a membrane element and discrete Kirchhoff plate bending element, and the global stiffness matrix is obtained from a local to global transformation. The resulting stresses are used to formulate the geometric stiffness matrix and buckling loads are obtained by solving a generalized eigenvalue problem.

In Chapter 4, explicit expressions of the stiffness and geometric stiffness matrices are derived in detail, they were obtained with the aid of symbolic computation using the program “MATHEMATICA”, which reduces the computing time and also make it possible to obtain analytic shape sensitivities. Analytic shape sensitivities for buckling loads, displacements and stresses are then derived in Chapter 5 by simply differentiating the closed form system matrices and transformation matrix.

Chapter 6 describes the order reduction method and approximations for buckling analysis in the optimization process, in which the repetitive evaluations are necessary. The

buckling loads for the modified structure can be effectively obtained with less cost by using a reduced eigensystem and several approximation methods are considered and studied here.

In Chapter 7, numerical results for the analytic shape sensitivities of buckling loads are presented and the interactions of sub components in the buckling analysis of complicated structure are discussed. Numerical results from the reduced eigensystem under change of design variables are presented and discussed in Chapter 8. Conclusions and recommendations for the future work are brought in Chapter 9.

Chapter 2

Finite Element Equation For Structural Stability

The energy functional for elasticity problems is given for a displacement formulation by (ZT91)

$$\pi(U) = \int_V \{\epsilon\}^T [E] \{\epsilon\} dV - \int_V \rho \{b\}^T \{U\} dV - \int_{\partial V} \{t\}^T \{U\} dV \quad (2.1)$$

where the strain $\{\epsilon\}$ is composed of linear and nonlinear strain

$$\{\epsilon\} = \{\epsilon^l\} + \{\epsilon^{nl}\} \quad (2.2)$$

$[E]$ is the constitutive matrix, and the vectors $\{b\}$ and $\{t\}$ represent body forces and surface tractions, respectively.

The strain-displacement relations are given as

$$\{\epsilon^l\} = [B_L] \{U\} \quad (2.3)$$

$$\{\epsilon^{nl}\} = [B_{NL}] \{U\} \quad (2.4)$$

According to the principal of minimum potential energy in the small displacement theory of elasticity neglecting nonlinear strain $\{\epsilon^{nl}\}$ (WASH82), the solution is obtained when the first variation of π is zero, giving the standard form

$$[K] \{U\} = \{F\} \quad (2.5)$$

where $[K]$, the small displacements stiffness matrix, is given by.

$$[K] = \int_V [B_L]^T [E] [B_L] dV \quad (2.6)$$

The second variation of the energy functional given in Eq. (2.1) can be written as

$$\delta^2 \pi = \frac{1}{2} \delta\{U\}^T [K_T] \delta\{U\} \quad (2.7)$$

where the tangential stiffness matrix has three parts:

$$[K_T] = [K] + [K_L] + [K_G] \quad (2.8)$$

The matrix $[K_L]$ is the stiffness matrix due to the large displacement and $[K_G]$ is known as the geometric stiffness matrix or initial stress matrix, and will be derived in the next chapter. If the effect of large displacement in $[K_T]$ is small, we can assume that $[K_L] = 0$.

According to the energy criterion (ZT91, CMP89), the critical load corresponding to bifurcation point buckling is obtained when the second variation of the general potential energy π is equal to zero. That condition is equivalent to the eigenvalue equation

$$\det\left[[K] + \lambda[K_G]\right] = 0 \quad (2.9)$$

The minimum value of λ is the critical loading parameter, that value is the ration of the critical load to the initial load considered.

Chapter 3

A Flat Shell Finite Element

3.1 Shell Finite Elements

A large number of structural systems in aerospace, mechanical and civil engineering are composed of thin shell components. The finite element method has proved to be a very powerful tool for structural analysis, and a great number of finite elements have been developed for the analysis of shells. A comprehensive review of the application of the finite element method to shell analysis can be found in references GR91 and YSL90.

There are two main approaches in the finite element analysis of shells, depending on whether the shell surface is approximated by curved or flat shell element. In the first approach, a curved shell is approximated by an assemblage of flat elements, each consisting of separate membrane and bending parts, without any direct coupling at the element level. The second approach uses curved elements which better approximate the shell surface and which provide membrane-bending coupling in the element level.

It is desirable, of course, to have proper membrane-bending coupling within the element. However, curved shell elements can be computationally very expensive, due to the complexity of the formulation, and they can lead to significant computational effort when structural optimization is carried out, since many evaluations are necessary. For flat shell element, the bending-stretching coupling is attained as a result of transformation of the element stiffness matrices from a local to the global coordinate system prior to assembly.

Though a large number of flat elements are needed to model curved structure accurately, flat shell elements are still widely used because of their simplicity and cost effectiveness, and are an obvious choice in the analysis of folded plate structure (ZL91).

Among common flat shell elements, triangular elements are more effective for the meshing of general shells than are quadrilateral elements. However, some flat shell elements, especially those derived by generalization of flat plate elements, possess no rotational (drilling) stiffness in the direction perpendicular to the element surface. In that case, the singularity of the global stiffness matrix creates a problem when neighboring elements are coplanar. Thus, many bending elements based on Mindlin-plate theory have two in-plane rotations (in the vector rotation sense) at each node. When they are combined with membrane elements, which have two in-plane displacements at nodes, the resulting flat shell element has a singularity problem for coplanar elements. In order to overcome this difficulty, the addition of fictitious out of plane (in the vector sense) rotational stiffness at a node where elements are coplanar or suppression of the drilling rotation in local coordinate system were tried but both methods were found to be not effective for practical purpose (BAT82). A better way of overcoming this problem is to use a drilling degree of freedom in the membrane element. The Allman triangular element (ALL84) is the first successful element with drilling degrees of freedom. Flat shell elements obtained by combining the Allman element with bending elements based on Discrete Kirchhoff Theory (DKT) have been successfully employed for linear shell analysis (CHE92, EKE92). In an effort to prevent undesirable shear locking for the thin plates in the Reissner-Mindlin plate, several plate elements were developed based on discrete Kirchhoff theory in which the Kirchhoff assumption is applied in a discrete way along the edge of the element, and the transverse shear energy is neglected (BH81, BBH80, DMM86). One of the most successful DKT element was developed by Batoz and colleagues (BBH80). Their formulation of element

stiffness matrix starts with the approximations of rotations; and the discrete kirchhoff hypothesis was imposed along the edges, where a cubic interpolation of the transverse displacement was assumed. Therefore, the transverse displacement was not defined in the interior of the plate element . The geometric stiffness matrix required for the non-linear analysis and buckling of plates and shells requires the first derivative of transverse displacement. To obtain it, either lower order interpolation of the displacement (FDB89, TD87) or a constant non-linear strain based on the strain projection method (SC86) have been tried. In that regard, the DKTL element proposed by Meek and Tan (MK85) is more consistent, because transverse displacement was interpolated quadratically over the element before discrete Kirchhoff hypothesis are imposed at the Loof nodes. That element was followed by the flat shell element (MK86a) which superposes this bending element with LST (Linear Strain Triangular) membrane element which has superior accuracy compared to constant strain triangles (CST).

By using the rotation of the Loof node as a degree of freedom in their element, the rotational singularity mentioned above was eliminated. This flat shell element has been successfully employed for both linear and non-linear analyses of thin shells (MK86a, MK86b). In the formulation of the bending element, one of the basis functions for normal rotations is cubic, that requires seven points to numerically integrate the elements of stiffness matrix, while three points are needed for the integration of membrane stiffness contributions. As a result this element can be computationally expensive.

The motivation for the current research is the need to find numerically inexpensive thin shell elements which: 1) have high accuracy in predicting the buckling loads of wing-like structures, 2) do not suffer from rotational singularities, and 3) are simple enough so that their stiffness matrices can be derived and calculated in closed form so that analytic shape sensitivities can be obtained in explicit closed form. These features would give a

method for the effective selection of intermediate design variables and intermediate response functions for successful approximations. In the present work the flat shell element developed by Meek and Tan is used, because it is free of rotational singularity and has demonstrated successful performance in linear shell buckling analysis.

An important new contribution is given in the following sections. The stiffness matrix and geometric stiffness matrix will be derived *explicitly* in terms of the element nodal coordinates, cross-section properties and material properties. This explicit formulation will reduce the computation time and lead to explicitly-derived analytic sensitivities, because no numerical integrations are involved. In order to make this thesis self-contained, formulations of stiffness and geometric stiffness matrices of this DKTL shell element are derived following the analysis of Meek and Tan (MK86a). Then the element stiffness matrix for the static analyses will be derived in closed form, by the superposition of DKTL bending element and the LST membrane element. By using an explicit form of the transformation matrix from local to global coordinates, the closed form expression for the global stiffness matrix is obtained. Because of its complexity, both manual and computer-assisted algebraic manipulation using MATHEMATICA(W91) was combined to calculate explicit formulation.

3.2 The Flat Shell Element

A curved shell can be approximated as a faceted surface by connecting flat triangular elements together at vertex nodes, as shown in Figure 3.1. Each element has 3 vertex nodes and three midside nodes located in the middle of three sides of the triangle. The element stiffness matrix is formulated in the local coordinate system by superposing the membrane stiffness matrix and the bending stiffness matrix. As a result, there are twenty four degrees

of freedom: twelve displacements for the membrane action and twelve degrees of freedom for the bending action.

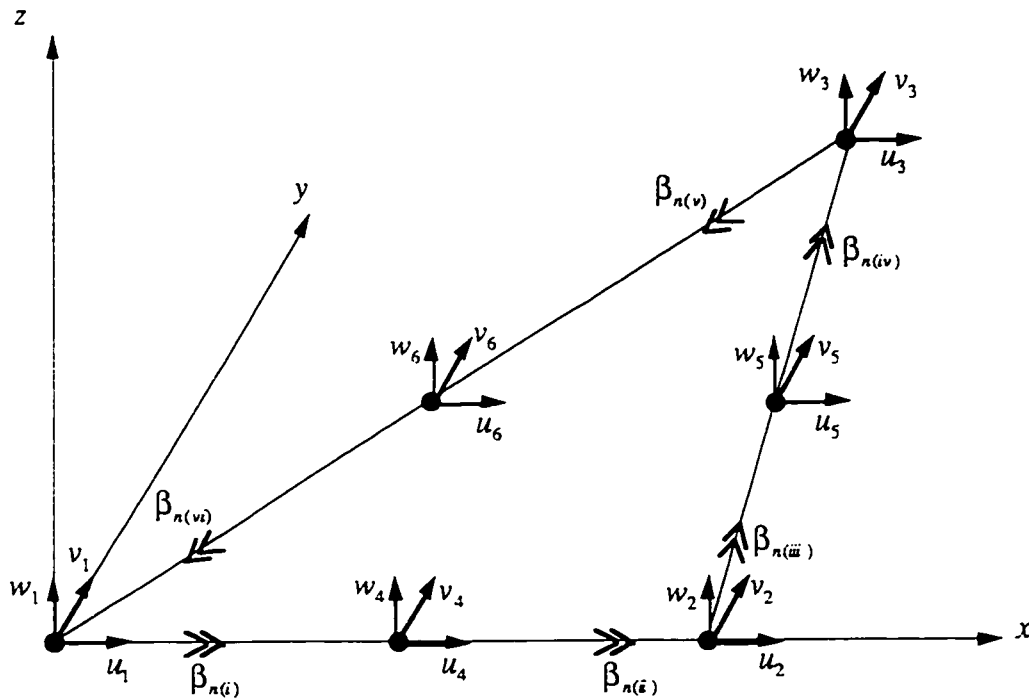


Figure 3.1 Geometry and nodal parameters of element

The LST is chosen to model membrane behavior, the two inplane displacements at each of the six nodes gives the twelve degrees of freedom for the membrane stiffness. The bending stiffness is formulated using Mindlin plate theory in which the interpolations of the normal rotations β_x and β_y are independent of transverse displacement. A higher order term is added to the quadratic interpolation for normal rotations so that shape functions can be found for the Loof nodes: two Gaussian points along each side of the triangle. In order to model thin plate behavior, Kirchhoff assumptions are imposed at discrete points and the degree of freedom are reduced to twelve, six of which are out-of plane displacements at six

nodes and the other six are the normal rotations at the Loof nodes. The global stiffness matrix is obtained by transformation from the local coordinate system to global coordinate system.

3.3 Bending Stiffness Matrix

3.3.1 Discrete Kirchhoff Theory

In the Reissner-Mindlin plate theory, the normal vector is assumed to remain straight in the deformed plate and its elongation of the normal is neglected. The displacement in a midplane symmetric laminate is therefore written as

$$\begin{aligned} u(x, y, z) &= z \beta_x(x, y) \\ v(x, y, z) &= -z \beta_y(x, y) \\ w(x, y, z) &= w(x, y) \end{aligned} \quad (3.1)$$

where u , v and w are displacements and β_x and β_y are the normal rotations as shown in Figure 3.2. These displacement assumptions leads to independent interpolations of the rotations β_x and β_y and the transverse displacement w .

The resulting bending strains can be expressed in terms of the normal rotations β_x and β_y ; as

$$\{\epsilon^b\} = \begin{Bmatrix} \epsilon_{xx}^b \\ \epsilon_{yy}^b \\ \gamma_{xy}^b \end{Bmatrix} = z \begin{Bmatrix} \beta_{x,x} \\ -\beta_{y,y} \\ \beta_{x,y} - \beta_{y,x} \end{Bmatrix} = z\{\kappa\} \quad (3.2)$$

and the transverse shear strains are

$$\{\epsilon^f\} = \begin{Bmatrix} \gamma_{zx} \\ \gamma_{zy} \end{Bmatrix} = \begin{Bmatrix} w_{,x} + \beta_x \\ w_{,y} - \beta_y \end{Bmatrix} \quad (3.3)$$

where the subscript after the comma indicates partial differentiation.

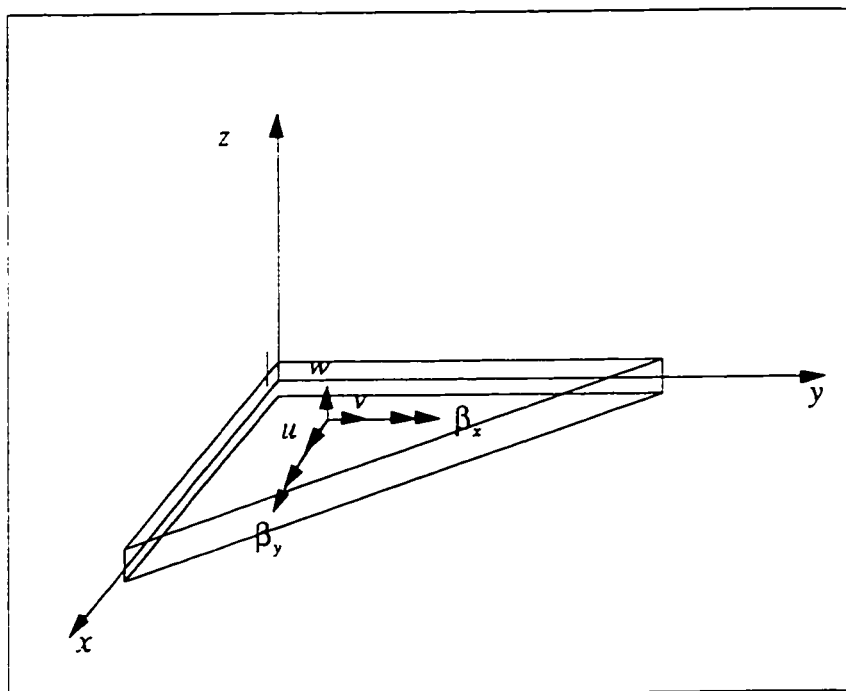


Figure 3.2 Displacements and coordinates of the bending element

To model thin plate behavior, in which the transverse shear effect is negligible, the Kirchhoff assumption that the normal remains normal in the deformed plate is applied by imposing

$$\begin{aligned} w_{,x} + \beta_x &= 0 \\ w_{,y} - \beta_y &= 0 \end{aligned} \quad (3.4)$$

over the element.

Using the plane stress assumption, the bending stresses are related to bending strains by

$$\{\sigma^b\} = [D] \{\epsilon^b\} \quad (3.5)$$

where $[D]$ is the constitutive matrix for the plane stress assumption.

The bending moments are obtained by integrating the stresses through the thickness as

$$\{M\} = \begin{Bmatrix} M_{xx} \\ M_{yy} \\ M_{xy} \end{Bmatrix} = [D_b] \{\kappa\} \quad (3.6)$$

For an isotropic, homogeneous plate with Young's modulus E , Poisson's ratio ν and thickness t

$$[D_b] = \begin{bmatrix} \frac{Et^3}{12(1-\nu^2)} & \frac{Et^3}{12(1-\nu^2)} & 0 \\ \frac{\nu Et^3}{12(1-\nu^2)} & \frac{Et^3}{12(1-\nu^2)} & 0 \\ 0 & 0 & \frac{Et^3}{24(1+\nu)} \end{bmatrix} \quad (3.7)$$

and the resulting strain energy of the plate bending is expressed as

$$U = \frac{1}{2} \int_A \{\kappa\}^T [D_b] \{\kappa\} dA \quad (3.8)$$

3.3.2 Interpolations for Transverse Displacement and Normal Rotations

The transverse displacement w is assumed to be quadratic in an element with the form

$$w = [N] \{w\} \quad (3.9)$$

where the shape functions in area coordinates are

$$[N] = [\zeta_1(2\zeta_1 - 1) \quad \zeta_2(2\zeta_2 - 1) \quad \zeta_3(2\zeta_3 - 1) \quad 4\zeta_1\zeta_2 \quad 4\zeta_2\zeta_3 \quad 4\zeta_1\zeta_3] \quad (3.10)$$

and

$$\{w\}^T = [w_1 \quad w_2 \quad w_3 \quad w_4 \quad w_5 \quad w_6] \quad (3.11)$$

The interpolation of the normal rotations β_x and β_y , is given by:

$$\beta_x = [L] \{a\} \quad (3.12)$$

where

$$[L] = [1 \quad \zeta_1 \quad \zeta_2 \quad \zeta_1^2 \quad \zeta_1\zeta_2 \quad \zeta_2^2 \quad (2\zeta_1^3 + 3\zeta_1^2\zeta_2 - 3\zeta_1\zeta_2^2 - 2\zeta_2^3)] \quad (3.13)$$

and $\{a\}$ is the vector of generalized displacements. The first six terms in Eq. (3.13) form a complete quadratic interpolation, and a single higher order term is added. Substituting the area coordinates of the Loof nodes and center node into above equation results in

$$\{\beta_x^L\} = [A] \{a\} \quad (3.14)$$

where

$$\{\beta_x^L\}^T = [\beta_{x(i)} \quad \beta_{x(ii)} \quad \beta_{x(iii)} \quad \beta_{x(iv)} \quad \beta_{x(v)} \quad \beta_{x(vi)} \quad \beta_{x(c)}] \quad (3.15)$$

Thus

$$\beta_x = [L] [A]^{-1} \{\beta_x^L\} \quad (3.16)$$

Similarly,

$$\beta_y = [L] [A]^{-1} \{\beta_y^L\} \quad (3.17)$$

These provides the original twenty degees of freedom which are composed of six transverse displacements and twelve normal rotations.

3.3.3 Applications of Shear Constraints

In order to model the thin plate behavior in which shear strain effect is negligible, the Kirchhoff assumptions are imposed at a discrete number of points:

$$\gamma_{xz} = w_{,s(j)} - \beta_{s(j)} = 0 \quad \text{at } j = (i), \dots, (vi) \quad (3.18)$$

and over the element:

$$\int_A \gamma_{xz} dA = \int_A \gamma_{yz} dA = 0 \quad (3.19)$$

After these constraints are applied at six Loof nodes and over the element, the original twenty d.o.f. for the bending element are reduced to twelve as:

$$\begin{aligned} \{\beta_x^L\} &= [C_x] \begin{Bmatrix} \{w\} \\ \{\beta_n\} \end{Bmatrix} \\ \{\beta_y^L\} &= [C_y] \begin{Bmatrix} \{w\} \\ \{\beta_n\} \end{Bmatrix} \end{aligned} \quad (3.20)$$

where

$$\{\beta_n\}^T = \{\beta_{n(i)}, \beta_{n(ii)}, \beta_{n(iii)}, \beta_{n(iv)}, \beta_{n(v)}, \beta_{n(vi)}\} \quad (3.21)$$

and two (7×12) matrices. The $[C_x]$ and $[C_y]$ are given in Appendix A.

The normal rotations expressed in terms of the final degrees of freedom are obtained by substituting Eq. (3.20) to Eqs. (3.16) and (3.17), to get

$$\begin{aligned} \{\beta_x\} &= [L] [A^{-1}] [C_x] \begin{Bmatrix} \{w\} \\ \{\beta_n\} \end{Bmatrix} \\ \{\beta_y\} &= [L] [A^{-1}] [C_y] \begin{Bmatrix} \{w\} \\ \{\beta_n\} \end{Bmatrix} \end{aligned} \quad (3.22)$$

3.3.4 The Evaluations of the Stiffness Matrix and Consistent Load Vector

As the two normal rotations are expressed in local coordinate system, the first derivatives about the local coordinate system have the following form

$$\begin{aligned}\frac{\partial\{\beta_x\}}{\partial x} &= [L_{,x}] [A^{-1}] [C_x] \begin{Bmatrix} \{w\} \\ \{\beta_n\} \end{Bmatrix} \\ \frac{\partial\{\beta_y\}}{\partial y} &= [L_{,y}] [A^{-1}] [C_y] \begin{Bmatrix} \{w\} \\ \{\beta_n\} \end{Bmatrix}\end{aligned}\quad (3.23)$$

where

$$\begin{aligned}[L_{,x}] &= \frac{\partial[L]}{\partial x} \\ [L_{,y}] &= \frac{\partial[L]}{\partial y}\end{aligned}\quad (3.24)$$

From Eqs. (3.2) and (3.23), the bending strain - displacement can be written

$$\{\epsilon^b\} = z \begin{Bmatrix} [L_{,x}] [A^{-1}] [C_x] \\ -[L_{,y}] [A^{-1}] [C_y] \\ [L_{,y}] [A^{-1}] [C_x] - [L_{,x}] [A^{-1}] [C_y] \end{Bmatrix} \begin{Bmatrix} \{w^b\} \\ \{\beta_n\} \end{Bmatrix} = z [B^b] \begin{Bmatrix} \{w^b\} \\ \{\beta_n\} \end{Bmatrix}\quad (3.25)$$

Since the Kirchhoff hypothesis is imposed in the interpolation of normal rotations, shear strain energy is ignored and the resulting element bending stiffness matrix becomes

$$[K^b] = \iint_A [B^b]^T [D_b] [B^b] dA\quad (3.26)$$

The consistent load vector corresponding to the element stiffness matrix is

$$\{f^b\}^T = \int_A [N_w] p_z dA\quad (3.27)$$

where

$$[N_w] = [\zeta_1(2\zeta_1 - 1) \quad \zeta_2(2\zeta_2 - 1) \quad \zeta_3(2\zeta_3 - 1) \quad 4\zeta_1\zeta_2 \quad 4\zeta_2\zeta_3 \quad 4\zeta_1\zeta_3 \quad 0 \quad , \quad , \quad 0]\quad (3.28)$$

When a uniformly distributed load, p_z , is applied over the element, the load vector is

$$\{f^b\}^T = p_z \begin{bmatrix} 0 & 0 & 0 & \frac{A}{3} & \frac{A}{3} & \frac{A}{3} & 0 & 0 & 0 & 0 & 0 & 0 \end{bmatrix} \quad (3.29)$$

3.4 Membrane Stiffness Matrix

The L.S.T.(Linear Strain Triangular) element is chosen for membrane behavior of the shell. The in-plane displacements are quadratic over an element.

$$\begin{aligned} u &= [N] \{u\} \\ v &= [N] \{v\} \end{aligned} \quad (3.30)$$

where

$$\begin{aligned} \{u\} &= \{u_1, u_2, u_3, u_4, u_5, u_6\} \\ \{v\} &= \{v_1, v_2, v_3, v_4, v_5, v_6\} \end{aligned} \quad (3.31)$$

and $[N]$ is given in Eq.(3.10).

The membrane strains are given by

$$\{\epsilon^m\} = \begin{Bmatrix} \epsilon_{xx}^m \\ \epsilon_{yy}^m \\ \gamma_{xy}^m \end{Bmatrix} = \begin{Bmatrix} u_{,x} \\ v_{,y} \\ u_{,y} + v_{,x} \end{Bmatrix} \quad (3.32)$$

From Eqs.(3.30) and (3.32), the membrane strain-displacement relations have the form

$$\{\epsilon^m\} = \begin{Bmatrix} [N_{,x}] & [0] \\ [0] & [N_{,y}] \\ [N_{,y}] & [N_{,x}] \end{Bmatrix} \begin{Bmatrix} \{u^a\} \\ \{v^a\} \end{Bmatrix} = [B^m] \begin{Bmatrix} \{u^a\} \\ \{v^a\} \end{Bmatrix} \quad (3.33)$$

where

$$\begin{aligned} [N_{,x}] &= \frac{\partial [N]}{\partial x} \\ [N_{,y}] &= \frac{\partial [N]}{\partial y} \end{aligned} \quad (3.34)$$

With the stress-strain relation for the membrane stress as

$$\{\sigma^m\} = [D] \{\epsilon^m\} \quad (3.35)$$

the resultant force can be obtained by integrating the stresses through the thickness to get

$$\{N_m\} = \begin{Bmatrix} N_{xx} \\ N_{xy} \\ N_{xy} \end{Bmatrix} = [D_m] \{\epsilon^m\} \quad (3.36)$$

where, for an isotropic material with constant thickness t

$$[D_m] = \begin{bmatrix} \frac{Et}{(1-\nu^2)} & \frac{Et}{(1-\nu^2)} & 0 \\ \frac{\nu Et}{(1-\nu^2)} & \frac{Et}{(1-\nu^2)} & 0 \\ 0 & 0 & \frac{Et}{2(1+\nu)} \end{bmatrix} \quad (3.37)$$

The element membrane stiffness matrix then becomes

$$[K^m] = \int_A [B^m]^T [D_m] [B^m] dA \quad (3.38)$$

The consistent load vector corresponding to the in-plane force p_{xy} is obtained as

$$\{f^m\}^T = \int_A [N] p_{xy} dA \quad (3.39)$$

3.5 Constitutive Equations for Composite Layer

In the classical laminate theory, the constitutive equations for an orthotropic layer, in its principal axes system of the material, are

$$\begin{Bmatrix} \sigma_{11} \\ \sigma_{22} \\ \tau_{12} \end{Bmatrix} = [\overline{Q}_{ij}] \begin{Bmatrix} \epsilon_{11} \\ \epsilon_{22} \\ \gamma_{12} \end{Bmatrix} \quad (3.40)$$

where

$$[\bar{Q}_{ij}] = \begin{bmatrix} \frac{E_1}{1 - \nu_{12}\nu_{21}} & \frac{\nu_{21}E_1}{1 - \nu_{12}\nu_{21}} & 0 \\ \frac{\nu_{21}E_1}{1 - \nu_{12}\nu_{21}} & \frac{E_2}{1 - \nu_{12}\nu_{21}} & 0 \\ 0 & 0 & G_{12} \end{bmatrix} \quad (3.41)$$

Since the x, y coordinate system is not aligned with the material axes of each layer, as shown in Figure 3.3, these constitutive equations must be transformed to the x, y system in each layer.

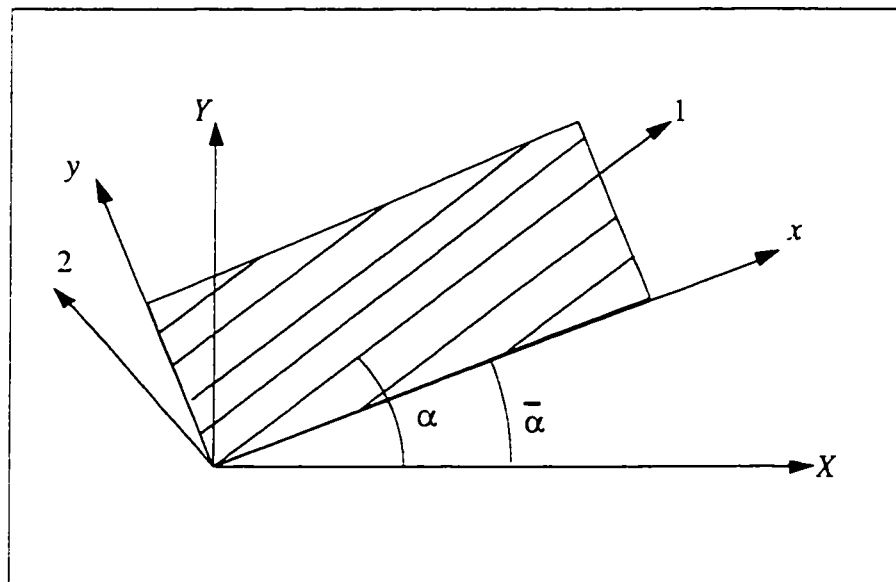


Figure 3.3 Rotations of coordinate system for a laminate

Thus the stress-strain relations in the local coordinate system for a typical k th layer become

$$\begin{Bmatrix} \sigma_{xx} \\ \sigma_{yy} \\ \tau_{xy} \end{Bmatrix}_k = [Q_{ij}]_k \begin{Bmatrix} \epsilon_{xx} \\ \epsilon_{yy} \\ \gamma_{xy} \end{Bmatrix}_k \quad (3.42)$$

where

$$[Q_{ij}]_k = [T_c] [\bar{Q}_{ij}] [T_c]^T \quad (3.43)$$

The transformation matrix $[T_c]$ from material axes of each layer to x, y system is

$$[T_c] = \begin{bmatrix} c^2 & s^2 & -2cs \\ s^2 & c^2 & 2cs \\ cs & -cs & c^2 - s^2 \end{bmatrix} \quad (3.44)$$

where $c = \cos(\alpha - \bar{\alpha})$ and $s = \sin(\alpha - \bar{\alpha})$ (3.45)

and α , $\bar{\alpha}$ are the angles of the material axes and the local coordinates with respect to the reference axis, which can be defined either locally or globally.

When the laminate is symmetric, there is no coupling between bending and extension in the element. Therefore for the symmetric angle-ply laminates, the bending moments $\{M\}$ can be obtained by integrating the stresses due to bending through the thickness. They are

$$\{M\} = \begin{Bmatrix} M_{xx} \\ M_{yy} \\ M_{xy} \end{Bmatrix} = [D_b] \{\kappa\} \quad (3.46)$$

and for the symmetric laminates

$$[D_b] = \frac{1}{3} \sum_{i=1}^n [Q_{ij}]_k (h_k^3 - h_{k-1}^3) \quad (3.47)$$

where h_k and h_{k-1} are the upper and lower position of the k th laminate in the thickness direction as shown in Figure 3.4.

Similarly, the resultant membrane forces for the symmetric laminates are

$$\{N_m\} = \begin{Bmatrix} N_{xx} \\ N_{xy} \\ N_{xy} \end{Bmatrix} = [D_m] \{\epsilon^m\} \quad (3.48)$$

with

$$[D_m] = \sum_{k=1}^n [Q_{ij}]_k (h_k - h_{k-1}) \quad (3.49)$$

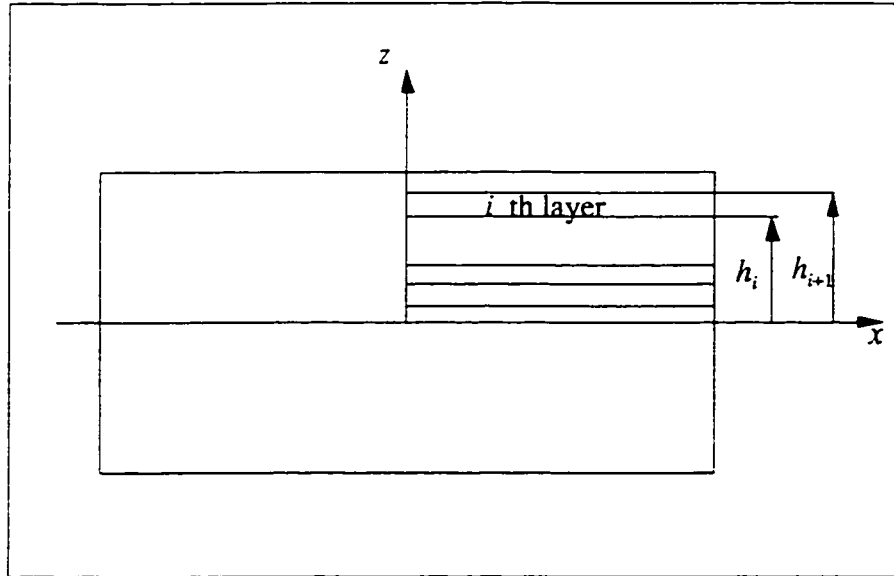


Figure 3.4 Geometry of the laminate

3.6 Geometric Stiffness Matrix

When the transverse shear strains are negligible, Green-Lagrange strain vector is given as

$$\{\epsilon\} = \begin{Bmatrix} \epsilon_x \\ \epsilon_y \\ \gamma_{xy} \end{Bmatrix} = \{\epsilon^m\} + \{\epsilon^b\} + \{\epsilon^{nl}\} \quad (3.50)$$

where non-linear strain is expressed as

$$\{\epsilon^{nl}\} = \left. \begin{Bmatrix} \frac{1}{2} \left(\frac{\partial u}{\partial x} \right)^2 + \frac{1}{2} \left(\frac{\partial v}{\partial x} \right)^2 + \frac{1}{2} \left(\frac{\partial w}{\partial x} \right)^2 \\ \frac{1}{2} \left(\frac{\partial u}{\partial y} \right)^2 + \frac{1}{2} \left(\frac{\partial v}{\partial y} \right)^2 + \frac{1}{2} \left(\frac{\partial w}{\partial y} \right)^2 \\ \left(\frac{\partial u}{\partial x} \right) \left(\frac{\partial u}{\partial y} \right) + \left(\frac{\partial v}{\partial x} \right) \left(\frac{\partial v}{\partial y} \right) + \left(\frac{\partial w}{\partial x} \right) \left(\frac{\partial w}{\partial y} \right) \end{Bmatrix} \right\} \quad (3.51)$$

Introducing the Von Karman assumptions, that the derivatives of u and v with respect to x and y are small, yields the following non-linear strain

$$\{\epsilon^nl\} = \left\{ \begin{array}{c} \frac{1}{2} \left(\frac{\partial w}{\partial x} \right)^2 \\ \frac{1}{2} \left(\frac{\partial w}{\partial y} \right)^2 \\ \left(\frac{\partial w}{\partial x} \right) \left(\frac{\partial w}{\partial y} \right) \end{array} \right\} \quad (3.52)$$

The potential energy produced by non-linear strains can be written as

$$U = \frac{1}{2} \iint_A \begin{bmatrix} \frac{\partial w}{\partial x} & \frac{\partial w}{\partial y} \end{bmatrix} \begin{bmatrix} N_{xx} & N_{xy} \\ N_{xy} & N_{yy} \end{bmatrix} \left\{ \begin{array}{c} \frac{\partial w}{\partial x} \\ \frac{\partial w}{\partial y} \end{array} \right\} dA \quad (3.53)$$

The use of matrix $[G]$ defined by

$$\left\{ \begin{array}{c} \frac{\partial w}{\partial x} \\ \frac{\partial w}{\partial y} \end{array} \right\} = \begin{bmatrix} [0] & [0] & [N_{,x}] & [0] \\ [0] & [0] & [N_{,y}] & [0] \end{bmatrix} \{\bar{\delta}^e\} = [G] \{\bar{\delta}^e\} \quad (3.54)$$

leads to the potential energy form

$$U = \frac{1}{2} \{\bar{\delta}^e\}^T [K_G] \{\bar{\delta}^e\} \quad (3.55)$$

where geometric stiffness matrix is defined in the local coordinate system as

$$[K_G^e] = \int_A [G]^T \begin{bmatrix} N_{xx} & N_{xy} \\ N_{xy} & N_{yy} \end{bmatrix} [G] dA \quad (3.56)$$

and

$$\{\bar{\delta}^e\}^T = \left\{ \{u^n\}^T \quad \{u^n\}^T \quad \{w\}^T \quad \{\beta_n\}^T \right\} \quad (3.57)$$

3.7 Transformation to Global Coordinates

Both membrane and bending stiffness matrices are calculated in local coordinate system in which the local x axis is aligned with the line vector from node 1 to node 2, and z axis is perpendicular to the element plane. The element stiffness matrix of the shell is obtained by superposing membrane and bending stiffness matrices and membrane-bending coupling is attained by employing the proper spatial transformation. The transformation matrix $[T]$ between local and global coordinates is calculated using the vectors H and G which is shown in Figure 3.5

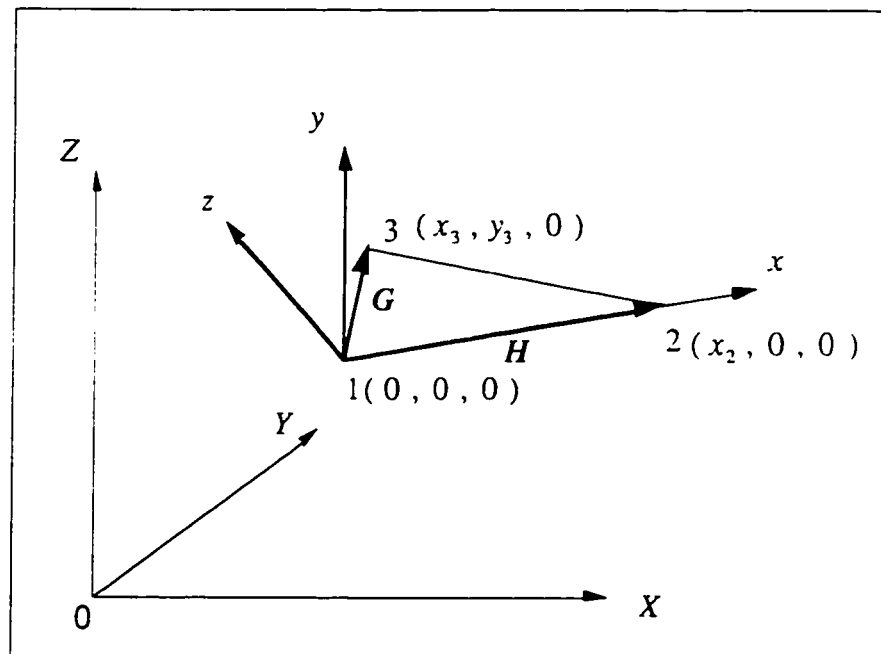


Figure 3.5 Local coordinate system

$$\begin{aligned} \{H\} &= \begin{Bmatrix} X_2 - X_1 \\ Y_2 - Y_1 \\ Z_2 - Z_1 \end{Bmatrix} \\ \{G\} &= \begin{Bmatrix} X_3 - X_1 \\ Y_3 - Y_1 \\ Z_3 - Z_1 \end{Bmatrix} \end{aligned} \quad (3.58)$$

leading to the transformation

$$[T] = \begin{bmatrix} \{l\}^T \\ \{m\}^T \\ \{n\}^T \end{bmatrix} \quad (3.59)$$

where

$$\begin{aligned} \{l\} &= \frac{\{H\}}{\|\{H\}\|} \\ \{n\} &= \frac{\{H\} \times \{G\}}{\|\{H\} \times \{G\}\|} \\ \{m\} &= \{n\} \times \{l\} \end{aligned} \quad (3.60)$$

The transformation matrix can be expressed in terms of three vertex nodal coordinates in the global coordinates system (See Appendix B).

By attaching node 1 to the origin of the local coordinate system, as shown Figure 3.5, there are only three non-zero nodal coordinates exist in the local coordinate system:

$$\begin{aligned} x_2 &= \{l\}^T \{H\} \\ x_3 &= \{l\}^T \{G\} \\ y_3 &= \{m\}^T \{G\} \end{aligned} \quad (3.61)$$

This is important in the shape sensitivity analysis to follow, where many derivative calculation with respect to local coordinates can be avoided by reducing the number of non-zero nodal coordinates.

numbering are of ascending order along the edge, the components of the transformation matrix used for the normal rotations are positive and the normal rotations have the sense shown in Figure 3.1. Also the force vector can be written in the global coordinates through the same transformation

$$\{f\} = [\Lambda]^T \{f^e\} \quad (3.68)$$

Chapter 4

The Explicit Formulation of the Stiffness and Geometric Stiffness Matrices

4.1 Introduction

The development of finite element codes can be greatly enhanced with the aid of symbolic computation. One may utilize the symbolic method to assist in the derivation of element stiffness matrices, which can then be readily adopted for computer implementation. Furthermore, with the availability of a proper translator, derived equations can be converted automatically to appropriate computer code.

Using symbolic computation for finite element analysis provides several obvious benefits: (1) reducing manual tedium, (2) the derived equations may have improved computational efficiency and numerical accuracy, (3) increased reliability in derived equations and automated code conversion, and (4) reduced time in finite element development. A sample of publications describing the use of symbolic computation for finite element structural analysis can be found in references NA79, KF79, CTZY90, JK85, and LT95.

Due to the presence of higher order terms for the approximation of normal rotations in the current flat shell element, previously a seven point Gauss quadrature was used to integrate the element stiffness matrix numerically. As a result, a finite element analysis of a large structure using this element can be computationally quite expensive. In order to overcome this difficulty, here explicit formulations of the element matrices are derived, with the help of a symbolic computation package.

The formulation of shell element stiffness matrix terms requires the integration of material properties and polynomials of natural coordinates over the area of the element. This integration can be evaluated analytically if the specific polynomial expressions for all components can be found by symbolic computation. However, if we apply the symbolic computation in a brute force manner, the growth of the resulting expressions will be excessive and the derived formulation can be of little use.(CTZY90)

In the following , the strain-displacement relations will be expressed in terms of nodal coordinates in the local coordinate system via the explicit Jacobian matrix for the straight-sided triangular element. These expressions in terms of nodal coordinates are needed so that explicit derivatives with respect to element shape can be obtained. The polynomial expression for each component of element matrices is calculated with the help of the symbolic computation package, MATHEMATICA (W91). In order to simplify the expressions of the integrand, we will extract any terms independent of the integration variables. Finally, explicit formulation will be derived by applying analytic integration rules with MATHEMATICA.

4.2 Stiffness Matrix

Using the three corner nodes and the three midside nodes in Figure 3.5, it is possible to get an explicit inverse of the Jacobian as

$$\begin{bmatrix} \frac{\partial \xi_1}{\partial x} & \frac{\partial \xi_2}{\partial x} \\ \frac{\partial \xi_1}{\partial y} & \frac{\partial \xi_2}{\partial y} \end{bmatrix} = \frac{1}{J} \begin{bmatrix} -y_3 & y_3 \\ x_3 - x_2 & x_3 \end{bmatrix} \quad (4.1)$$

where

$$J = x_2 \times y_3 \quad (4.2)$$

is two times the area of the element. $2A$.

The integration of a polynomial in area coordinates over the triangle area is accomplished by the formula

$$\begin{aligned} \iint_A \xi_1^m \xi_2^n dA &= \frac{m!n!}{(2+m+n)!} 2A \\ \int_0^1 \int_0^{1-\xi_1} \xi_1^m \xi_2^n d\xi_2 d\xi_1 &= \frac{m!n!}{(2+m+n)!} \end{aligned} \quad (4.3)$$

Using the Eq. (4.1) and (3.10), the membrane strains-displacement relations in Eq. (3.33) can be rewritten explicitly in terms of local nodal coordinates

$$[B^m] = \begin{bmatrix} [N_x] & 0 \\ 0 & [N_y] \\ [N_y] & [N_x] \end{bmatrix} \quad (4.4)$$

where

$$[N_x] = \frac{1}{J} \begin{Bmatrix} -y_3(4\xi_1 - 1) \\ y_3(4\xi_2 - 1) \\ 0 \\ 4(-y_3\xi_2 + y_3\xi_1) \\ 4y_3\xi_3 \\ -4y_3\xi_3 \end{Bmatrix}^T \quad (4.5)$$

$$[N_y] = \frac{1}{J} \begin{Bmatrix} -(x_2 - x_3)(4\xi_1 - 1) \\ -x_3(4\xi_2 - 1) \\ x_2(4\xi_3 - 1) \\ 4(-x_3\xi_1 - (x_2 - x_3)\xi_2) \\ 4(-x_3\xi_3 + x_2\xi_2) \\ -4((x_2 - x_3)\xi_3 - x_2\xi_1) \end{Bmatrix}^T \quad (4.6)$$

Substitution of Eqs. (4.4), (4.5) and (4.6) into Eq. (3.38) gives

$$[K^m] = \frac{1}{J} [\bar{K}^m] \quad (4.7)$$

where

$$[\bar{K}^m] = \iint_A [B^m]^T [D_m] [B^m] J dA \quad (4.8)$$

For the explicit expression of $[\bar{K}^m]$, matrix product $[B^m]^T [D_m] [B^m]$ is first calculated analytically using symbolic computations, which results in the explicit form of the various components in terms of the area coordinates and their coefficients. Then analytical integration of the result is performed by integrating the matrix components using the analytic integration rule given in Eq.(4.3). Since the components of resulting matrix product are functions of area coordinates, the order of the each monomial with its coefficient is examined and the corresponding integration is obtained (See Appendix D for the MATHEMATICA code). As a result, each component is expressed in terms of material properties and the three non-zero nodal coordinates, x_2 , x_3 and y_3 in the local coordinate system. The final expressions are translated to the FORTRAN format using the built-in translator in MATHEMATICA.

Similarly, the closed form expression can be obtained for the matrix $[B^b]$ which relates the bending strains and displacements in Eq. (3.25) as

$$[B^b] = \left\{ \begin{array}{l} [L_{,x}] [A^{-1}] [C_x] \\ -[L_{,y}] [A^{-1}] [C_y] \\ [L_{,y}] [A^{-1}] [C_x] - [L_{,x}] [A^{-1}] [C_y] \end{array} \right\} \quad (4.9)$$

In order to simplify the integrand of the element stiffness matrix in Eq. (3.25), constant factors will be extracted by splitting the matrix $[B^b]$ into two sub-matrices

$$[B^b] = [S] [R] \quad (4.10)$$

$$[S] = \begin{bmatrix} [L_{,x}] & 0 \\ 0 & -[L_{,y}] \\ [L_{,y}] & -[L_{,x}] \end{bmatrix} \quad (4.11)$$

$$[R] = \begin{bmatrix} [A]^{-1} [C_x] \\ [A]^{-1} [C_y] \end{bmatrix} \quad (4.12)$$

Here, the components of matrix $[R]$ are expressed in terms of nodal coordinates and are independent of area coordinates, where $[S]$ contains both the nodal coordinates and integration variables ξ_1 , ξ_2 and ξ_3 . Since the explicit inverse Jacobian is available in Eq.(4.1), $[L_{,x}]$ and $[L_{,y}]$ can be written in closed-form as

$$[L_{,x}] = \frac{1}{J} \left\{ \begin{array}{c} 0 \\ -y_3 \\ y \\ -2y_3\xi_1 \\ -y_3\xi_2 + y_3\xi_1 \\ 2y_3\xi_2 \\ -y_3(6\xi_1^2 + 6\xi_1\xi_2 - 3\xi_2^2) + y_3(3\xi_1^2 - 6\xi_1\xi_2 - 6\xi_2^2) \end{array} \right\}^T \quad (4.13)$$

$$[L_{,y}] = \frac{1}{J} \left\{ \begin{array}{c} 0 \\ -(x_2 - x_3) \\ -x_3 \\ -2(x_2 - x_3)\xi_1 \\ -(x_2 - x_3)\xi_2 - x_3\xi_1 \\ -2x_3\xi_2 \\ -(x_2 - x_3)(6\xi_1^2 + 6\xi_1\xi_2 - 3\xi_2^2) - x_3(3\xi_1^2 - 6\xi_1\xi_2 - 6\xi_2^2) \end{array} \right\}^T \quad (4.14)$$

Since all the components of the matrix $[R]$ are independent of the integration variables, the bending stiffness matrix can be rewritten in the following form

$$[K^b] = \frac{1}{J} [R]^T [\bar{S}] [R] \quad (4.15)$$

where

$$[\bar{S}] = \iint_A [S]^T [D_b] [S] J dA \quad (4.16)$$

An explicit expression for $[\bar{S}]$ is obtained from the symbolic computation of the matrix product $[S]^T [D_b] [S]$ followed by the analytic integration of each component.

Since the element stiffness matrix is the superposition of membrane stiffness and bending stiffness matrices, which are already in explicit forms in Eqs. (4.7) and (4.15), it

can be written in global coordinate through the transformation matrix $[\Lambda]$ which is also written in an explicit form of nodal coordinates in global coordinate system.

4.3 Geometric Stiffness Matrix

Since the geometric stiffness matrix, $[K_G^e]$ depends on the membrane forces linearly, as shown in Eq.(3.56), the closed form of membrane forces are required for the explicit formulation of $[K_G^e]$. After the displacement solution in global coordinates is calculated from Eq. (2.5), the resultant membrane forces are recovered by combining Eqs. (3.33) and (4.4) in the local coordinate system as

$$\{N_m\} = [D_m] [B_m] \begin{Bmatrix} \{u\} \\ \{v\} \end{Bmatrix} \quad (4.17)$$

The above in-plane displacements defined in local coordinates can be obtained from the transformation matrix, $[T_m]$, which extracts the nodal displacements in local coordinate from the solution such as

$$\begin{Bmatrix} \{u^a\} \\ \{v^a\} \end{Bmatrix} = [T_m] \{\delta\} \quad (4.18)$$

Therefore, the membrane forces are obtained explicitly from the following relation

$$\{N_m\} = [D_m] [B_m] [T_m] \{\delta\} \quad (4.19)$$

There are two approaches in getting explicit expression of $\{N_m\}$ over the element. Since all the matrices in Eq.(4.19) are in closed form, it can be used to formulate explicit $[K_G^e]$ by direct substitution. The other approach is to interpolate $\{N_m\}$ using the discrete membrane forces obtained at sampling points. Since the displacements of the L.S.T. membrane element are complete quadratic functions of area coordinates over the element, the resulting

strains are linear and so are the stresses and membrane forces. Any linear function of area coordinates can be uniquely determined by three function values defined at three different points over the area. Eq.(4.19) involves the product of three matrices and one vector, which has twenty four components, meanwhile only the membrane forces at sampling points are used in the latter approach. Therefore, when Eq.(4.19) is substituted directly, the corresponding expression for $[K_G^e]$ will be lengthy and will include additional twenty four independent variables which can be reduced to nine in the latter approach. In the sensitivity analysis, the number of derivative calculation is proportional to the number of independent variables in the formulation of the geometric stiffness matrix. For these reasons, the distribution of membrane forces are interpolated linearly over the element using the forces at three Gaussian points.

After the membrane forces are obtained from Eq.(4.19) at three Gaussian points, they are linearly interpolated as,

$$N_x = [1 \quad \xi_1 \quad \xi_2] \begin{Bmatrix} b_1 \\ b_2 \\ b_3 \end{Bmatrix} \quad (4.20)$$

which results in

$$N_x = [1 \quad \xi_1 \quad \xi_2] [B]^{-1} \begin{Bmatrix} N_{x1} \\ N_{x2} \\ N_{x3} \end{Bmatrix} \quad (4.21)$$

where

$$[B] = \begin{bmatrix} 1 & 1/6 & 1/6 \\ 1 & 2/3 & 1/6 \\ 1 & 1/6 & 2/3 \end{bmatrix} \quad (4.22)$$

and N_{xi} is the membrane force obtained at i th gaussian points. Similarly, N_y and N_{xy} can be expressed in terms of resultant forces at Gaussian points and area coordinates. As a

result, only nine components of membrane forces are required for the interpolation of the three membrane forces over the element

Another constituent matrix of geometric stiffness matrix, $[G]$, can be expressed in closed form as

$$[G] = \begin{Bmatrix} [0] & [0] & [N_x] & [0] \\ [0] & [0] & [N_y] & [0] \end{Bmatrix} \quad (4.23)$$

where explicit form of $[N_x]$ and $[N_y]$ are given in Eqs. (4.5) and (4.6).

With all the matrices in Eq. (3.56) in closed form of the local nodal coordinates and material properties, the geometric stiffness matrix in local coordinates is obtained in closed form by integrating each component analytically after the matrix product is computed by symbolic manipulation such as

$$[K_G^e] = \frac{1}{J} [\bar{K}_e] \quad (4.24)$$

where

$$[\bar{K}_e] = \iint_A [G] \begin{bmatrix} N_x & N_y \\ N_y & N_x \end{bmatrix} [G] J dA \quad (4.25)$$

Combined with the closed form transformation matrix, it can be explicitly written in the global coordinate system such as

$$[K_e] = \frac{1}{J} [\Lambda]^T [\bar{K}_e] [\Lambda] \quad (4.26)$$

Chapter 5

Analytic Sensitivities

5.1 Introduction

This chapter presents the calculation of the analytic sensitivity of the buckling load and the sensitivities of static structural responses (displacements and stresses) computed from the finite element analysis. Recall that the displacement is obtained from the following system of equations

$$[K]\{U\} = \{F\} \quad (5.1)$$

Both $[K]$ and $\{F\}$ are, in general, functions of design variables q_i . A typical function of displacement will be represented as

$$g = g(q_i, \{U\}), \quad \{U\} = \{U(q_i)\} \quad (5.2)$$

A straightforward method of calculating derivatives of g is to use a finite difference approximation such as

$$\frac{dg}{dq_i} \cong \frac{g[q_i + h, \{U(q_i + h)\}] - g[q_i, \{U(q_i)\}]}{h} \quad (5.3)$$

Finite difference schemes have been widely used in the shape optimization because of their simplicity, generality and the ease of incorporation into existing finite element codes (BOT81). The shortcomings of this method are the computational cost involved due to the need to run as many analyses as there are design variables, in addition to the original

analysis, and the difficulty in choosing the step size for the design variables. Both too-large and too-small step sizes can cause excessive truncation or round-off errors.

There are two methods for analytical calculations of derivatives of displacements and their functions. The variational methods involve differentiating the continuum equations governing the structural response (CH83, HCK86), whereas the implicit differentiation method is based on derivatives of the discrete equations of finite element. Both methods involve fewer computations than the finite difference approaches (which requires repeated factorization of the stiffness matrix), since they require a single factorization for all design variables. Some of the differences and relative merits of both approaches are described in the literature (YB86, HG86, ARO95).

The implicit differentiation method begins with the differentiation of Eqs. (5.1) and (5.2).

$$[K] \frac{d\{U\}}{dq_i} = \frac{\partial\{F\}}{\partial q_i} - \frac{\partial[K]}{\partial q_i} \{U\} \quad (5.4)$$

$$\frac{dg}{dq_i} = \frac{\partial g}{\partial q_i} + \left(\frac{\partial g}{\partial \{U\}} \right)^T \frac{\partial \{U\}}{\partial q_i} \quad (5.5)$$

When the sensitivity analysis is with respect to the sizing design variable q_i (such as thickness of plates or the cross-sectional area of a rod), then $\frac{\partial[K]}{\partial q_i}$ is a constant matrix.

However if the design variables involve the shape or the boundary of the structure, the resulting stiffness matrix is generally an implicit functions of the design variables q_i . Thus, the analytic evaluation of $\frac{\partial[K]}{\partial q_i}$ is harder to obtain for shape design variables than for the sizing design variables. Consequently finite difference technique has been a major tool for the numerical evaluation of $\frac{\partial[K]}{\partial q_i}$. This is called the Semi-Analytical method (HGK90).

While this method is simple and easy to implement for general finite element analysis, it is subject to truncation and condition errors which strongly depends on the step size (BCH88, CGZ89). Analytic evaluations of $\frac{\partial [K]}{\partial q_i}$ have been suggested for the isoparametric finite element in which numerical integrations are used for the formulation of stiffness matrix (WSG85, BRO87, BL88), . These methods are straight-forward but their calculations are lengthy and computationally expensive because the sensitivity with respect to nodal position must be obtained at each Gaussian point.

Recently analytic sensitivity calculations using explicit formulation of stiffness matrix have been reported (WBNL92, LL97, LIV94). Since all evaluations of the global stiffness matrix are explicit in the design variables, the calculation of $\frac{\partial [K]}{\partial q_i}$ can be easily done easily by applying chain rules, without the need for numerical integration. However, the above mentioned sensitivity calculations were limited to static finite element analyses, which only consider stress and displacement constraints in the optimization process.

Although shape optimization with buckling constraints is very important, most of the reported optimization results with buckling constraints were for problems involving sizing design variables (RGS94). This is due to the numerical complexities in calculating the sensitivities of buckling loads with respect to shape design variables. Recent attempts in shape optimization with buckling constraints based on finite element analysis are reported by Botkin (BOT94), but the method of calculating sensitivities was not shown. Also Ref.LM95 presented derivations of analytic shape sensitivity with buckling constraints, using explicit expressions for the stiffness and geometric stiffness matrices based on Ritz analysis for wing skin panels. However, the problem of global buckling including sub-component interactions was not addressed in that work.

In this chapter, analytic sensitivities of the stiffness and geometric stiffness matrices are derived based on the explicit formulation of the flat shell element which were derived in Chapter 4. These derivatives are then used to obtain the analytic shape sensitivity of the buckling load.

5.2 Sensitivities of Static Displacement and Stresses

In the early days of structural shape design sensitivity analysis and optimization, attempts were made to use the nodal coordinates of a finite element model as design variables. However, this approach caused large set of design variables and could lead to inadequate shape for the final design. Polynomial or spline representation of boundaries and the design element concept, in which the location of the key nodes is a set of design variables, have been proposed to reduce the number of design variables and to achieve an adequate finite element model.

When design variable affects the nodal positions, non-zero derivatives may occur for the element area A , the strain-displacement matrix, the coordinate transformation matrix and for the material properties of a composite material. First the derivatives of node locations in the global coordinates, $\frac{\partial \Psi_i}{\partial q_i}$ are calculated. Using the derivative of the transformation matrix which can be done by calculating the derivative of individual component, the derivative of global stiffness matrix can be written as

$$\frac{\partial [K]}{\partial q_i} = \frac{\partial [\Lambda]^T}{\partial q_i} [K^e] [\Lambda] + [\Lambda]^T \frac{\partial [K^e]}{\partial q_i} [\Lambda] + [\Lambda]^T [K^e] \frac{\partial [\Lambda]}{\partial q_i} \quad (5.6)$$

The derivatives of nodal locations in the local coordinates ψ_k are calculated using chain rules:

$$\frac{\partial \psi_k}{\partial q_i} = \frac{\partial \psi_k}{\partial \Psi_j} \frac{\partial \Psi_j}{\partial q_i} \quad (5.7)$$

As the components of element stiffness matrix are explicit functions of the location of nodes in local coordinates, the derivative of the element stiffness matrix can be obtained as

$$\frac{\partial [K^e]}{\partial q_i} = \frac{\partial [K^e]}{\partial \psi_k} \frac{\partial \psi_k}{\partial q_i} \quad (5.8)$$

An explicit form of the bending element has been derived in the former chapter as

$$[K^b] = \frac{1}{J} [R]^T [\bar{S}] [R] \quad (5.9)$$

where both $[R]$ and $[\bar{S}]$ contain nodal coordinates, and the material properties are included in $[\bar{S}]$. Since the bending stiffness matrix for orthotropic or anisotropic materials depends on the direction of the local coordinates system, which is calculated from nodal locations in the global coordinates, the derivatives of material properties must be included in that case.

Thus the derivative of bending stiffness is

$$\frac{\partial [K^b]}{\partial q_i} = \frac{\partial [K^b]}{\partial \psi_k} \frac{\partial \psi_k}{\partial q_i} + \frac{\partial [K^b]}{\partial \Psi_j} \frac{\partial \Psi_j}{\partial q_i} \quad (5.10)$$

where

$$\frac{\partial [K^b]}{\partial \psi_k} = \frac{\partial \left(\frac{1}{J} \right)}{\partial \psi_k} [R]^T [\bar{S}] [R] + \frac{1}{J} \left(\frac{\partial [R]^T}{\partial \psi_k} [\bar{S}] [R] + [R]^T \frac{\partial [\bar{S}]}{\partial \psi_k} [R] + [R]^T [\bar{S}] \frac{\partial [R]}{\partial \psi_k} \right) \quad (5.11)$$

$$\frac{\partial [K^b]}{\partial \Psi_j} = \frac{1}{J} [R]^T \frac{\partial [\bar{S}]}{\partial \Psi_j} [R] \quad (5.12)$$

Similarly, for the membrane stiffness matrix

$$\frac{\partial [K^m]}{\partial q_i} = \frac{\partial [K^m]}{\partial \psi_k} \frac{\partial \psi_k}{\partial q_i} + \frac{\partial [K^m]}{\partial \Psi_j} \frac{\partial \Psi_j}{\partial q_i} \quad (5.13)$$

where

$$\frac{\partial [K^m]}{\partial \psi_k} = \frac{\partial \left(\frac{1}{J} \right)}{\partial \psi_k} [\bar{K}^m] + \frac{1}{J} \frac{\partial [\bar{K}^m]}{\partial \psi_k} \quad (5.14)$$

$$\frac{\partial [K^m]}{\partial \Psi_j} = \frac{1}{J} \frac{\partial [\bar{K}^m]}{\partial \Psi_j} \quad (5.15)$$

After the sensitivity of the force vector is known, the sensitivity of displacement $\frac{\partial U}{\partial q_i}$ is obtained from Eq.(5.4). By taking derivatives of Eq.(5.4), the sensitivity of the geometric stiffness is obtained:

$$\begin{aligned} \frac{\partial [K_g]}{\partial q_i} = & \frac{\partial \left(\frac{1}{J} \right)}{\partial q_i} [\Lambda]^T [\bar{K}_g] [\Lambda] + \\ & \frac{1}{J} \left(\frac{\partial [\Lambda]^T}{\partial q_i} [\bar{K}_g] [\Lambda] + [\Lambda]^T \frac{\partial [\bar{K}_g]}{\partial q_i} [\Lambda] + [\Lambda]^T [\bar{K}_g] \frac{\partial [\Lambda]}{\partial q_i} \right) \end{aligned} \quad (5.16)$$

As $[\bar{K}_g]$ is a function of the membrane forces at three Gaussian points, as well as the nodal coordinates, the sensitivity can be obtained by

$$\frac{\partial [\bar{K}_g]}{\partial q_i} = \frac{\partial [\bar{K}_g]}{\partial \psi_k} \frac{\partial \psi_k}{\partial q_i} + \frac{\partial [\bar{K}_g]}{\partial \{N_{mk}\}} \frac{\partial \{N_{mk}\}}{\partial q_i} \quad (5.17)$$

The recovery of resultant membrane forces can be done by combining Eqs. (3.33) and (3.36) as

$$\{N_m\} = [D_m] [B_m] [T_m] \{\delta\} \quad (5.18)$$

Since the derivatives of the three matrices and the sensitivity of the displacement are available, the sensitivities of the membrane forces are calculated easily at the three Gaussian points as

$$\begin{aligned} \frac{\partial \{N_{mk}\}}{\partial q_i} = & \frac{\partial [D_m]}{\partial q_i} [B_m] [T_m] \{\delta\} + [D_m] \frac{\partial [B_m]}{\partial q_i} [T_m] \{\delta\} + \\ & [D_m] [B_m] \frac{\partial [T_m]}{\partial q_i} \{\delta\} + [D_m] [B_m] [T_m] \frac{\partial \{\delta\}}{\partial q_i} \end{aligned} \quad (5.19)$$

5.3 Sensitivities of Buckling Load and Buckling Modeshapes

Recall that buckling load is obtained through the generalized eigenvalue problem

$$[K] + \lambda_i [K_g] \{\phi_i\} = \{0\} \quad (5.20)$$

where $[K]$ and $[K_g]$ are the stiffness and geometric stiffness matrices, and λ_i and $\{\phi_i\}$ are the i th buckling load coefficient and buckling mode, respectively. As both matrices are real and symmetric, the eigenvalue λ_i is real and the equation can be rewritten as

$$\{\phi_i\}^T [K] + \lambda_i [K_g] \{\phi_i\} = \{0\}^T \quad (5.21)$$

Differentiating these equations with respect to a design variable one obtains

$$\left[\frac{\partial [K]}{\partial q_i} + \lambda_i \frac{\partial [K_g]}{\partial q_i} + \frac{\partial \lambda_i}{\partial q_i} [K_g] \right] \{\phi_i\} + [K] + \lambda_i [K_g] \left\{ \frac{\partial \phi_i}{\partial q_i} \right\} = \{0\} \quad (5.22)$$

When this is pre-multiplied by the transpose of buckling mode vector $\{\phi_i\}^T$, one can get the sensitivity of buckling load coefficient as

$$\frac{\partial \lambda_i}{\partial q_i} = - \frac{\{\phi_i\}^T \left[\frac{\partial K}{\partial q_i} + \lambda_i \frac{\partial K_g}{\partial q_i} \right] \{\phi_i\}}{\{\phi_i\}^T K_g \{\phi_i\}} \quad (5.23)$$

using Eq. (5.21), which eliminates the term associated with the sensitivity of buckling mode $\left\{ \frac{\partial \phi_i}{\partial q_i} \right\}$ from Eq. (5.22).

The sensitivity of the eigenvector with respect to the design variable is obtained by Eq. (5.22),

$$[B_i] \left\{ \frac{\partial \phi_i}{\partial q_i} \right\} = \{F_i\} \quad (5.24)$$

where

$$[B_i] = \left[[K] + \lambda_i [K_g] \right] \quad (5.25)$$

$$\{F_i\} = - \left[\frac{\partial [K]}{\partial q_i} + \lambda_i \frac{\partial [K_g]}{\partial q_i} + \frac{\partial \lambda_i}{\partial q_i} [K_g] \right] \quad (5.26)$$

Since the matrix on the left-hand side of Eq.(5.24) is singular, the eigenvector derivatives cannot be obtained from this. However, several methods for computing the eigenvector derivatives have been developed in the literature(AH86), some of them use analytic procedure while others are based on simplified procedure. It is usual for the analysis of large structural systems to use a truncated set of mode shapes, and the eigenvector derivatives can not be obtained using the analytic procedure, since it requires all the mode shapes. The simplified method which requires only the eigenvector and the associated eigenvalue under consideration has been developed by Nelson(NEL76) and that procedure for calculating the eigenvector sensitivity is repeated in this section.

As the eigenvector $\{\phi_i\}$ is the homogeneous solution of Eq. (5.24) with $\{F_i\} = \{0\}$, the solution can be approximated as

$$\left\{ \frac{\partial \phi_i}{\partial q_i} \right\} = \{V_i\} + c_i \{\phi_i\} \quad (5.27)$$

Since the norm of the eigenvector does not depend on the design variable, a differentiation of it with respect to design variable will give

$$\left\{ \frac{\partial \phi_i}{\partial q_i} \right\} \{\phi_i\} = \{0\} \quad (5.28)$$

After substiting Eq. (5.27) into Eq. (5.28) , the coefficient c_i becomes

$$c_i = \frac{-\{V_i\}^T \{\phi_i\}}{\{\phi_i\}^T \{\phi_i\}} \quad (5.29)$$

the matrix on the left hand side may be partitioned as

$$\begin{bmatrix} [B_i]_{11} & \{B_i\}_{1k} & [B_i]_{13} \\ [B_i]_{k1} & [B_i]_{kk} & [B_i]_{k3} \\ [B_i]_{31} & \{B_i\}_{3k} & [B_i]_{33} \end{bmatrix} \begin{Bmatrix} V_1 \\ v_k \\ V_3 \end{Bmatrix} = \begin{Bmatrix} F_1 \\ f_k \\ F_3 \end{Bmatrix} \quad (5.30)$$

where $\{B_i\}_{1k}$ and $\{B_i\}_{3k}$ are column matrices, $[B_i]_{k1}$ and $[B_i]_{k3}$ are row matrices, and $[B_i]_{kk}$ is the (k,k) th element of $[B_i]$, V_1 and V_3 are partitioned subvectors, and v_k is the k th component of the vector $\{V_i\}$. Then, by taking as the pivotal element the component of $\{V_i\}$ at the location k where the absolute value of eigenvector is maximum, the partitioned system becomes

$$\begin{bmatrix} [B_i]_{11} & [B_i]_{13} \\ [B_i]_{31} & [B_i]_{33} \end{bmatrix} \begin{Bmatrix} V_1 \\ V_3 \end{Bmatrix} = -v_k \begin{Bmatrix} \{B_i\}_{1k} \\ \{B_i\}_{3k} \end{Bmatrix} + \begin{Bmatrix} F_1 \\ F_3 \end{Bmatrix} \quad (5.31)$$

Since the matrix on the left-hand side is not singular, the solution for V_1 and V_3 can be obtained by simply setting $v_k = 0$. The complete solution for the eigenvector derivatives is then

$$\left\{ \frac{\partial \phi_i}{\partial q_i} \right\} = \begin{Bmatrix} V_1 \\ 0 \\ V_3 \end{Bmatrix} + c_i \begin{Bmatrix} \Phi_1 \\ \phi_k \\ \Phi_3 \end{Bmatrix} \quad (5.32)$$

where Φ_1 and Φ_3 are partitioned subvectors, and ϕ_k is the k th component of the vector $\{\phi_i\}$.

In practice, the system can be solved directly using the same banded-equation solving routines used for solving the displacement vector, by simply taking out the k th row and k th column of $[B_i]$, except for the diagonal element, and putting zero for the k th element of the right-hand side vector.

$$\begin{bmatrix} [B_i]_{11} & 0 & [B_i]_{13} \\ 0 & 1 & 0 \\ [B_i]_{31} & 0 & [B_i]_{33} \end{bmatrix} \begin{Bmatrix} V_1 \\ v_k \\ V_3 \end{Bmatrix} = \begin{Bmatrix} F_1 \\ 0 \\ F_3 \end{Bmatrix} \quad (5.33)$$

Chapter 6

Order Reduction and Approximations

6.1 Introduction

In the design of complex structures, it is often necessary or desirable to use approximate analyses at various stages of the optimization process in order to reduce the computational cost and required computer storage. This is especially true in the case of global/local buckling analysis, when finite element models have to be detailed enough to capture sub-component behavior as well as global behavior. As a result, techniques for reducing the number of degrees of freedom have been widely used in dynamic analysis and automated optimum design (FM71), as well as in nonlinear analysis (NOO81), because of the excessive amounts of computer time associated with the repetitive evaluation of behavior functions.

In structural optimization problems with buckling constraints, buckling eigenvalues must be evaluated for successive modifications of the structure. With closed form formulae for the stiffness and geometric stiffness of individual elements, such as for the shell elements used in this work, it is computationally efficient to evaluate the stiffness and geometric stiffness matrices for a new configuration. Thus, most of the computational cost associated with repetitive solutions is related to the eigensolution procedures themselves, even with small number of degrees of freedom. The numerical solution of eigenvalue problems is time consuming and computationally burdensome. Order reduction of models

of large-scale structures with buckling constraints will lead to smaller eigenvalue problems and therefore less cost .

The essence of structural order reduction methods is to limit the deformation modes of the discretized structure to some set of known modes (basis vectors), which are considerably smaller in number than the number of degrees of freedom of the initial discretization. In aeroelasticity and structural dynamics analyses this has been done successfully for years using sets of low-frequency natural vibration modes of the structure. However, there is a marked difference between airplane flutter problems and buckling problems. Flutter of the complete airplane involves motions which can be successfully described by linear superposition of low frequency vibration modes, and include some overall global motion of wings and fuselage structures. However, buckling of the complete airframe will usually show up as a local problem e.g. the local buckling of a panel together with neighboring support structure. For a set of base vectors (deformation shape functions) to be capable of capturing both local and global deformation patterns, this set must usually include many degrees of freedom. The resulting savings in terms of numbers of degrees of freedom become less and less significant. Actually, even in structural dynamics and aeroelasticity, when the local behavior of the structure becomes important, such as in a case of a structural model capable of simulating dynamic behavior for both global and local panel flutter modes, the selection of low frequency vibration modes for order reduction will usually not lead to reliable reduced order models, unless the number of modes is very large.

In this chapter, the focus is on the application of modeshapes to the order reduction of the eigensystem, which is composed of either exact evaluations of both $[K]$ and $[K_G]$ or the first order approximations of those matrices based on the sensitivities of an unperturbed full order analysis when the shape design variables are changed.

6.2 Reduced System of Equations

In linear buckling analysis of a structure, the system is given from

$$\left[[K] + \lambda_i [K_G] \right] \{\phi_i\} = \{0\} \quad (6.1)$$

where $[K]$ and $[K_G]$ are stiffness and geometric stiffness matrices of order n , λ_i and $\{\phi_i\}$ are eigenvalue and corresponding eigenvector.

A Rayleigh-Ritz technique is used to replace Eq. (6.1) by a reduced system of equations. This is accomplished by approximating $\{\phi_i\}$ by a linear combination of r linearly independent vectors $\{X\}_1, \{X\}_2, \dots, \{X\}_r$, where r is much less than n , i.e.

$$\{\phi_i\} \cong [\Gamma] \{\psi\} \quad (6.2)$$

where

$$[\Gamma] = [\{X\}_1, \{X\}_2, \dots, \{X\}_r] \quad (6.3)$$

and $\{\psi\}$ is a vector of undetermined coefficients which are obtained by solving the reduced system. This reduced system is obtained by substituting Eq. (6.2) into Eq. (6.1) and pre-multiplying the resulting equation by $[\Gamma]^T$:

$$\left[[\tilde{K}] + \lambda_i [\tilde{K}_G] \right] \{\psi\} = \{0\} \quad (6.4)$$

where

$$\begin{aligned} [\tilde{K}] &= [\Gamma]^T [K] [\Gamma] \\ [\tilde{K}_G] &= [\Gamma]^T [K_G] [\Gamma] \end{aligned} \quad (6.5)$$

As a result, an approximate eigenvector $\{\psi\}$ and corresponding eigenvalue λ'_i can be obtained by solving the smaller order system in Eq. (6.4) to approximate the full order solution $\{\phi_i\}$ and λ_i obtained by solving the full system of Eq. (6.1). Each component of the vector $\{\psi\}$ represents the contributions of an assumed modeshape to the approximated modeshape as

$$\{\phi_i\} = \psi_1 \cdot \{X\}_1 + \psi_2 \cdot \{X\}_2 + \dots + \psi_r \cdot \{X\}_r \quad (6.6)$$

The sensitivity of the reduced order eigenvalues can be calculated using

$$\frac{\partial \lambda'_i}{\partial q_i} = - \frac{\{\psi_i\}^T \left[\frac{\partial [\tilde{K}]}{\partial q_i} + \lambda'_i \frac{\partial [\tilde{K}_G]}{\partial q_i} \right] \{\psi_i\}}{\{\psi_i\}^T [\tilde{K}_G] \{\psi_i\}} \quad (6.7)$$

in which the sensitivities of the reduced matrices can be obtained by differentiating Eqs. (6.5) and (6.6) such as

$$\begin{aligned} \frac{\partial [\tilde{K}]}{\partial q_i} &= \frac{\partial [\Gamma]^T}{\partial q_i} [K] [\Gamma] + [\Gamma]^T \frac{\partial [K]}{\partial q_i} [\Gamma] + [\Gamma]^T [K] \frac{\partial [\Gamma]}{\partial q_i} \\ \frac{\partial [\tilde{K}_G]}{\partial q_i} &= \frac{\partial [\Gamma]^T}{\partial q_i} [K_G] [\Gamma] + [\Gamma]^T \frac{\partial [K_G]}{\partial q_i} [\Gamma] + [\Gamma]^T [K_G] \frac{\partial [\Gamma]}{\partial q_i} \end{aligned} \quad (6.8)$$

When the sensitivities of assumed eigenvectors are not available, the resulting sensitivities are obtained by ignoring them:

$$\begin{aligned} \frac{\partial [\tilde{K}]}{\partial q_i} &= [\Gamma]^T \frac{\partial [K]}{\partial q_i} [\Gamma] \\ \frac{\partial [\tilde{K}_G]}{\partial q_i} &= [\Gamma]^T \frac{\partial [K_G]}{\partial q_i} [\Gamma] \end{aligned} \quad (6.9)$$

6.3 Selection of Eigenvectors

Successive evaluations of Eq. (6.1) are required in the structural optimization process with buckling constraint. For the approximation of eigenvectors analysis when the design variables are changed, here two methods are considered using the results from a base full order analysis done at $q_i = q_{i0}$.

The first approach is to approximate the eigenvectors using a truncated set of former eigenvectors evaluated at the base configuration.

$$\{\phi_i(q_i)\} \cong \sum_{k=1}^r \psi_k \cdot \{\phi_k(q_{i0})\} \quad (6.10)$$

where

$$q_i = q_{i0} + \delta q_i \quad (6.11)$$

This is the “fixed modes” approach, in which the assumption is that, as the design changes, critical buckling modeshapes do not change as fast as the buckling eigenvalues, and that a subset of the buckling modeshapes at the base design is capable through some linear combination of its members to capture the buckling shapes of the changed configuration..

The second approach is a “variable modes” method, in which a Taylor series expansion is used to approximate the new buckling modeshapes:

$$\{\phi_i(q_i)\} \cong \sum_{k=1}^r \psi_k \cdot \left[\{\phi_k(q_{i0})\} + \frac{\partial \{\phi_k\}}{\partial q_i} \Big|_{q_{i0}} \delta q_i \right] \quad (6.12)$$

The sensitivities of eigenvectors with respect to design variables are obtained analytically as explained in Chapter 4. Now the order reduction process involves two steps. First, a new set of base vectors is generated at a modified design point using Eq. (6.11). These new vectors are then used to create the order reduction transformation matrix in Eq. (6.3),

which, in turn, is used with the new modified stiffness and geometric stiffness matrices to create the reduced order eigenproblem Eq. (6.4).

6.4 Approximations

The nonlinear constrained structural optimization problem can be mathematically written as follows:

$$\text{Minimize: } F(q) \quad (6.13)$$

$$\text{Subject to : } g_k(q) \leq 0 \quad (6.14)$$

where $F(q)$ is the objective function (which usually is the weight of the structure) and g_k are the constraint functions. If the constraint is related to the buckling of the structures, Eq. (6.14) can be rewritten as

$$g_k(q_i) = 1 - \lambda_i \leq 0 \quad (6.15)$$

i.e., the ratio of the buckling load to the applied load must be greater than unity.

In modern structural optimization based on sensitivity analysis, the optimum solution is found by applying linear/nonlinear programming to approximations of objective and constraint functions, which can be explicit but are usually implicit functions of design variables. There are three kinds of approximation methods in which first-order derivatives are used, the direct, reciprocal and conservative approximations. Direct approximations are obtained by using truncated Taylor series expansions with respect to the design variable, which can be mathematically written as

$$g_k(q_{i0} + \delta q_i) = g_k(q_{i0}) + \left. \frac{\partial g_k}{\partial q_i} \right|_{q_{i0}} \cdot \delta q_i \quad (6.16)$$

where

$$\delta q_i = (q_i - q_{i,0}) \quad (6.17)$$

If the reciprocal of the variable $\gamma_i = 1/q_i$ is defined as intermediate variable, the resulting first order approximations with respect to the intermediate variable can be obtained as in Eq. (6.12) and the reciprocal approximations with respect to the original design variable are

$$g_k(q_{i,0} + \delta q_i) = g_k(q_{i,0}) + \frac{\partial g_k}{\partial \left(\frac{1}{q_i}\right)} \bigg|_{q_{i,0}} \left(\frac{1}{q_i} - \frac{1}{q_{i,0}} \right) = g_k(q_{i,0}) + \frac{\partial g_k}{\partial q_i} \bigg|_{q_{i,0}} \frac{q_{i,0}}{q_i} \delta q_i \quad (6.18)$$

The conservative approximations are defined as

$$g_k(q_{i,0} + \delta q_i) = g_k(q_{i,0}) + G_{ki} \cdot \frac{\partial g_k}{\partial q_i} \bigg|_{q_{i,0}} \cdot \delta q_i \quad (6.19)$$

where

$$G_{ki} = \begin{cases} 1 & \text{when } \frac{\partial g_k}{\partial q_i} \bigg|_{q_{i,0}} \geq 0 \\ \frac{q_i}{q_{i,0}} & \text{when } \frac{\partial g_k}{\partial q_i} \bigg|_{q_{i,0}} < 0 \end{cases} \quad (6.20)$$

The conservative approximations are equivalent to direct approximation when sensitivity is positive and is equivalent to reciprocal approximation when the sensitivity is negative, so that the bigger estimate of the function is obtained in a conservative way. In the case where the cross sectional properties of structural elements (for example truss, membrane and plate element) are used as design variables, the element stiffness matrix is a product of design variables and a constant matrix, and structural responses like displacements and stresses are inversely proportional to stiffness. Therefore, in designing these structures, it is convenient to use as design variables the reciprocal of cross sectional properties, which leads direct

approximation of stiffness and reciprocal approximation of structural responses, without loss of accuracy. However, when shape design variables are used in the structural optimization, the relationship between stiffness and design variables becomes highly nonlinear, which requires considerable insight in choosing approximation methods for the structural responses. Moreover, if the constraints are related to more complicated structural responses like natural frequencies or buckling loads, the approximation techniques should be used with extreme caution, and needs to be modified to deal with the general nature of the problems. Since the buckling load can be treated as either objective function or constraint, the approximations of buckling load are discussed in this section.

6.4.1 Approximations based on analytic sensitivity

Since the analytic sensitivity is available in Eq. (5.23), the approximation of buckling loads can be constructed by applying this sensitivity to Eqs. (6.18) and (6.19).

For the direct approximation:

$$\lambda(q_i) = \lambda_0 + \left. \frac{\partial \lambda}{\partial q_i} \right|_{q_{i,0}} \cdot (q_i - q_{i,0}) \quad (6.21)$$

For the Reciprocal approximation:

$$\lambda(q_i) = \lambda_0 + \left. \frac{\partial \lambda}{\partial q_i} \right|_{q_{i,0}} \frac{q_{i,0}}{q_i} \cdot (q_i - q_{i,0}) \quad (6.22)$$

6.4.2 Order Reduction using the Approximate Eigensystem.

Whereas the matrices in Eq. (6.5) can be calculated exactly at the modified design variable, q_i with their sensitivities as shown in Chapter 4., they also can be obtained from

the approximations based on the former sensitivity results, $\frac{\partial[K]}{\partial q_i}$ and $\frac{\partial[K_G]}{\partial q_i}$ at $q_i = q_{i0}$

such as:

Direct approximation :

$$\begin{aligned} [K(q_i)] &= [K(q_{i0})] + \left. \frac{\partial[K]}{\partial q_i} \right|_{q_{i0}} (q_i - q_{i0}) \\ [K_G(q_i)] &= [K_G(q_{i0})] + \left. \frac{\partial[K_G]}{\partial q_i} \right|_{q_{i0}} (q_i - q_{i0}) \end{aligned} \quad (6.23)$$

Reciprocal approximation :

$$\begin{aligned} [K(q_i)] &= [K(q_{i0})] + \left. \frac{\partial[K]}{\partial q_i} \right|_{q_{i0}} \frac{q_{i0}}{q_i} (q_i - q_{i0}) \\ [K_G(q_i)] &= [K_G(q_{i0})] + \left. \frac{\partial[K_G]}{\partial q_i} \right|_{q_{i0}} \frac{q_{i0}}{q_i} (q_i - q_{i0}) \end{aligned} \quad (6.24)$$

Now the buckling load are obtained by solving reduced eigen problem in Eq. (6.4), in which reduced matrices in Eq.(6.5) are produced by substituting approximate $[K]$ and $[K_G]$ without calculating the exact matrices.

6.4.3 Rayleigh Quotient Approximations

When only one basis vector is used to approximate eigenvector in Eq. (6.2) , the buckling loads can be approximated directly from the Rayleigh quotient :

$$\lambda_i = \frac{\{\phi_i\}^T [K] \{\phi_i\}}{-\{\phi_i\}^T [K_G] \{\phi_i\}} = \frac{V}{W} \quad (6.29)$$

where V represents the linear modal strain energy and W the nonlinear(geometric) strain energy of the buckling mode. We use the modeshapes from the full order analysis as the basis vector and only system matrices needs to be approximated to estimate the buckling load as the design variable changes. The Rayleigh quotients using r basis vectors will be identical to the eigenvalues of reduced system in Eq. (6.4) if one ignores off-diagonal terms of both $[\tilde{K}]$ and $[\tilde{K}_G]$, which measure the coupling effects of the basis vectors on the eigenvector for the modified design variable. Since the modeshapes are orthogonal to each other with respect to system matrices at the reference variable, this orthogonality can affect the off-diagonal term in reduced matrices when the change of matrices caused by modified design variable is not too large. In this case the eigenvalues obtained from the reduced system and the Rayleigh quotient are nearly identical.

When the eigenvector is approximated the corresponding estimation of the eigenvalue from the Rayleigh quotient can either overestimate or underestimate the exact value, depending on the approximations of system matrices as the shape design variable changes. Since an overestimation of buckling load is what the designer wants to avoid in the redesign process, it is important to achieve the conservative estimate of buckling load using the appropriate approximations of system matrices. Thus, the conservative Rayleigh quotient approximation(CRQA) of buckling load is formed according to this criteria as

$$\lambda_{CRQA} = \frac{V_{app}}{W_{app}} = \frac{V_0 + G_{vi} \frac{\partial V}{\partial q_i}(q_{i0} - q_i)}{W_0 + G_{wi} \frac{\partial W}{\partial q_i}(q_{i0} - q_i)} \quad (6.30)$$

where

$$\frac{\partial V}{\partial q_i} = \{\phi\}^T \frac{\partial [K]}{\partial q_i} \{\phi\} \Big|_{q_i=q_{i0}} \quad (6.31)$$

$$\frac{\partial W}{\partial q_i} = -\{\phi\}^T \frac{\partial [K_G]}{\partial q_i} \{\phi\} \Big|_{q_i=q_{i,0}} \quad (6.32)$$

$$G_{vi} = \begin{cases} 1 & \text{when } \frac{\partial V}{\partial q_i} < 0 \\ q_{i,0}/q_i & \text{when } \frac{\partial V}{\partial q_i} \geq 0 \end{cases} \quad (6.33)$$

$$G_{wi} = \begin{cases} 1 & \text{when } \frac{\partial W}{\partial q_i} \geq 0 \\ q_{i,0}/q_i & \text{when } \frac{\partial W}{\partial q_i} < 0 \end{cases} \quad (6.34)$$

V_0 is the linear modal strain energy and W_0 the geometric modal strain energy of the reference design. In this approximation, conservative approximations are used for both V and W in order to achieve conservative estimate of buckling load. When sizing design variables are considered, the stiffness is a product of design variable and constant matrix and the stiffness matrix is positive definite. In this case, the linear modal strain energy is underestimated by using the reciprocal approximation, which reduces the Rayleigh Quotient when it is combined with conservative approximation of W . This approximation, called RQA(Rayleigh Quotient Approximation), has been successfully adopted for the design of frames against buckling with sizing design variables(CAN93). However, in the case of shape design variables, the linearity between stiffness and design variable doesn't exist, and RQA might not give a conservative estimate of buckling loads, as can be seen in reference LM95.

Chapter 7

Numerical Results (Verification and Sensitivities)

A finite element code based on the preceding chapters using FORTRAN has been developed. A detail flow chart can be found in Appendix C. In this chapter, numerical results of the proposed analytic shape sensitivity analysis are presented for both two and three dimensional structures. First the accuracy of the method is verified for simple cases of homogeneous isotropic and orthotropic plates for which theoretical solutions are available in the literature, that is followed by cases for anisotropic laminated plates. Subsequently the shape sensitivity analysis of the buckling loads for wing-like structures are presented.

7.1 Simply Supported Rectangular Plates with Uniform Compression

The buckling of rectangular plates has been widely discussed in the literature(TG61). Since the theoretical solution is available for certain special cases of loads and boundary conditions, they were selected as examples to asses the accuracy of the finite element buckling analysis and sensitivity analysis. A rectangular plate subjected to biaxial compression is illustrated in Figure 7.1. A plate of length a , width b and constant thickness t is used. The plate is assumed to be either simply supported or clamped on its edges and two sets of loading conditions are considered: uniaxial compression and biaxial compression. In the uniaxial compression load $N_x = 1$ and $N_y = 0$ and, for the biaxial

compression load, $N_x = 1$, $N_y = 1$. In the sensitivity analysis, the length of the plate a is chosen as a shape design variable. The finite element approximations of the buckling load and its sensitivity are obtained for the isotropic, orthotropic and anisotropic laminated plates.

Since the structure and the applied loads are symmetric, only symmetric buckling mode is considered and thus only the part of the plate in the quadrant III is analyzed. Figure 7.2 shows examples of finite element mesh configurations when the length to width ratios are 1 and 3 respectively.

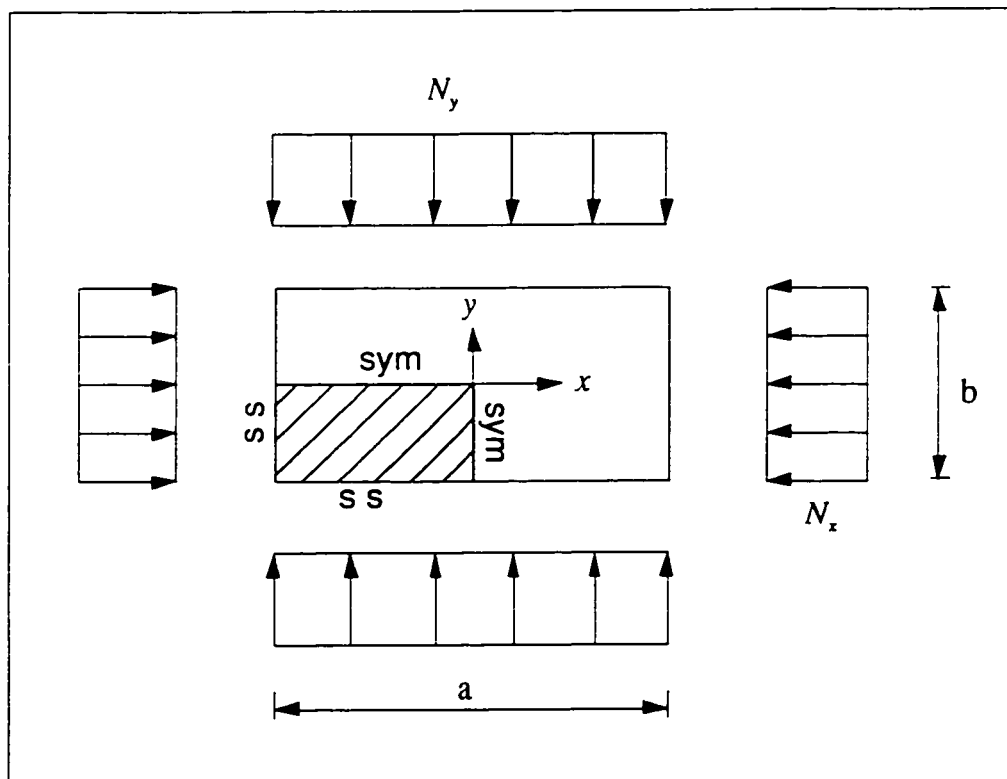


Figure 7.1 Rectangular plate subject to uniform compression

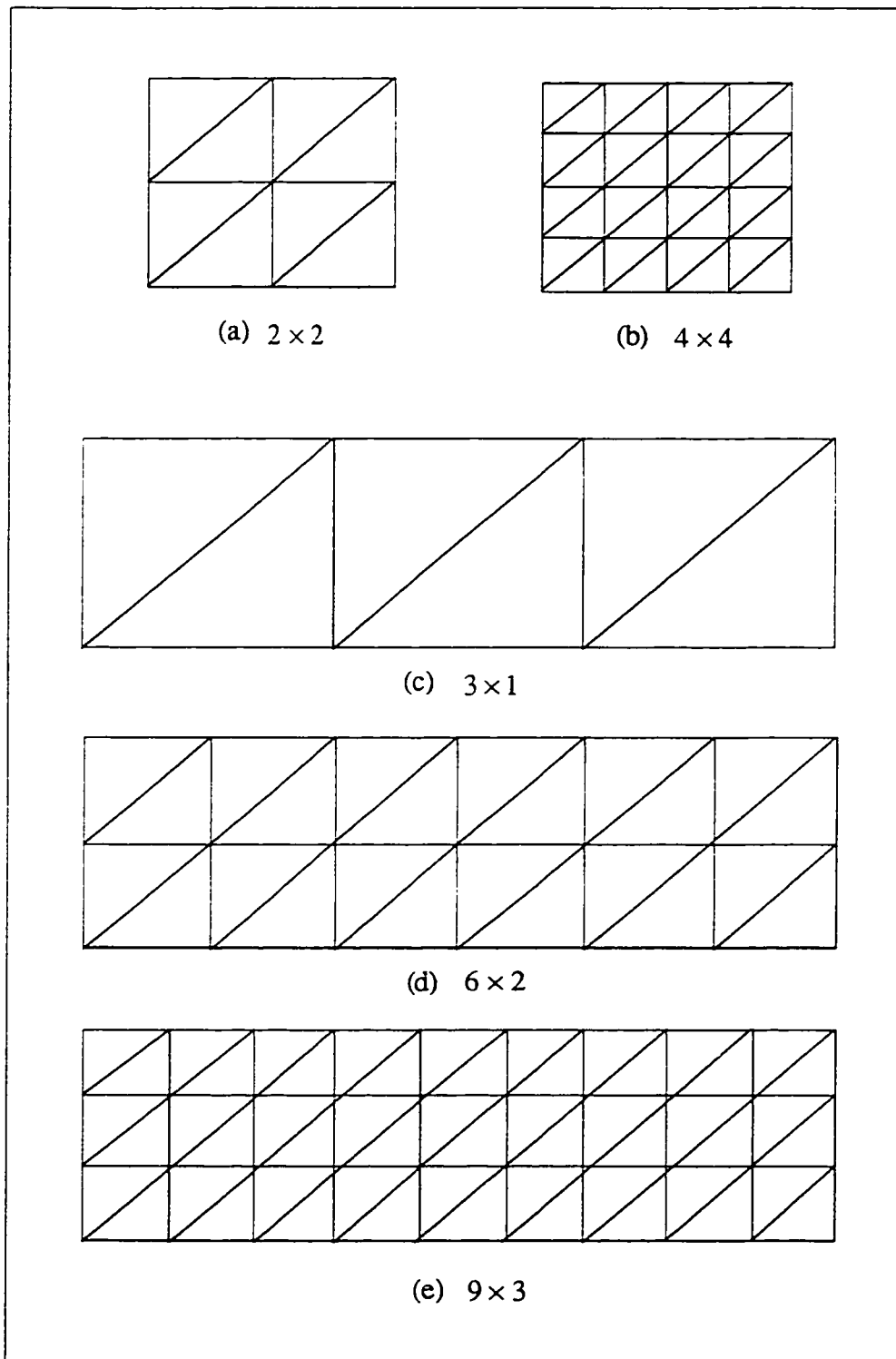


Figure 7.2 Finite element mesh configurations for rectangular plates

7.1.1 Isotropic Plates

The theoretical buckling load for simply supported isotropic plates is given (TG61) as

$$N_{cr} = k \frac{\pi^2 D}{b^2} \quad (7.1)$$

where

$$D = \frac{E t^3}{12(1-\nu^2)} \quad (7.2)$$

and buckling load coefficient k depends on the loading conditions.

For the uniaxial compression:

$$k = \left(m \frac{b}{a} + \frac{n^2 a}{m b} \right)^2 \quad (7.3)$$

and, for biaxial compression:

$$k = \left(\left(m \frac{b}{a} \right)^2 + n^2 \right) \quad (7.4)$$

Here m and n are the number of buckling half wavelengths in the x and y directions, respectively, and these numbers depend only on the aspect ratio $\frac{a}{b}$. For example, when the aspect ratio of the plate subject to uniaxial compression is less than $\sqrt{2}$, the critical buckling load occurs at $(m, n) = (1, 1)$ in Eq. (7.3) and the next minimum one at $(m, n) = (2, 1)$, and so on. Since only a quarter of the plate is analyzed using the symmetric boundary conditions, the corresponding finite element analysis gives the buckling solutions only for the symmetric modes in which m, n are odd numbers. In this example the approximation of buckling load and its sensitivity is examined not only for the first (primary) buckling mode but also for the next critical modes.

The corresponding theoretical sensitivity of the buckling force can be obtained by differentiating the theoretical buckling loads with respect to the shape design variable a :

$$\frac{dN_{cr}}{da} = \frac{\pi^2 D}{b^2} \frac{dk}{da} \quad (7.5)$$

where

$$\frac{dk}{da} = 2 \left(m \frac{b}{a} + \frac{n^2}{m} \frac{a}{b} \right) \left(-m \frac{b}{a^2} + \frac{n^2}{m} \frac{1}{b} \right) \quad (7.6)$$

$$\frac{dk}{da} = -2m^2 \frac{b^2}{a^3} \quad (7.7)$$

for the uniaxial and biaxial compression, respectively. The thickness of the plate $t = 0.1$ is assumed and the width of the plate b is set to 10 in this section. The material properties of isotropic material are :

$$E = 1.0 \times 10^7 \quad \nu = 0.3 \quad (7.8)$$

For a plate subject to uniaxial compression and with $\frac{a}{b} = 1.2$, the approximate buckling load coefficients k for the three critical modes are shown and compared with the theoretical ones in Table 7.1. Since the L.S.T. membrane element could produce a linear stress distribution, the constant membrane stress distribution over the plate produced by the uniaxial compression was exactly recovered and also the exact stress sensitivity, zero in this load case, was obtained. The number of buckling half wavelengths in the x and y directions for the critical three modes are given as $m = 1, 3, 5$ and $n = 1$ theoretically and the same mode shapes were obtained for all mesh densities except the third symmetric mode with 1×1 mesh. The three mode shapes obtained by finite element analysis with a 4×4 mesh are shown in Figures.7.3-7.5. As shown in Table 7.1, the critical buckling loads for the three modes are accurately isolated for each mode and the approximate buckling coefficients converge to the theoretical value as the number of finite elements is increased. It is observed that the present finite element analysis gives an accurate buckling solution for the primary mode using the coarse mesh. Even for a 1×1 mesh density, with only 17 d.o.f., the relative error of the primary buckling load is less than 3 %, as shown in

Figure 7.6. The accuracy of the buckling loads for the second and third modes is not as good as for the one for the primary mode with the coarse meshes, but the same order of accuracy was obtained with refined finite element meshes. When a 4×4 finite element mesh is used, the calculated buckling loads for all three symmetric modes range in errors from 0.03 to 3.8 percent.

The analytic shape sensitivities of the buckling loads were computed by solving the linear equations in Eq. (5.23). The calculated sensitivities from the theoretical solutions are shown in Table 7.2. and Figure 7.7 shows the normalized buckling load sensitivities with the changes of mesh density. It is observed that the calculated sensitivity converge monotonically to the theoretical solution as the mesh is refined. Since the formulation of the present sensitivity analysis is based on the same finite element formulation for the buckling analysis, the same order of accuracy is expected for the sensitivity results. The comparison of the normalized buckling loads and sensitivities can be seen in Figure 7.8. For all meshes, the sensitivity results are less accurate than the buckling loads. However, both results show good convergence to the theoretical solutions, and almost the same order of accuracy is obtained when the mesh is refined. For example, the relative errors of the buckling load and its sensitivity for the primary mode are 0.26 and 0.69 percents respectively using 2×2 mesh density.

Figure 7.9 illustrates the numerical results of buckling load and its sensitivity for the primary and second symmetric modes from the finite element analysis with a 4×4 mesh. In this figure, the sensitivity results are drawn as the slope of the buckling loads at given design variable. Both results show good agreement with the theoretical solutions.

Table 7.3 and 7.4 show the numerical results of buckling and sensitivity analysis when the same plate is subject to biaxial compression. The theoretical buckling mode shapes for the primary and second symmetric modes are identical to those of uniaxial load

case. The third symmetric mode has a different shape ($m = 1, n = 3$) and all three mode shapes are accurately captured in the buckling analysis. The normalized values of both results can be seen in Figure 7.10. In this figure, the numerical results for the primary and second symmetric modes show similar convergence tendency to those of the uniaxial load case, but the sensitivity for the third symmetric mode converges to the theoretical solution from above.

Table 7.1 Buckling coefficients for rectangular plate under uniaxial compression ($a/b = 1.2$).

	1st sym. mode ($m = 1, n = 1$)	2nd .sym. mode ($m = 3, n = 1$)	3rd sym. mode ($m = 5, n = 1$)
1 × 1 MESH	4.012	4.828	
2 × 2 MESH	4.124	7.763	15.712
3 × 3 MESH	4.132	8.277	17.009
4 × 4 MESH	4.134	8.367	18.685
5 × 5 MESH	4.134	8.392	19.120
Exact	4.134	8.410	19.419

Table 7.2 Buckling coefficient sensitivity for rectangular plate under uniaxial compression
($a/b = 1.2$)

	1st sym. mode ($m = 1, n = 1$)	2nd sym. mode ($m = 3, n = 1$)	3rd sym. mode ($m = 5, n = 1$)
1 × 1 MESH	.1016	-.3897	
2 × 2 MESH	.1235	-.8880	-2.0548
3 × 3 MESH	.1240	-.9900	-2.3377
4 × 4 MESH	.1241	-1.0075	-2.7140
5 × 5 MESH	.1241	-1.0124	-2.8162
Exact	.1242	-1.0150	-2.8839

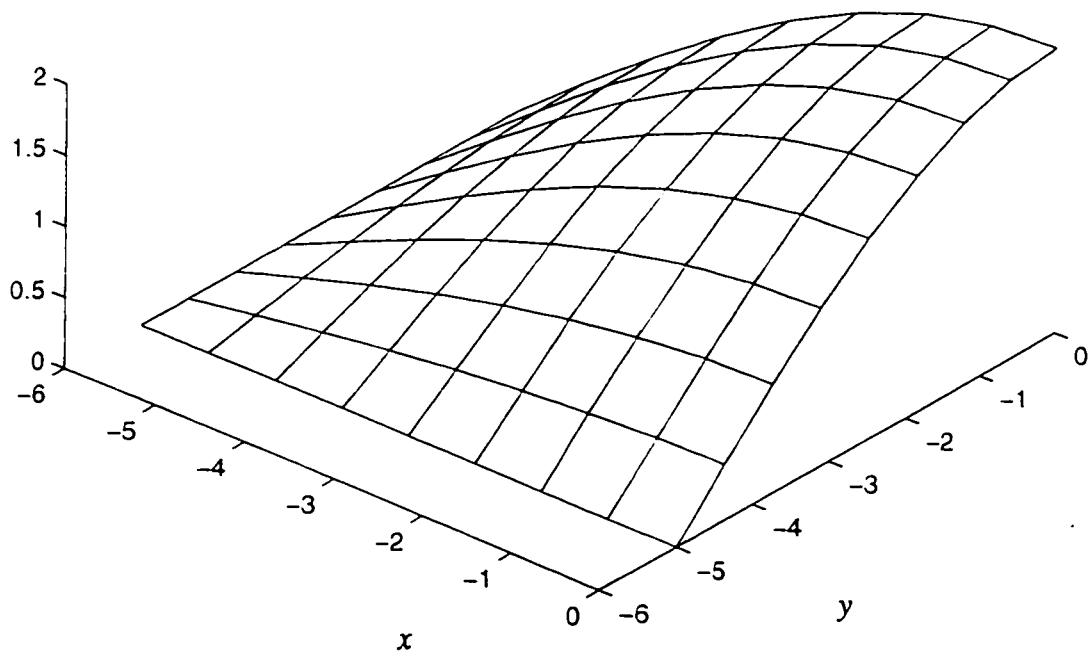


Figure 7.3 Mode shape for the first symmetric mode of a rectangular plate ($a/b = 1.2$)

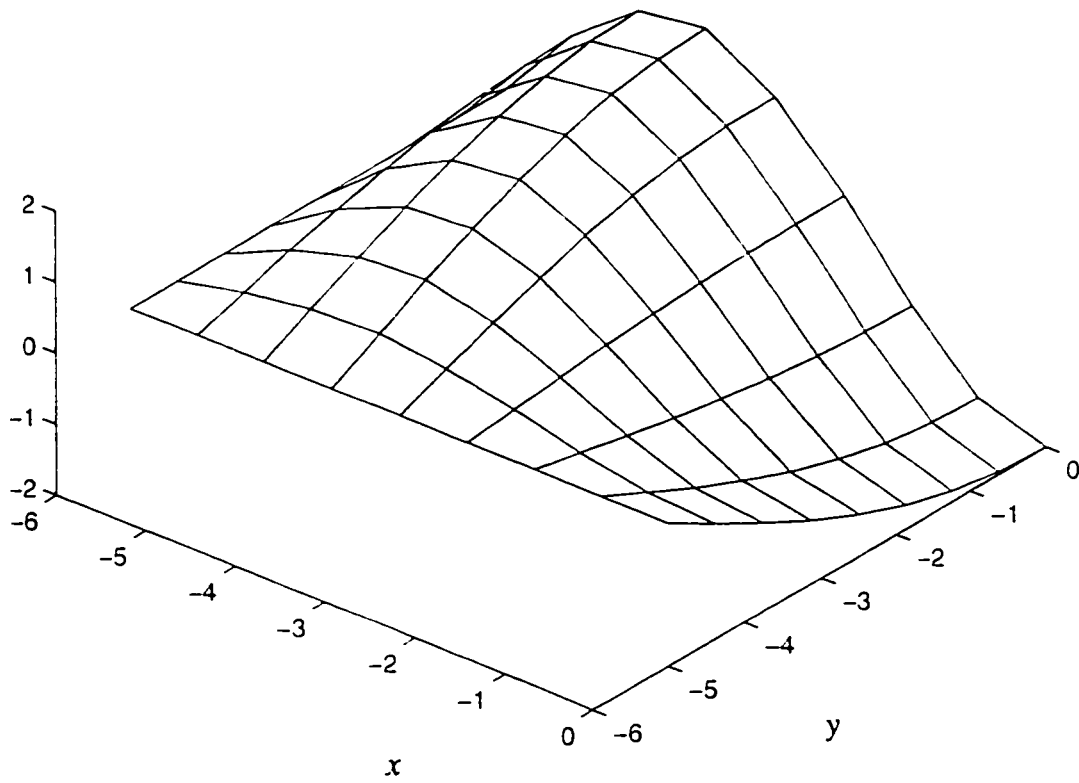


Figure 7.4 Mode shape for the second symmetric mode of a rectangular plate ($a/b = 1.2$)

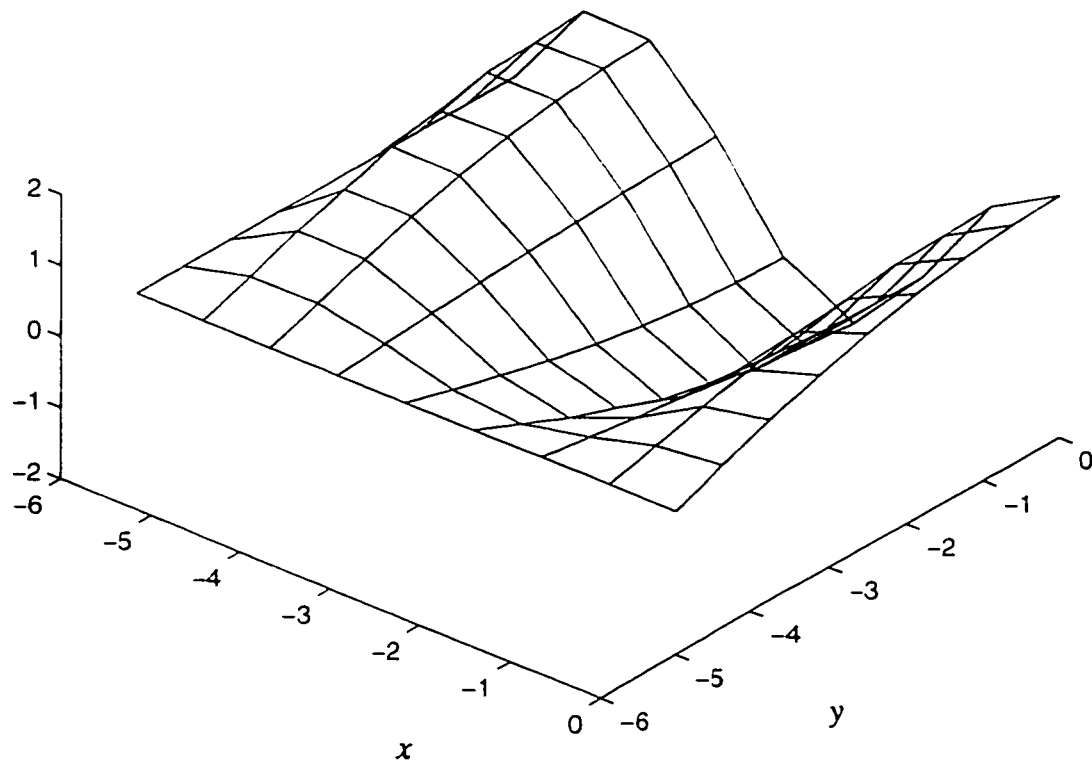


Figure 7.5 Mode shape for the third symmetric mode of a rectangular plate ($a/b = 1.2$)

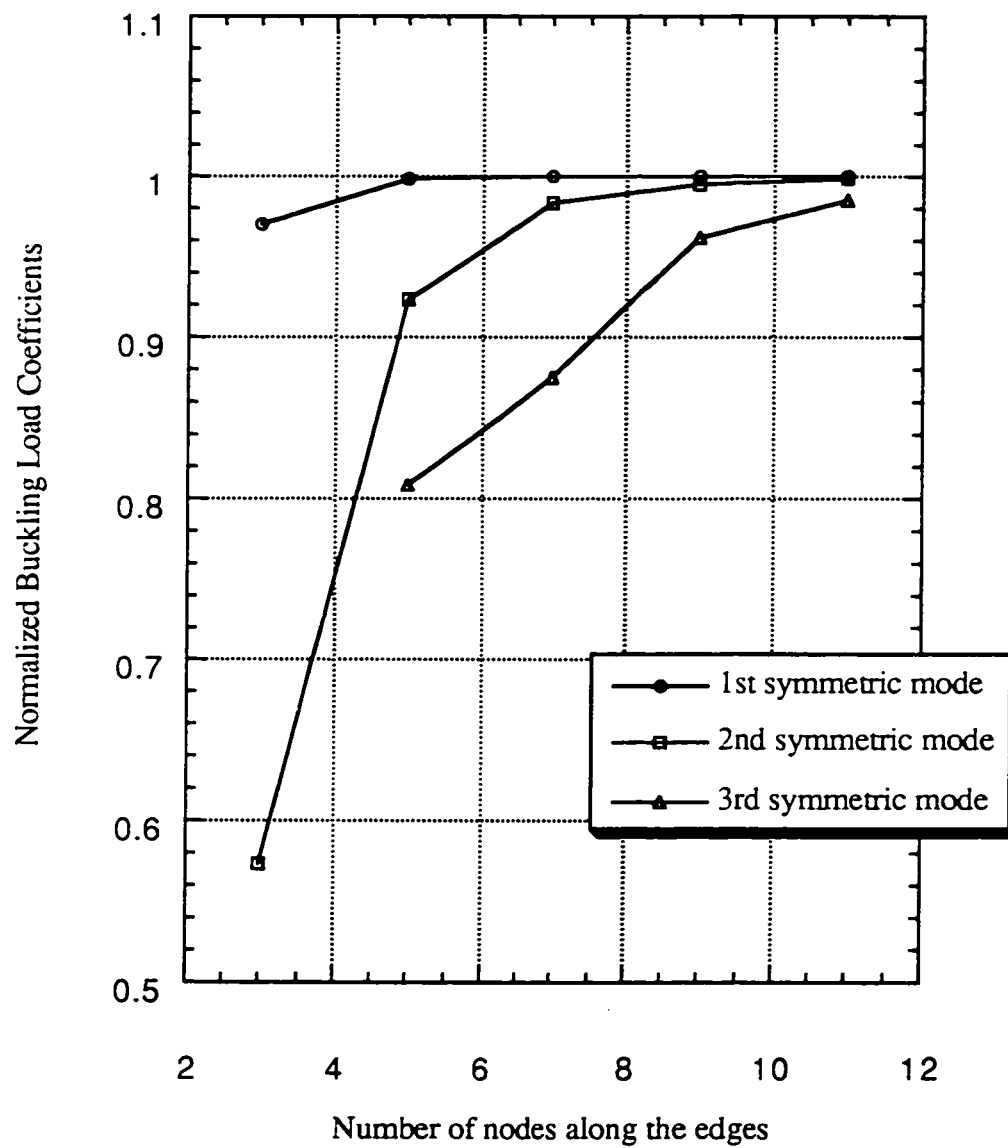


Figure 7.6 Convergence of buckling load for rectangular plate under uniaxial compression
($a/b = 1.2$)

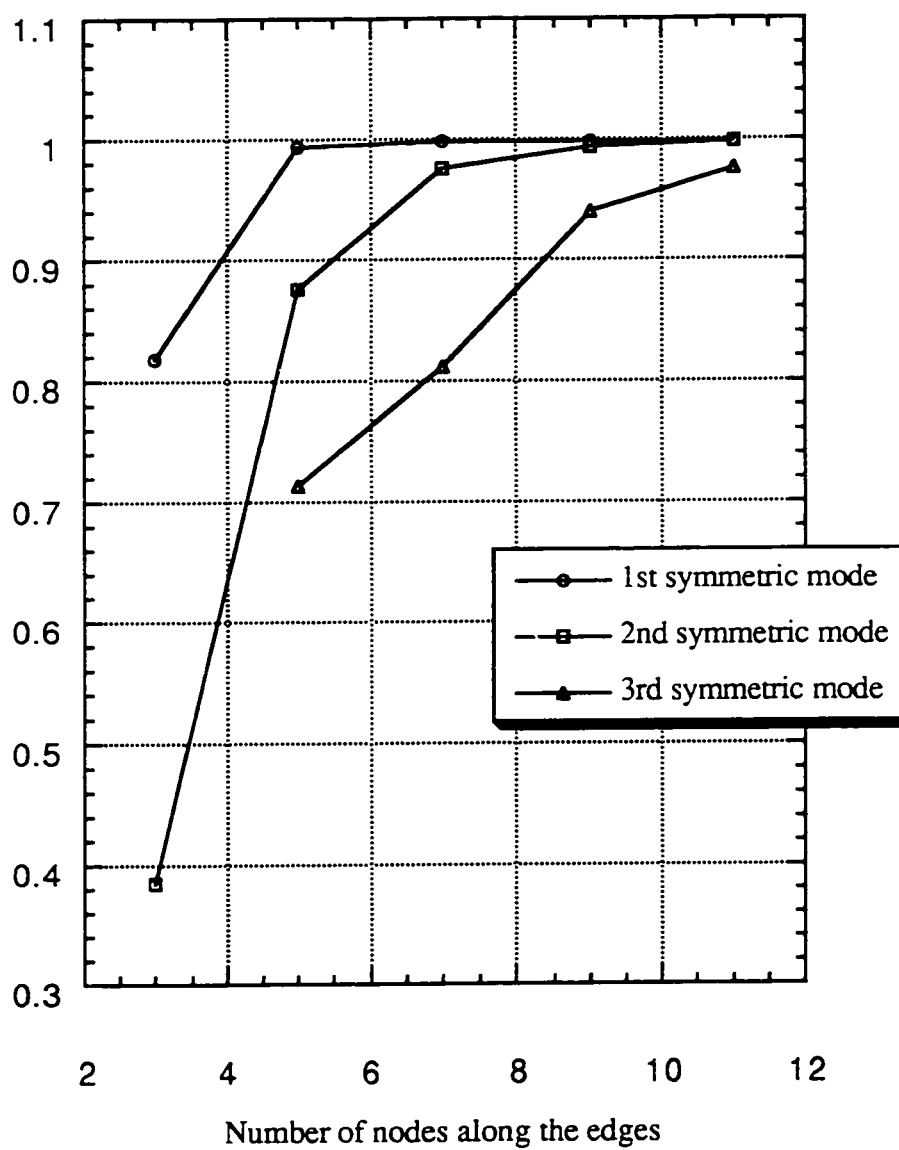


Figure 7.7 Convergence of buckling load sensitivity for rectangular plate under uniaxial compression ($a/b = 1.2$)

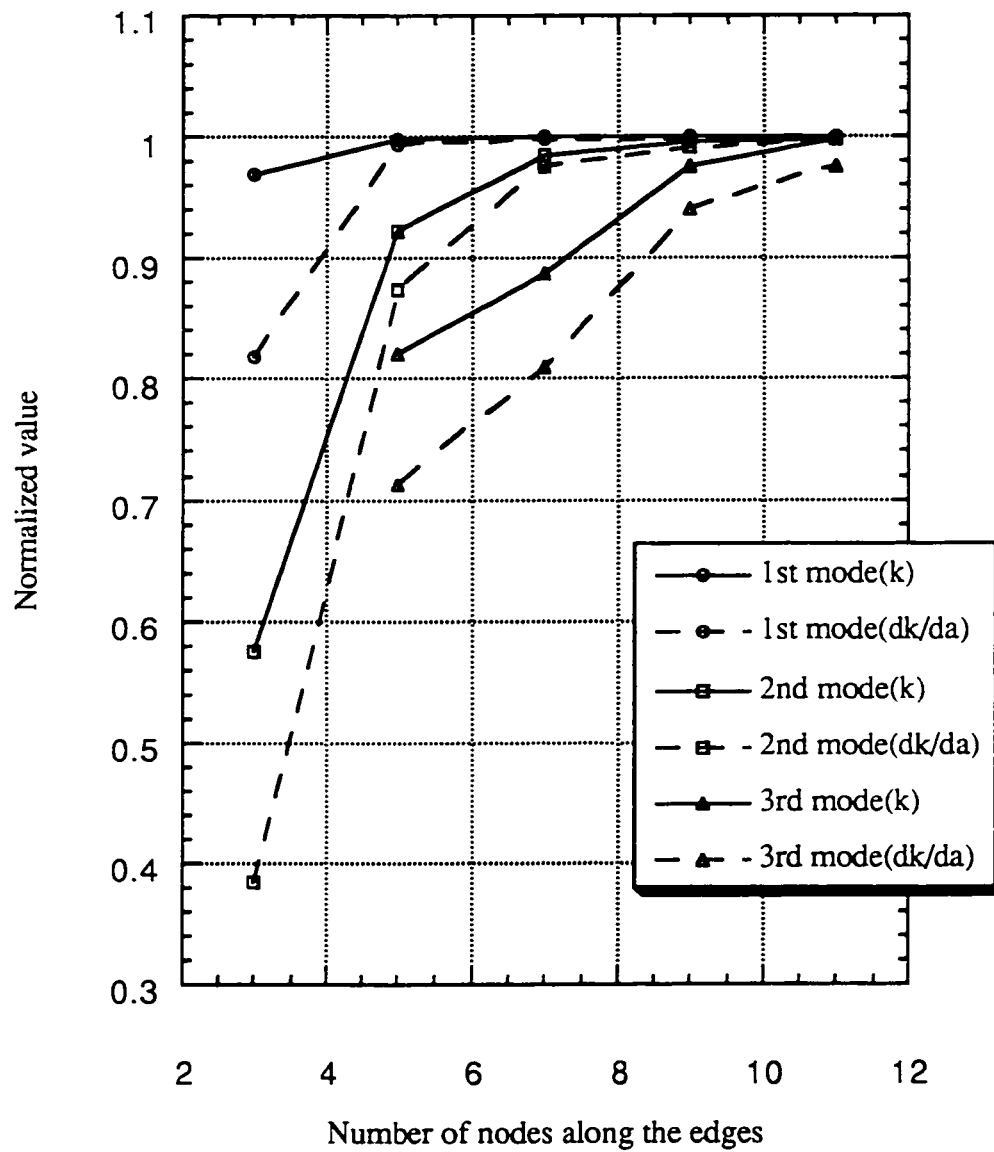


Figure 7.8 Normalized buckling load and sensitivity for the rectangular plate under uniaxial compression ($a/b = 1.2$)

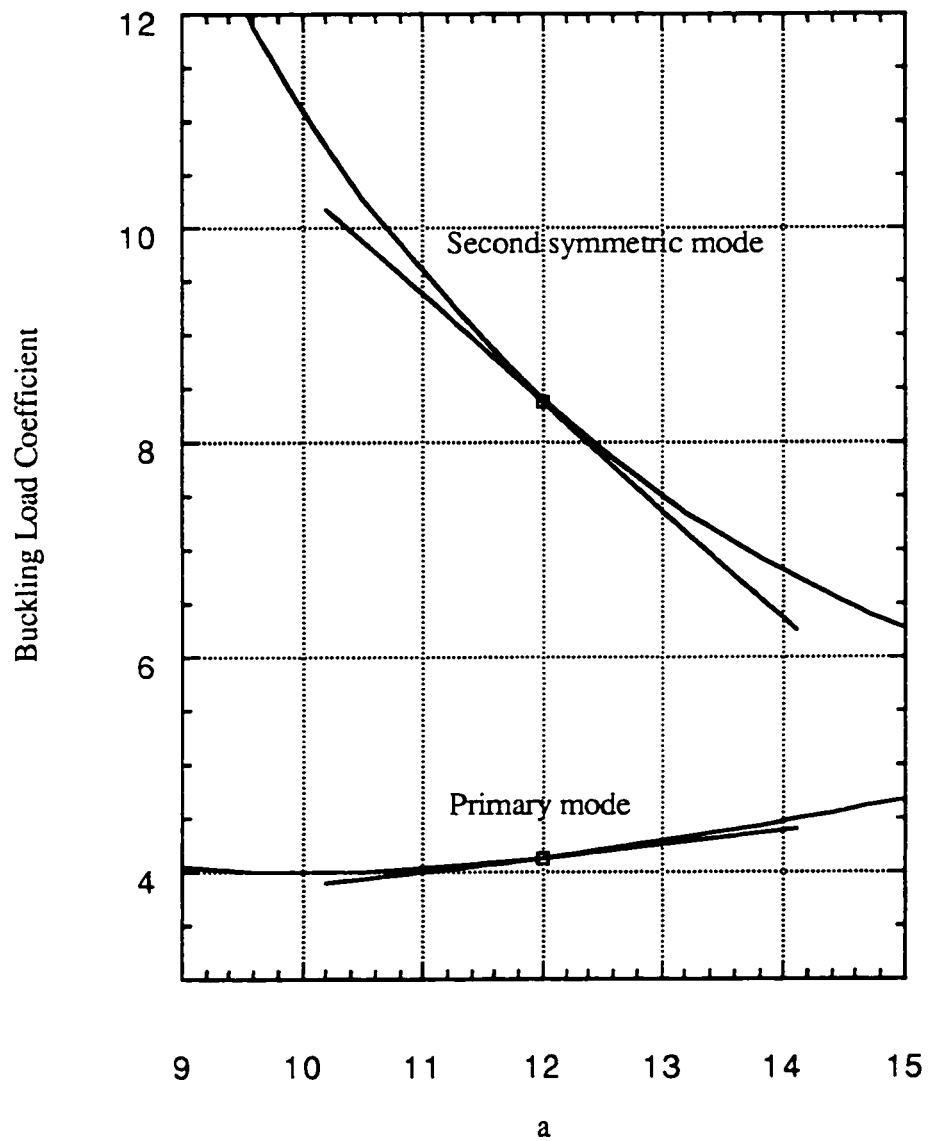


Figure 7.9 The sensitivity of Buckling Load Coefficients for the rectangular plate under uniaxial compression ($b = 10$)

Table 7.3 Buckling load coefficients for rectangular plate under biaxial compression
($a/b = 1.2$)

	1st sym. mode ($m = 1, n = 1$)	2nd sym. mode ($m = 3, n = 1$)	3rd sym. mode ($m = 1, n = 3$)
1 × 1 MESH	1.653	3.973	
2 × 2 MESH	1.690	6.645	8.497
3 × 3 MESH	1.693	7.129	9.456
4 × 4 MESH	1.694	7.211	9.620
5 × 5 MESH	1.694	7.234	9.664
Exact	1.694	7.250	9.694

Table 7.4 Buckling coefficient sensitivity for rectangular plate under biaxial compression
($a/b = 1.2$)

	1st sym. mode ($m = 1, n = 1$)	2nd sym. mode ($m = 3, n = 1$)	3rd sym. mode ($m = 1, n = 3$)
1 × 1 MESH	-.11337	-.4221	
2 × 2 MESH	-.11561	-.9129	-.2263
3 × 3 MESH	-.11575	-1.0169	-.1368
4 × 4 MESH	-.11577	-1.0343	-.1221
5 × 5 MESH	-.11577	-1.0390	-.1183
Exact	-.11574	-1.0417	-.1157

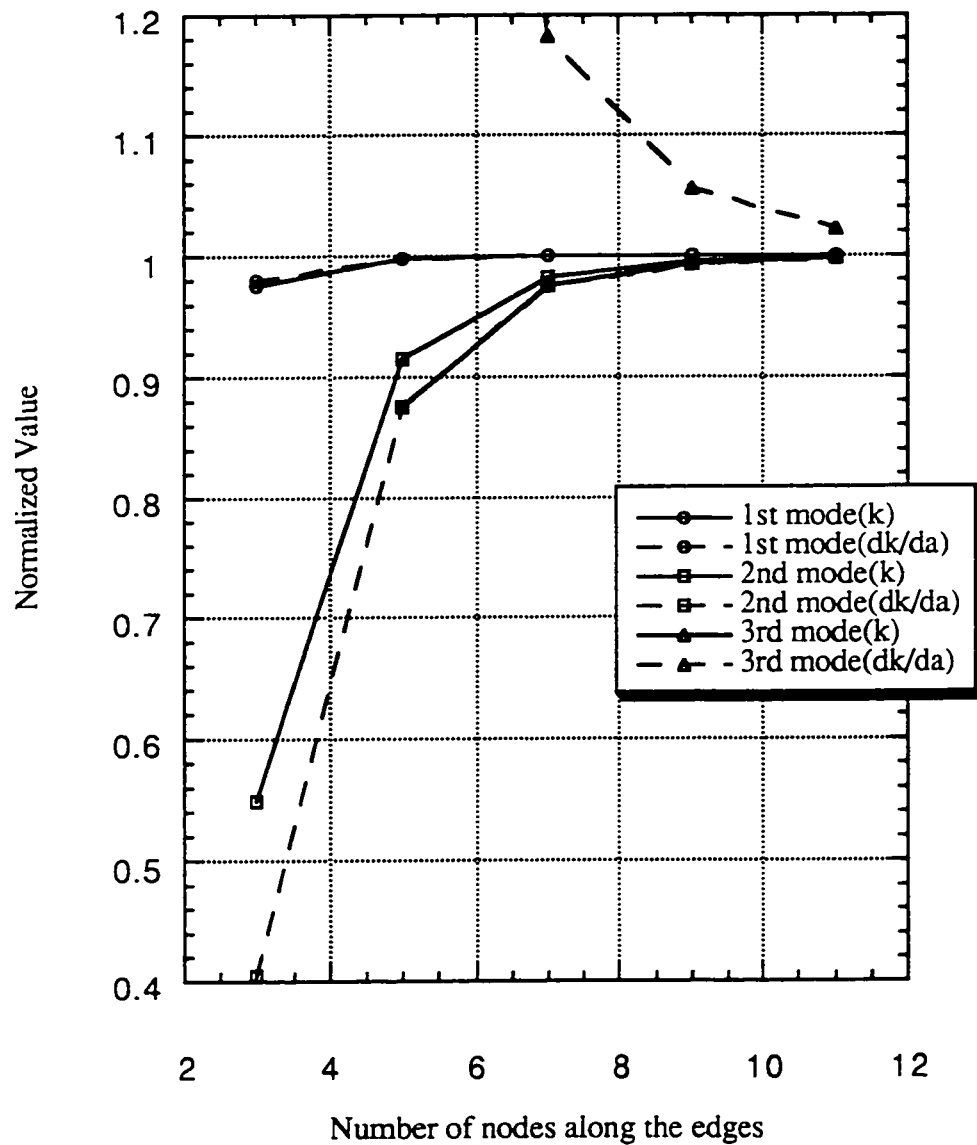


Figure 7.10 Convergence of buckling load and sensitivity for the rectangular plate under biaxial compression ($a/b = 1.2$)

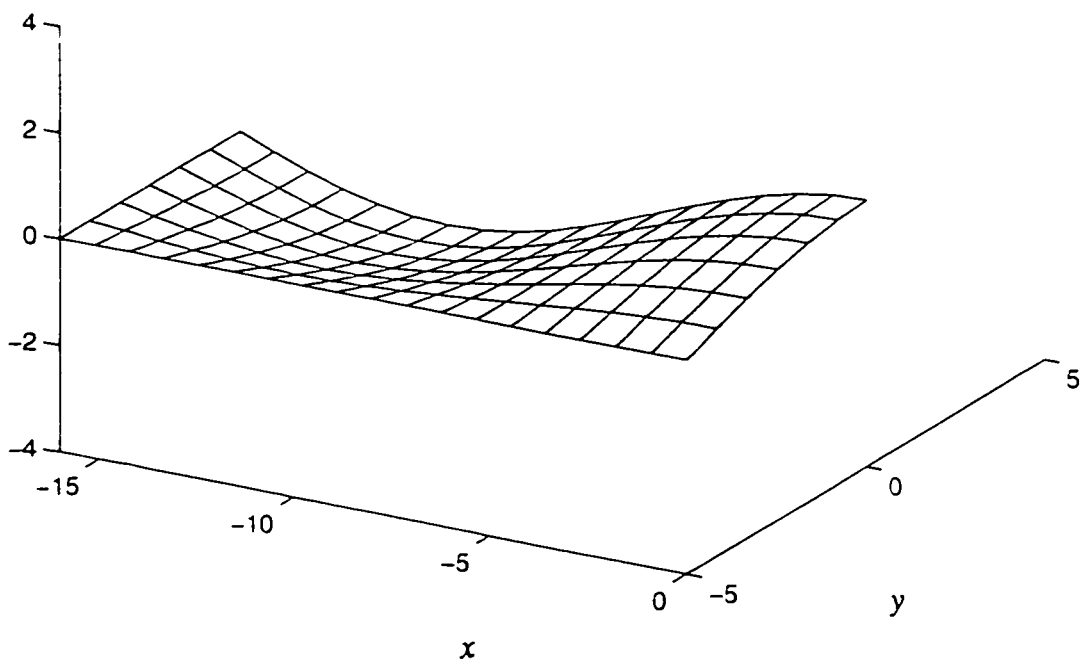


Figure 7.11 Mode shape for the first symmetric mode of a rectangular plate ($a/b = 3.2$)

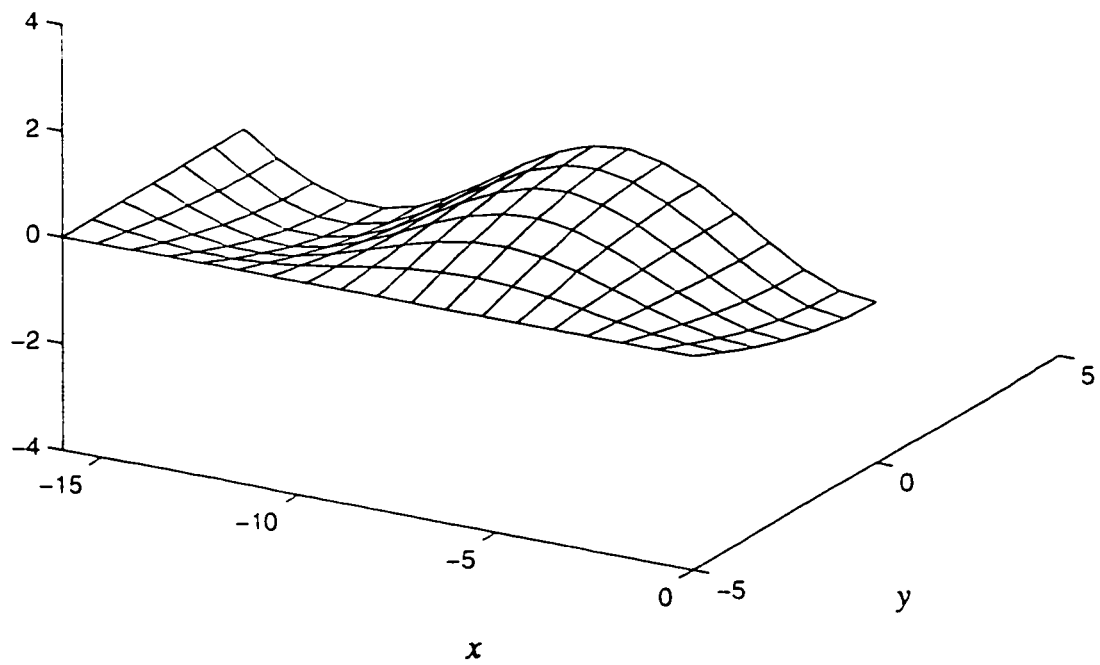


Figure 7.12 Mode shape for the second symmetric mode of a rectangular plate ($a/b = 3.2$)

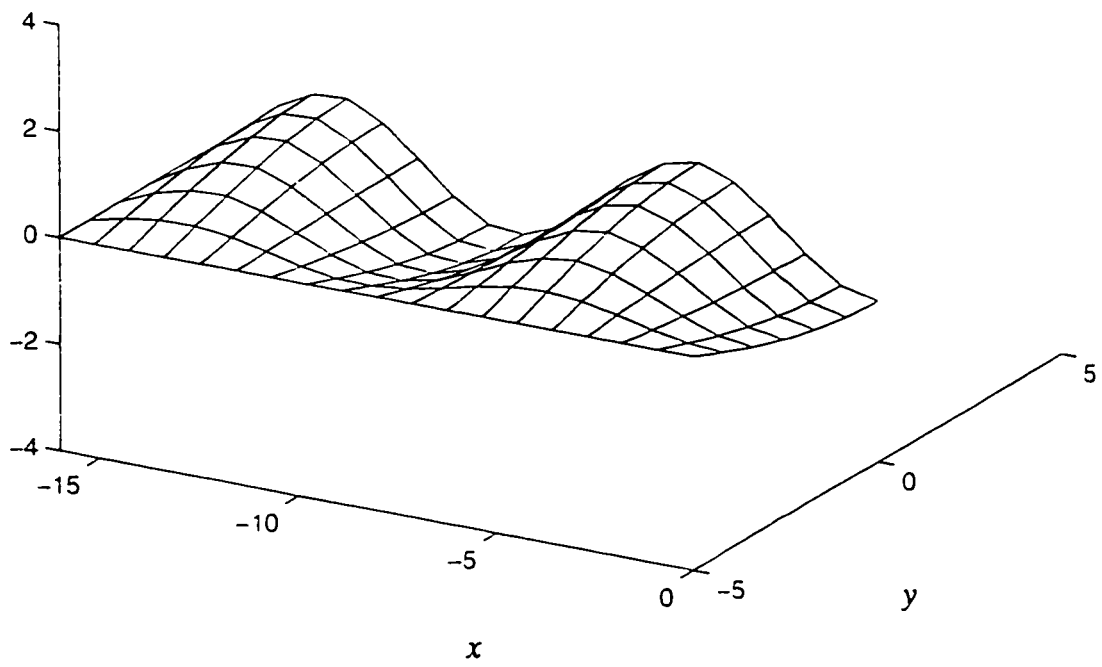


Figure 7.13 Mode shape for the third symmetric mode of a rectangular plate ($a/b = 3.2$)

Numerical results for a plate of different aspect ratio were evaluated to assess the accuracy of the buckling loads and their sensitivities. In this example a plate of aspect ratio $\frac{a}{b} = 3.2$, is used. The theoretical buckling loads and sensitivities for the first three symmetric modes for a plate subject to uniaxial compression are obtained by applying $m = 3, 5, 7$ and $n = 1$ to Eqs. (7.3) and (7.6); and, for a plate subject to biaxial compression by applying $m = 1, 3, 5$ and $n = 1$ to Eqs. (7.4) and (7.7). Figure 7.17 to 7.19 show the mode shapes obtained from the finite element analysis with a 9×3 mesh density for the uniaxial load case. The numerical results for various mesh densities of the plates under uniaxial and biaxial compressions can be seen in Table 7.5 and 7.6, in which sensitivity results are in the parenthesis. The normalized results are illustrated in Figures 7.14 and 7.15. It is observed in these figures that the buckling loads and corresponding sensitivities converge to the theoretical solutions as the number of elements in the finite element analysis is increased, for both load cases and the results for the biaxial load case are a little bit more accurate than the uniaxial load case. For example, the errors of critical k for the biaxial load case are in between 0.19 and 0.03 percents while those for the uniaxial load case are in between 4.5 and 0.07 percents.

Table 7.5 Buckling load coefficient and sensitivity for rectangular plate under uniaxial compression ($a/b = 3.2$)

	1st sym. mode ($m = 3, n = 1$)	2nd sym. mode ($m = 5, n = 1$)	3rd sym. mode ($m = 7, n = 1$)
3 × 1 MESH	3.838 (.0123)	4.173 (-.0946)	5.384 (-.1740)
6 × 2 MESH	4.004 (.0160)	4.797 (-.1246)	6.747 (-.2688)
9 × 3 MESH	4.014 (.0161)	4.840 (-.1256)	6.944 (-.2827)
Exact	4.017 (.0162)	4.851 (-.1270)	6.994 (-.2860)

Table 7.6 Buckling load coefficient and sensitivity for rectangular plate under biaxial compression ($a/b = 3.2$)

	1st sym. mode ($m = 1, n = 1$)	2nd sym. mode ($m = 3, n = 1$)	3rd sym. mode ($m = 5, n = 1$)
3 × 1 MESH	1.0766 (-.00675)	1.803 (-.0531)	2.943(-.1187)
6 × 2 MESH	1.0962 (-.00614)	1.873 (-.0548)	3.401 (-.1502)
9 × 3 MESH	1.0973 (-.00611)	1.878 (-.0549)	3.433 (-.1521)
Exact	1.0977 (-.00610)	1.879 (-.0549)	3.441 (-.1526)

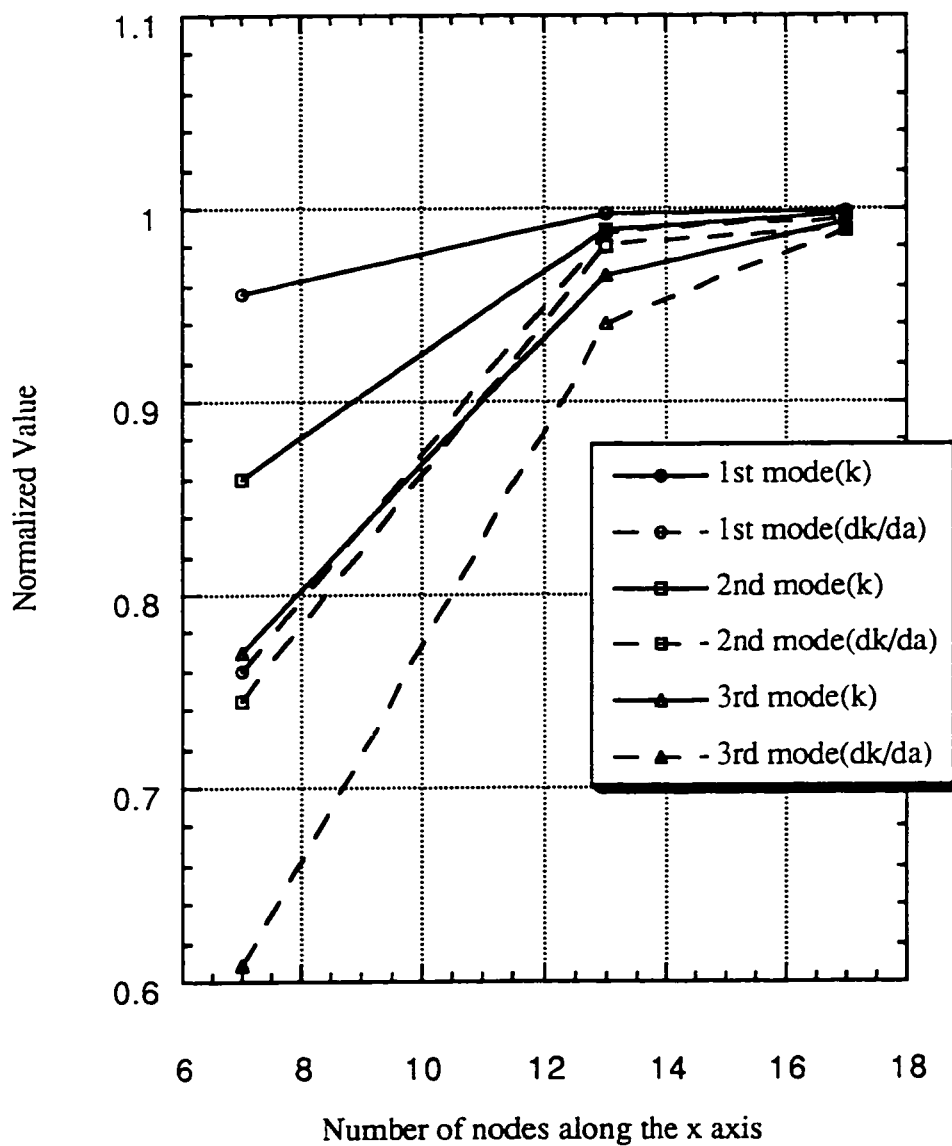


Figure 7.14 Convergence of buckling load and sensitivity for rectangular plate under uniaxial compression ($a/b = 3.2$)

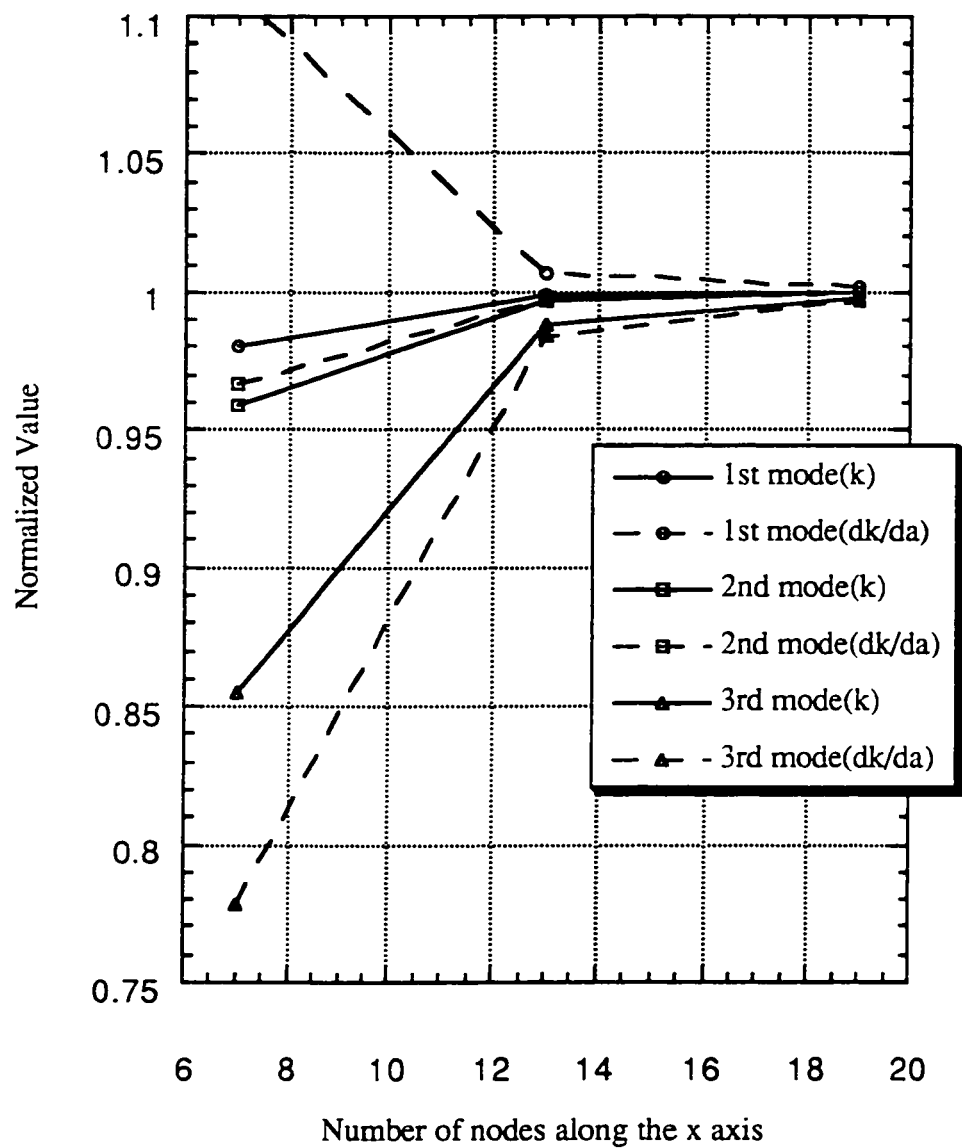


Figure 7.15 Convergence of buckling load and sensitivity for rectangular plate under biaxial compression ($a/b = 3.2$)

7.1.2 Orthotropic Plates

To assess the analytic shape sensitivity of buckling load for the orthotropic plates , GI/Ep single layered square and rectangular plates are examined. The material properties are given as:

$$E_1 = 7.8 \times 10^6 \text{ psi}, E_2 = 2.6 \times 10^6 \text{ psi}, G_{12} = 1.3 \times 10^6 \text{ psi} \text{ and } \nu_{12} = 0.25$$

The theoretical buckling load for the simply supported orthotropic plates subject to uniaxial loads is given in (JON75, WHI87) as

$$n_x = \pi^2 \left(D_{11} \left(\frac{m}{a} \right)^2 + 2(D_{12} + 2D_{66}) \left(\frac{n}{b} \right)^2 + D_{22} \left(\frac{n}{b} \right)^4 \left(\frac{a}{m} \right)^2 \right) \quad (7.9)$$

where m and n are the number of buckling half wavelengths in the x and y directions. These numbers can be different from the ones for isotropic plates because they depend on the material properties as well as the aspect ratio of the plate. The flexural rigidities D_{ij} can be obtained from Eq. (3.47). The theoretical sensitivity is obtained by differentiating Eq. (7.9) with respect to shape design variable , a as

$$\frac{dn_x}{da} = 2\pi^2 \left(-D_{11} \frac{m^2}{a^3} + D_{22} \left(\frac{n}{b} \right)^4 \frac{a}{m^2} \right) \quad (7.10)$$

Two cases are considered. One is a square plate ,i.e. $\frac{a}{b} = 1.0$ and the other is a rectangular plate with $\frac{a}{b} = 3.0$. For both cases, the width b is set to 10 and the thickness to 1.0. Since the symmetric boundary conditions can be applied when the plate is subject to uniaxial compression , only the quarter of the plate in the quadrant III is analyzed, and thus only symmetric modes can be captured in the buckling analysis. Unlike the isotropic plates with same aspect ratios, the first three critical buckling modes are found at $(m = 1, n = 1)$,

$(m = 3, n = 1)$ and $(m = 3, n = 3)$ for the square plate, and at $(m = 3, n = 1)$, $(m = 5, n = 1)$ and $(m = 1, n = 1)$ for the rectangular plate. The same finite element meshes given in Figure 7.2 are used to examine the rate of convergence. The analytic shape sensitivity has been computed when the length of the plate is chosen as the shape design variable. Table 7.7 and 7.8 present the numerical results of a square plate and Figure 7.16 shows the convergence of the buckling loads and sensitivity as the mesh is refined. As shown, the calculated buckling loads and sensitivities converge to the theoretical solutions for all three modes and the sensitivity results showed almost the same convergence rate as the buckling load.

The buckling analysis and sensitivity analysis were repeated for a rectangular plate of aspect ratio 3.0 with the same boundary and loading conditions. Table 7.9 and 7.10 show numerical results of the buckling load and sensitivity, and monotonic convergence behavior for both results can be seen in Figure 7.17. It is interesting to note that the numerical results for the third symmetric mode $(m = 1, n = 1)$ are more accurate than those for the primary $(m = 3, n = 1)$ and second symmetric mode $(m = 5, n = 1)$, in contrast to the previous cases. For example, the 3×1 mesh configuration yields the buckling load within 2.2 percent for the third symmetric mode, while the results for the primary and secondary one show errors of 3.9 and 19.7 percents, respectively. Similar trends are observed for the sensitivity results.

Table 7.7 Buckling load for the orthotropic square plate.

	1st sym. mode ($m = 1, n = 1$)	2nd sym. mode ($m = 3, n = 1$)	3rd sym. mode ($m = 3, n = 3$)
1 × 1 MESH	137955.	280175.	
2 × 2 MESH	140706.	570594.	1032012.
3 × 3 MESH	140960.	646226.	1213038.
4 × 4 MESH	140974.	659197.	1249977.
Exact	141044.	665183.	1269399.

Table 7.8 Buckling load sensitivity for the orthotropic square plate.

	1st sym. mode ($m = 1, n = 1$)	2nd sym. mode ($m = 3, n = 1$)	3rd sym. mode ($m = 3, n = 3$)
1 × 1 MESH	-8475.33	-24983.96	
2 × 2 MESH	-8692.84	-97426.08	-62590.06
3 × 3 MESH	-8725.17	-107771.7	-71002.49
4 × 4 MESH	-8731.29	-111769.1	-75884.84
Exact	-8735.65	-113563.4	-78620.85

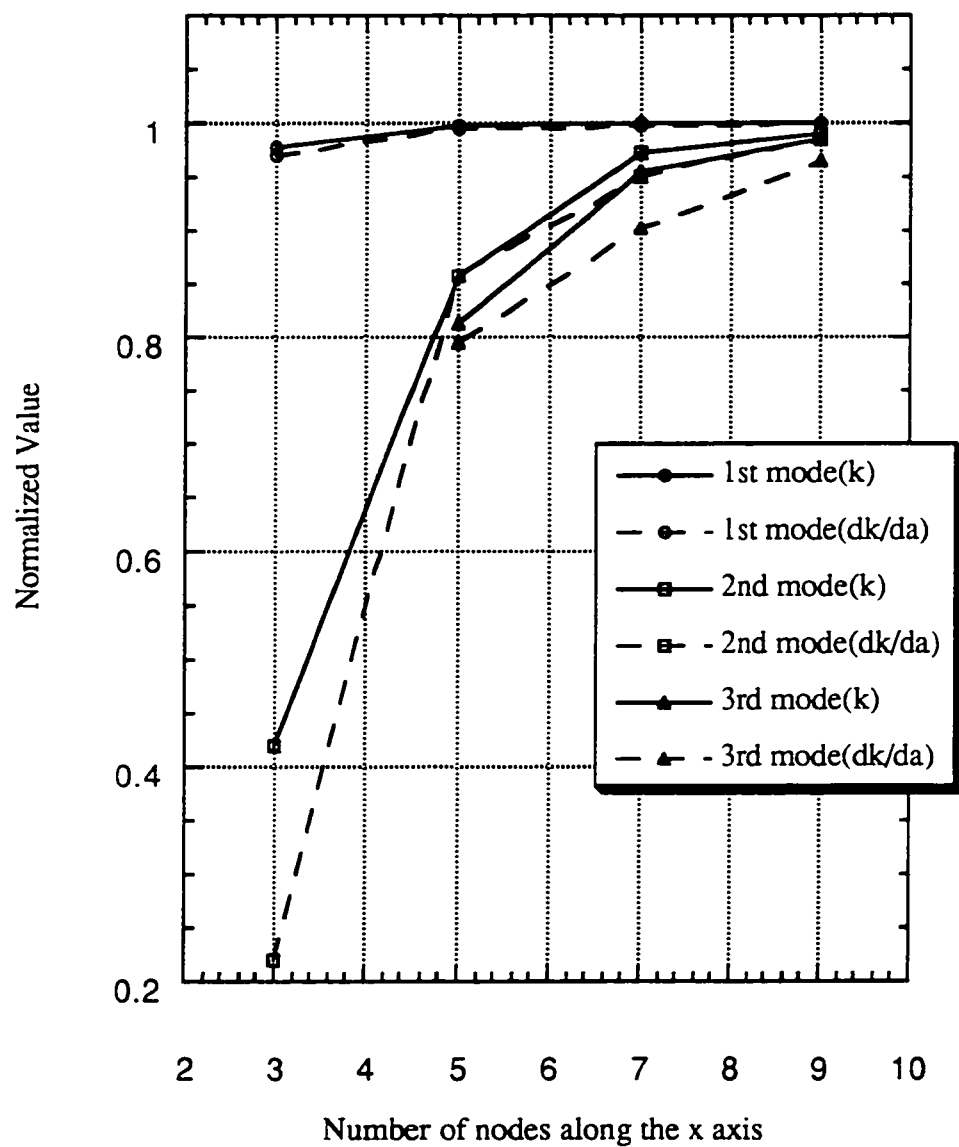


Figure 7.16 Convergence of buckling load and sensitivity for the orthotropic square plate.

Table 7.9 Buckling load for the orthotropic rectangular plate ($a/b = 3.0$).

	1st sym. mode ($m = 3, n = 1$)	2nd sym. mode ($m = 5, n = 1$)	3rd sym. mode ($m = 1, n = 1$)
3 × 1 MESH	135572.	195540.	251854.
6 × 2 MESH	140621.	239889.	257056.
9 × 3 MESH	140946.	242788.	257442.
Exact	141044.	243542.	257520.

Table 7.10 Buckling load sensitivity for the orthotropic rectangular plate ($a/b = 3.0$).

	1st mode ($m = 3, n = 1$)	2nd mode ($m = 5, n = 1$)	3rd mode ($m = 1, n = 1$)
3 × 1 MESH	-2677.77	-7164.89	11962.0
6 × 2 MESH	-2891.21	-11269.7	12592.9
9 × 3 MESH	-2907.22	-11539.1	12613.1
Exact	-2911.88	-11608.7	12618.2

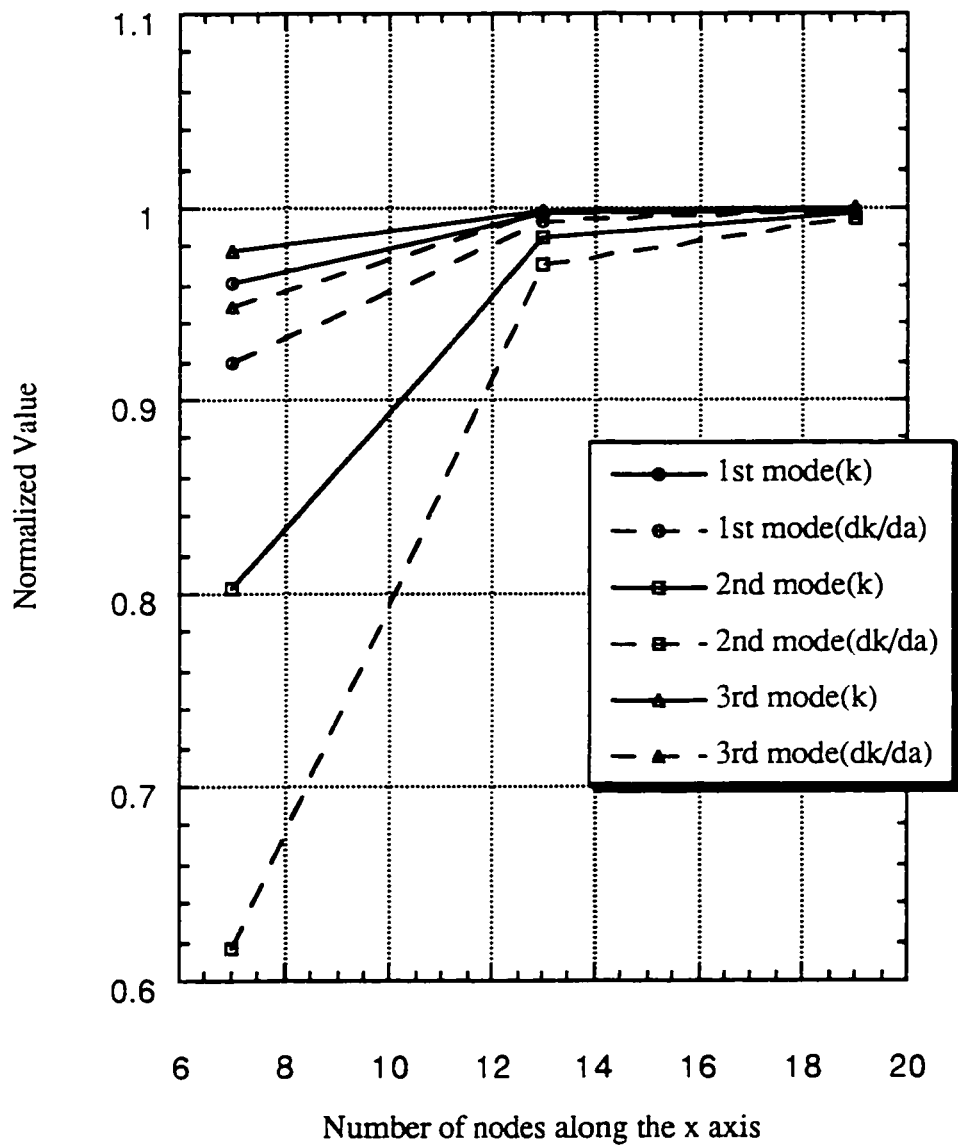


Figure 7.17 Convergence of buckling load and sensitivity for the orthotropic rectangular plate ($a/b = 3.0$).

7.1.3 Anisotropic Laminated Plates

In this section, numerical results are presented for the anisotropic laminated plates with various aspect ratios. Symmetric angle ply laminates made of 20 piles of DLP material are examined, the material properties of single ply is given in Table 7.11. The boundary conditions considered have all edge simply supported. Two load cases are considered, biaxial compression and uniaxial compression. Since the material properties depend on the fiber orientation, the full geometry of the plates is analyzed using a 10×10 finite element mesh. This proved to be sufficient for the required convergence in the finite element analysis. In the sensitivity analysis, the length a of the plate was chosen as the shape design variable. To assess the capability on the plate made of anisotropic material, the buckling loads for simply supported anisotropic laminated plates with various stack angles were obtained and are presented in Table 7.12 with the theoretical solutions (CHA69), which are solved by applying Galerkin method with trigonometric approximation of the lateral displacement. The plate is square with $b = 10$ inches and it is subject to uniaxial compression in this example. In all cases, the buckling mode shape has one half-wave in each direction ($m = 1$, $n = 1$). It is observed that the buckling loads from the present finite element analysis correlate very well with the theoretical results.

Numerical results for the buckling and sensitivity analysis for the anisotropic rectangular plates under uniaxial compression and biaxial compression are shown in Table 7.13 and 7.14 and analytic sensitivity results are shown in parenthesis. The plates have ply stacking sequence of $(30/-30)_5$, and the length of the plate, a has been changed from 5 to 20 with $b = 10$. The comparisons of the buckling loads with existing theoretical solutions are made when they are available. Since there are no continuous solutions for the buckling loads in this example, the numerical accuracy of the sensitivity result can not be obtained.

However, good correlation with the buckling results can be seen in the Figure 7.18 and 7.19. Again the sensitivities of the buckling loads with respect to the shape design variable are illustrated as a slope of the buckling load at each design variable. It is observed in these figures that larger values of sensitivity are obtained when the buckling loads change rapidly and the sensitivity decreases with small change of buckling loads.

Table 7.11 Material properties of DLP single layer.

E_1 ($\times 10^6$ psi)	E_2 ($\times 10^6$ psi)	G_{12} ($\times 10^6$ psi)	ν_{12}	t_l (inches)
32.9	1.8	0.88	0.24	0.0048

Table 7.12 Comparison of Buckling Loads for Anisotropic Composite Plates

Stack Angle	Series Solution (CHA69)	Present Analysis
20(0)	286	285.14
(15/-15) _{ss}	340	339.16
(30/-30) _{ss}	450	447.75
(45/-45) _{ss}	505	502.16
(60/-60) _{ss}	428	425.64
(75/-75) _{ss}	226	224.40
(90/-90) _{ss}	145	144.43

Table 7.13 Buckling Loads and Sensitivities for Anisotropic Composite Plates Under Uniaxial compression $((30/-30)_{5,s})$

Design Variable a	Series Solution	Present Analysis
5.0	854	851.03 (-223.8)
7.5		545.29 (-62.80)
10.0	450	447.75 (-22.58)
12.5		412.87 (-7.36)
15.0		404.77 (0.14)
17.5		411.16 (4.65)
20.0	429	426.94 (7.81)

Table 7.14 Buckling Loads and Sensitivities for Anisotropic Composite Plates Under Biaxial Compression $((30/-30)_{5,s})$

Design Variable a	Series Solution	Present Analysis
5.0	683	680.78 (-233.5)
7.5		348.96 (-78.69)
10.0	225	223.87 (-33.67)
12.5		161.12 (-18.59)
15.0		124.55 (-11.45)
17.5		101.22 (-7.57)
20.0	86	85.40 (-5.26)

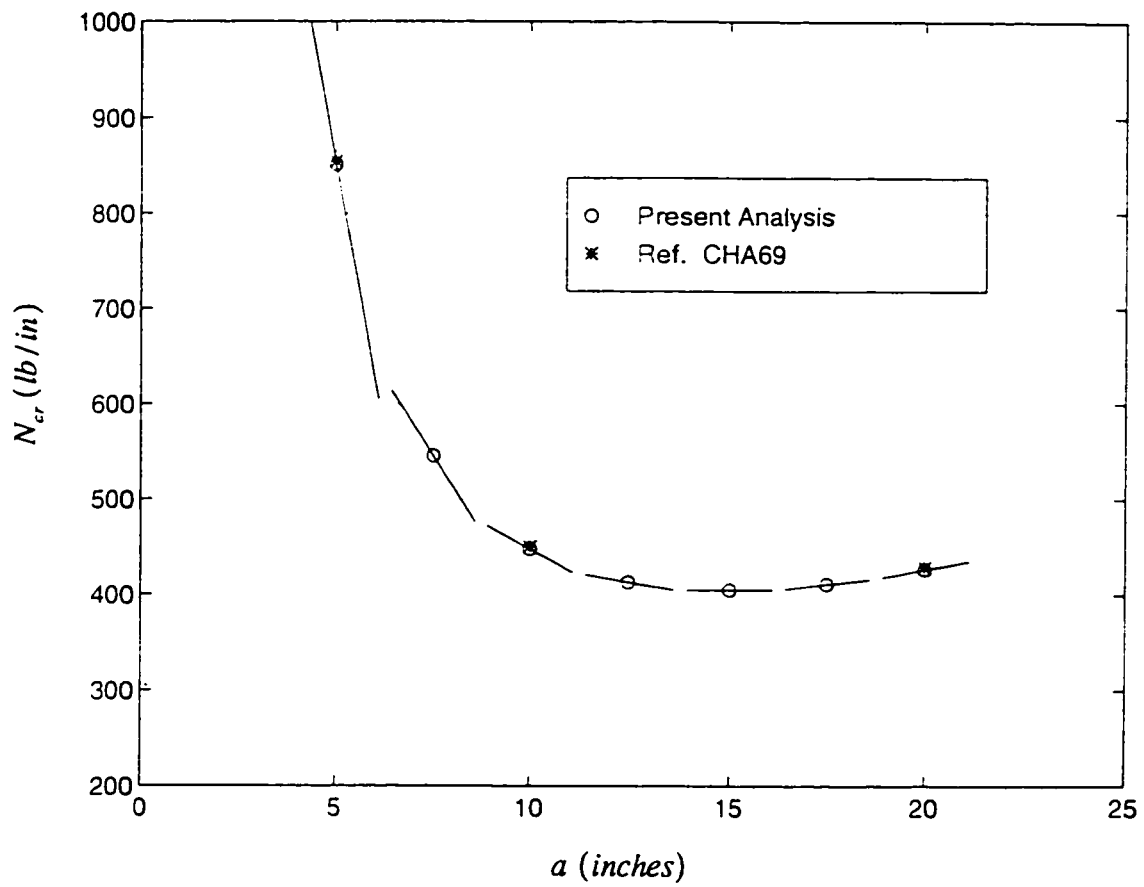


Figure 7.18 Buckling load coefficient and sensitivity for the anisotropic rectangular plate under uniaxial force

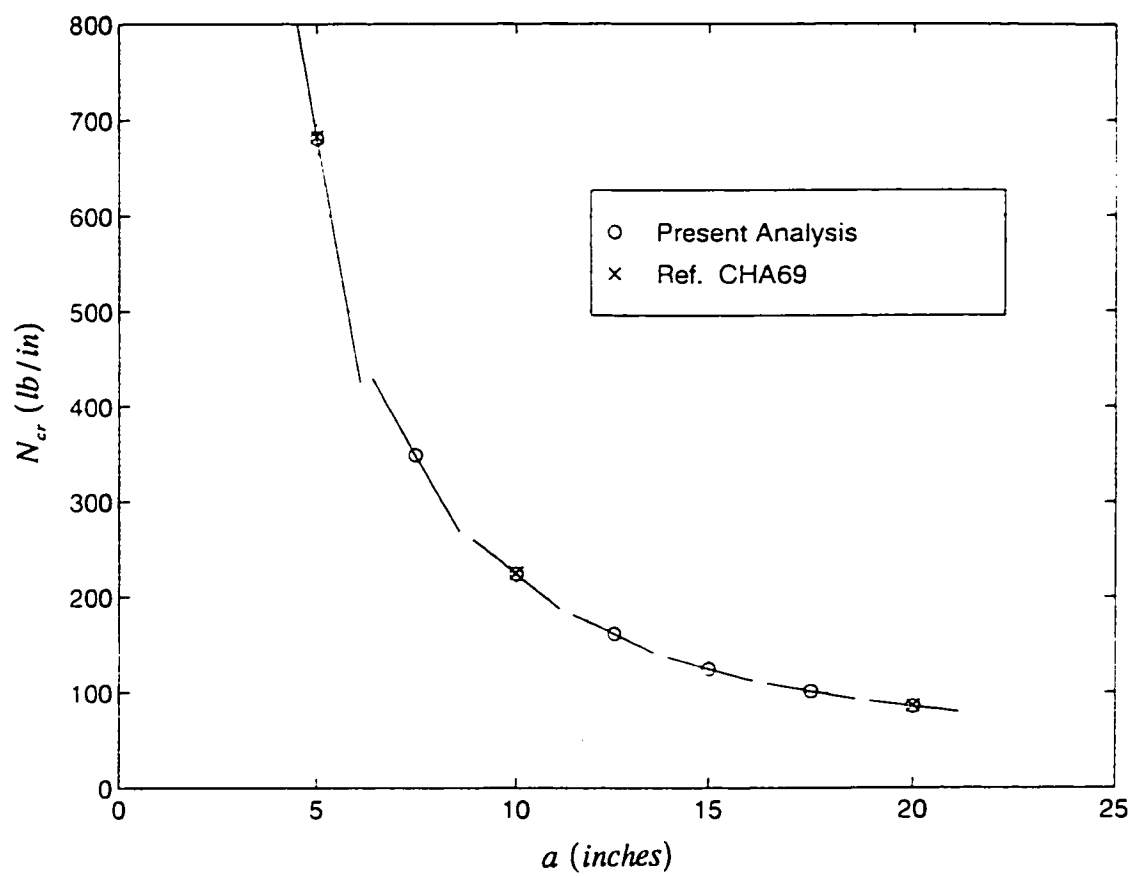


Figure 7.19 Buckling load coefficient and sensitivity for the anisotropic rectangular plate under biaxial force

7.2 Equilateral Triangular Plates under Uniform Compression

An equilateral triangular plate subjected to a uniform compression is illustrated in Fig 7.20. The plate has altitude a , and a constant thickness t . It is assumed to be simply supported on its edges and subject to uniform compressive force per unit length, N . In the sensitivity analysis, the altitude a of the plate is chosen as the shape design variable.

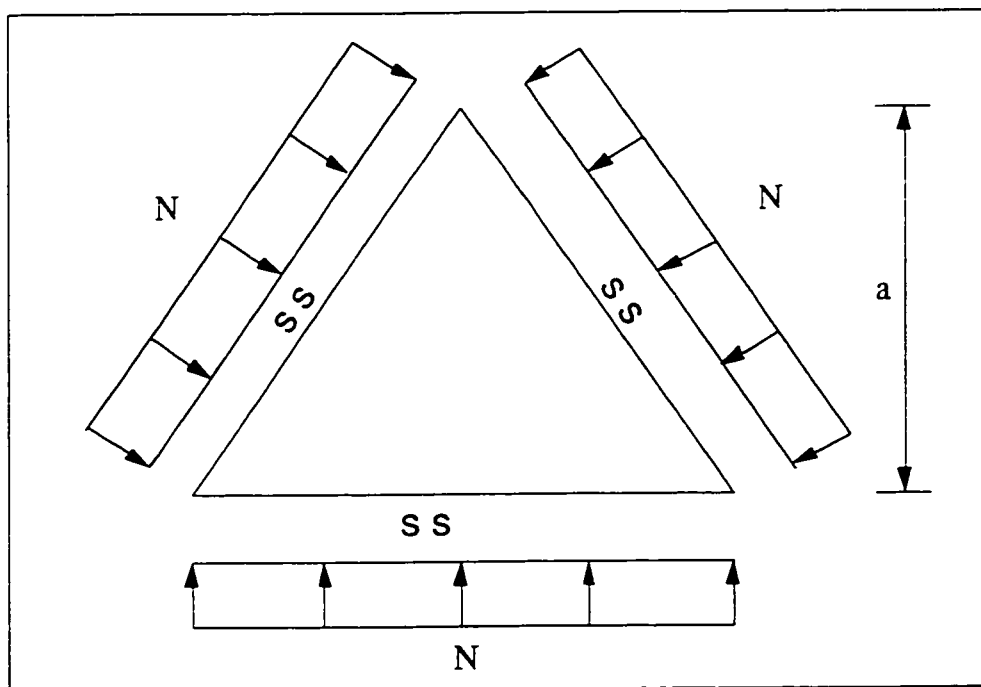


Figure 7.20 Simply Supported Triangular Plate subject to Uniform Compression

Theoretical solution is available for the critical buckling in (TG61) as

$$N_{cr} = k\pi^2 D \quad (7.11)$$

where

$$k = \frac{4}{a^2} \quad (7.12)$$

The theoretical sensitivity can be obtained as

$$\frac{dN_{cr}}{da} = \frac{dk}{da} \pi^2 D \quad (7.13)$$

where

$$\frac{dk}{da} = -\frac{8}{a^3} \quad (7.14)$$

The same material properties for the isotropic rectangular plate are used for the finite element calculation of the buckling load and its sensitivity. Figure 7.21 shows four finite element mesh configurations with different mesh densities, in terms of the number of elements along one edge. As the shape of the plate is equilateral triangle, all the elements have the same shape as the plate itself. Numerical results for both the buckling load and sensitivity are compared with theoretical solution in Table 7.15 when a is 1. The normalized results are shown in Figure 7.22. The results from the finite element buckling and sensitivity analysis showed good convergence behavior. It is interesting to note that the accuracy of buckling coefficient sensitivity is identical to the accuracy of the buckling coefficients for a given finite element mesh. Figure 7.23 shows the calculated buckling load coefficient and graphical representation of sensitivity result when mesh density is 4 and the corresponding mode shape can be seen in Figure 7.24.

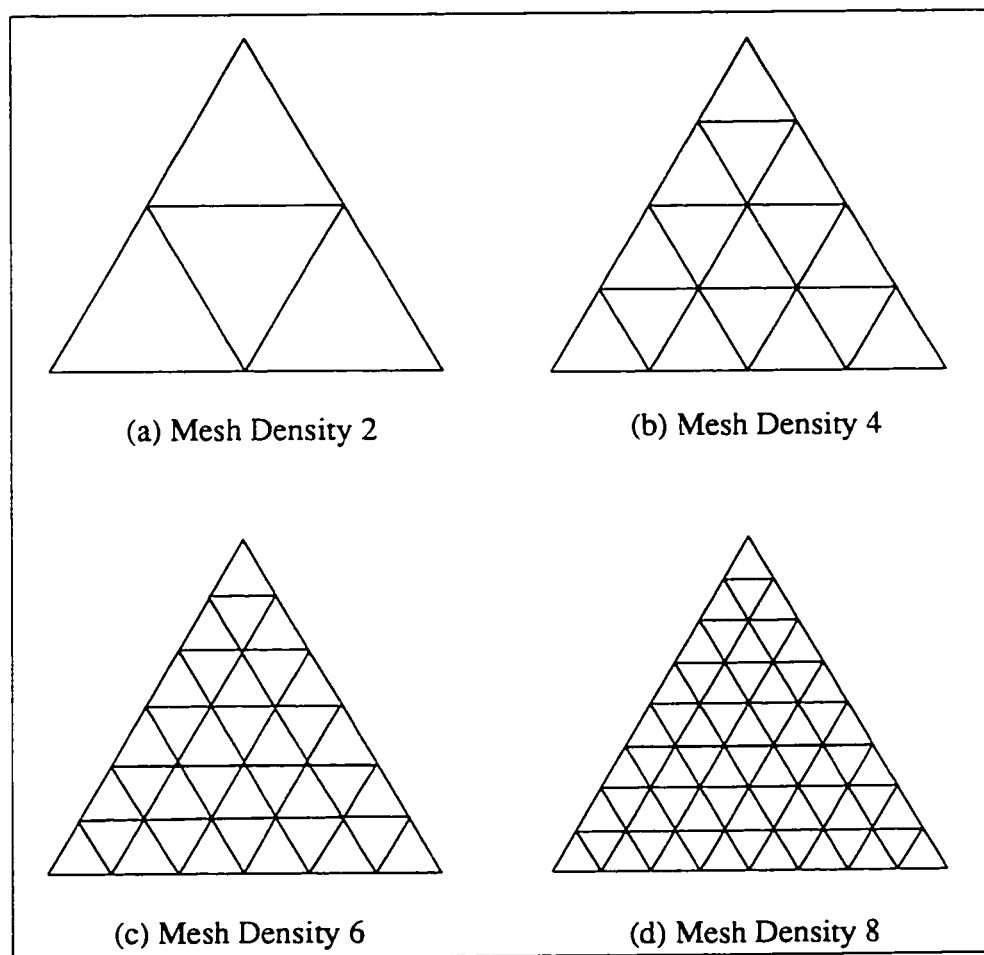


Figure 7.21 Finite Element mesh configuration for equilateral triangular plate.

Table 7.15 Critical buckling load and sensitivity for the equilateral triangular plate ($a = 1.$)

Mesh Density (Total D.O.F.)	Buckling load coeff. k	Sensitivity $\frac{dk}{da}$
2 (48)	0.7254	-5.803
4 (168)	0.9874	-7.899
6 (360)	0.9975	-7.980
8 (675)	0.9992	-7.994
Exact	1.0000	-8.000

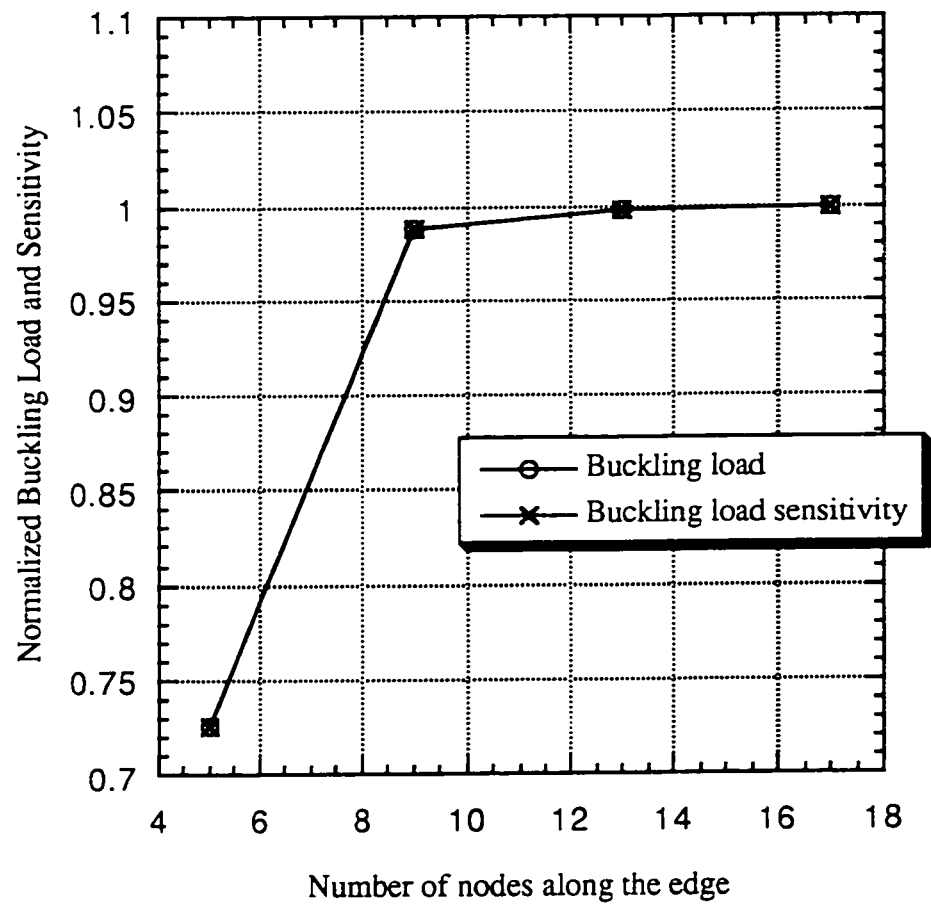


Figure 7.22 Convergence of buckling load and sensitivity for triangular plate ($a = 1.$)

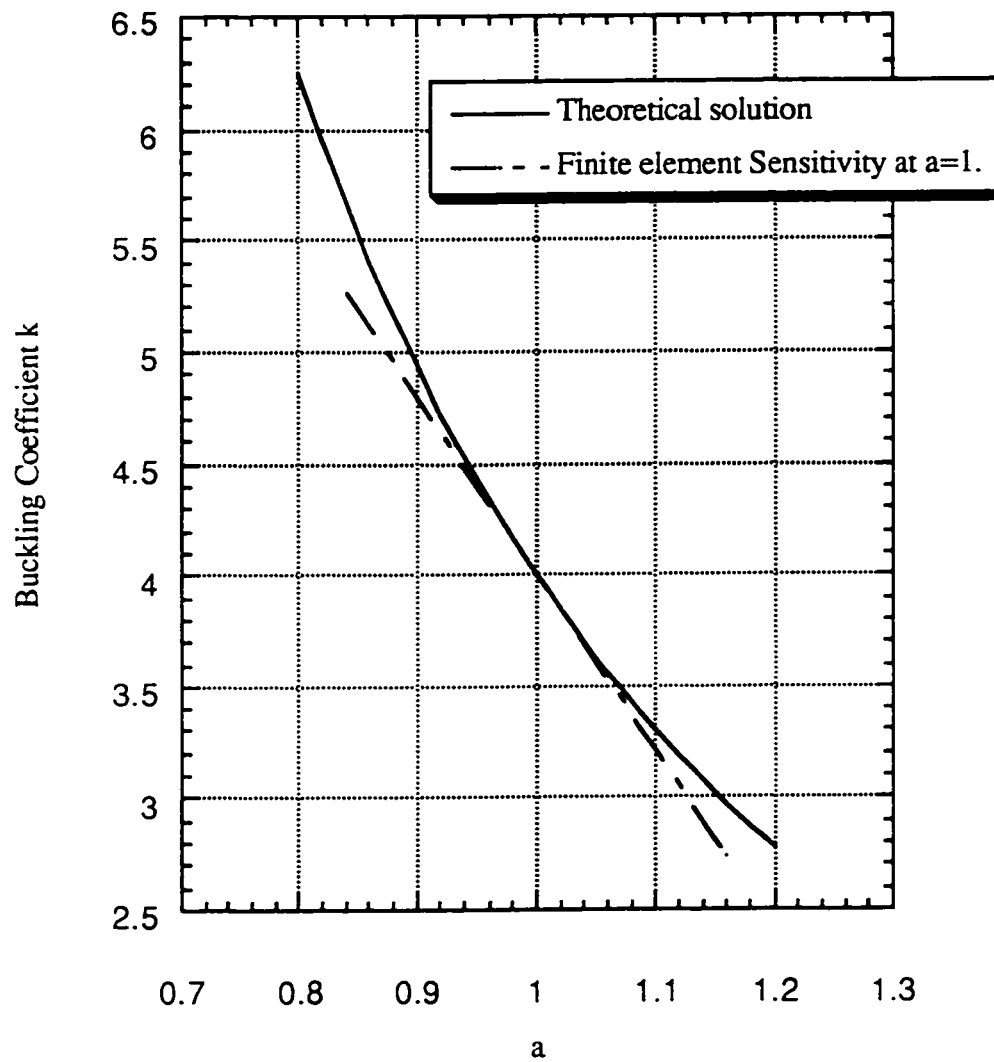
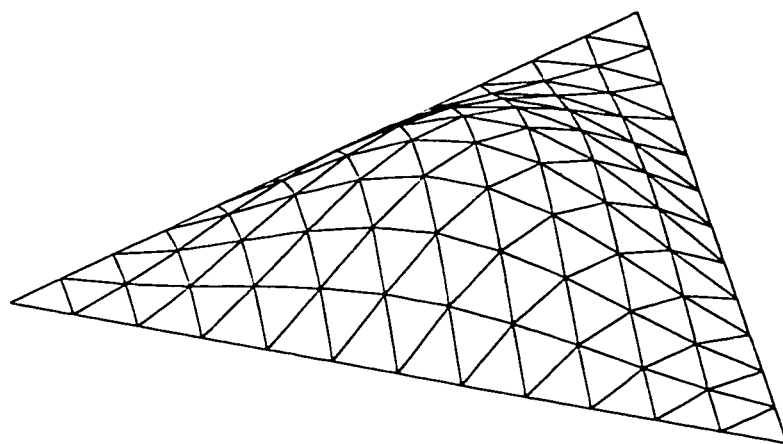


Figure 7.23 The sensitivity of buckling load for the equilateral triangular plate.



7.24 Mode shape for the critical mode of an equilateral triangular plate.

7.3 Skew Plates with Uniaxial Compression

With an increasing use of skew or oblique plates in the construction of airplane structures, the buckling of skew plates is of interest to the designer. A rich body of literature on the buckling of skewed plates exist (WLA92, MKN80, JKA95, KRP95, KXWL93). In this section, numerical results are presented for the buckling sensitivity analysis of isotropic, orthotropic and anisotropic plates with the skewed geometries illustrated in Figure 7.25.

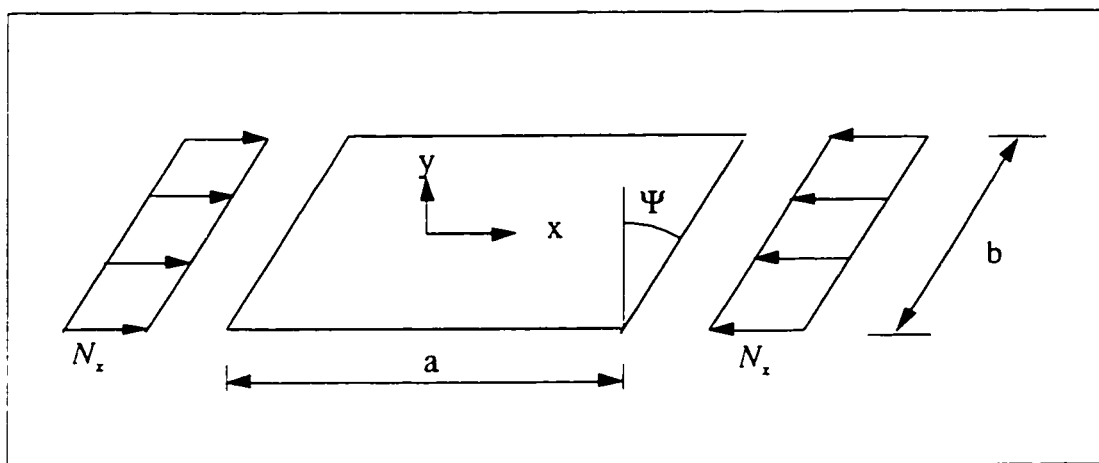


Figure 7.25 Skew plate subject to uniaxial compression

The plate is assumed to be either simply supported or clamped on its edges and subject to uniaxial compressive force per unit length N_x in the x direction. Since the geometry of the plate is not symmetric, the full plate is analyzed and a 10×10 mesh density illustrated in Figure 7.27 is used after the convergence study. In the sensitivity analysis, the skew angle of the plate Ψ is chosen as a shape design variable. The finite element

approximations of the buckling load and its sensitivity are obtained not only for the first mode but also for the second mode.

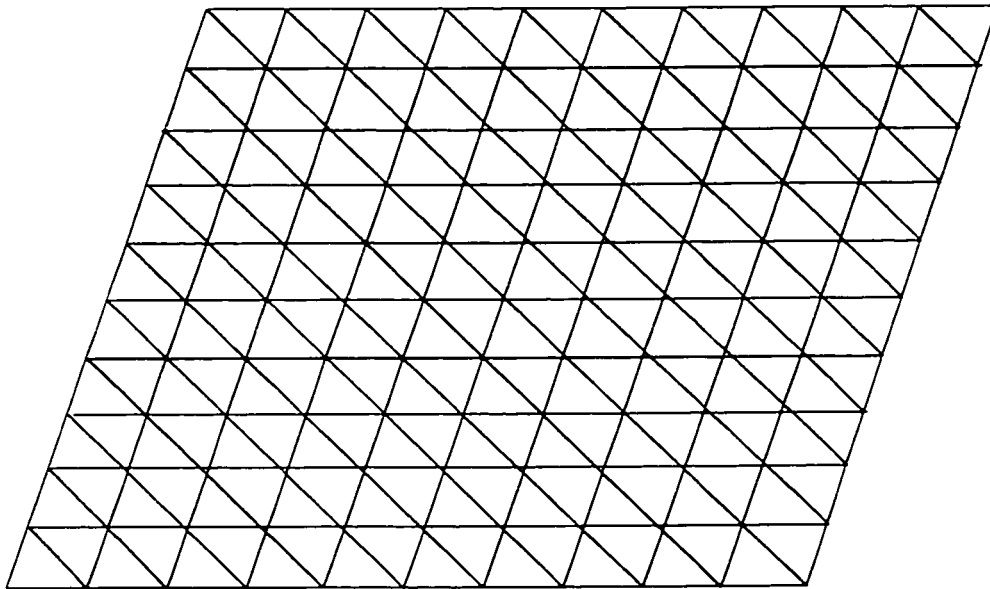


Figure 7.26 Finite element mesh configuration for skew plate.

7.3.1 Isotropic Skew Plates

Although there are theoretical solutions for the buckling load of rectangular plates under certain boundary and loading conditions, there are none for skewed plates. Therefore the buckling of clamped and simply supported isotropic skewed plate has been studied by many researchers using various numerical methods. The Rayleigh-Ritz method has been used with one of trigonometric functions in oblique coordinates (WIT53, KP78), a combination of B-splines and trigonometric functions (MKN80) or the modified Ritz functions (WLA92, KXWL93). Recently the finite element method has been used for the

buckling analysis of laminated skew plates (KRP95) and Jaunky and Knight (JK95) applied the Rayleigh-Ritz method combined with a first-order transverse shear deformation theory using higher order polynomial Ritz function. In that paper, they presented the buckling results obtained by the finite element code STAG in which C^1 4-node elements are used. Results from the present finite element method for clamped and simply supported skew plates with side ratio $a/b = 1$ are presented and compared with existing results in Table 7.16 and 7.17, respectively.

The geometry of the skew plate is assumed as $a = 10.0$, $b = 10.0$, $t = 0.1$. The material properties of isotropic material are given as $E = 1.0 \times 10^7$ and $\nu = 0.3$ Buckling loads are nondimensionalized and presented as a buckling load coefficient defined as

$$k = \frac{N_x b^2}{\pi^2 D} \quad (7.15)$$

Results shown in Table 7.16 for clamped plates show that all solutions are in good agreement. All the results are within 0.3 - 11 percents from each other for all skew angles. The results from present finite element analysis are lower than those of other results when skew angles are 30 and 45 degrees. However, even when the skew angle is 45 degree, the difference from the largest solution is less than 11 percents. Table 7.17 shows that there is a relatively large variation of results for the simply supported case when the skew angles are larger than 15 degree. It is interesting to note that the present analysis results closest to the solutions from STAG, another finite element analysis.

Table 7.16 Buckling Load coefficient k for clamped isotropic plates, $a/b = 1$

	$\Psi = 0$	$\Psi = 15$	$\Psi = 30$	$\Psi = 45$
Wittrick	10.08		13.64	21.64
Wang et al	10.08	10.76	13.75	20.69
Kitipornchai	10.07	10.83	13.54	20.11
Krishina Reddy	10.08	10.76	13.64	20.69
Jaunky et al (F.E.M.)	10.08	10.82	13.47	19.92
Jaunky et al (Rayleigh-Ritz)	10.07	10.83	13.55	20.20
Present F.E.M.	10.06	10.81	13.39	19.25

Table 7.17 Buckling Load coefficient k for simply supported isotropic plates, $a/b = 1$

	$\Psi = 0$	$\Psi = 15$	$\Psi = 30$	$\Psi = 45$
Kennedy et al	4.00	4.33	5.53	8.47
Mizusawa et al	4.00	4.34	5.61	8.64
Wang et al	4.00	4.39	5.98	9.87
Kitipornchai	4.00	4.39	5.90	10.10
Krishina Reddy	4.00	4.32	5.55	8.64
Jaunky et al (F.E.M.)	4.00	4.39	5.85	9.70
Jaunky et al (Rayleigh-Ritz)	4.00	4.40	6.01	10.52
Present F.E.M.	4.00	4.38	5.73	9.17

In order to see the results of the sensitivity analysis, the skew angle of the plate with $a/b = 1$ has been changed from 0 to 60 degrees and numerical results for the first and second buckling modes can be seen in Table 7.18. In Figure 7.27, the calculated sensitivities are illustrated as the slope of buckling load coefficients k . It is observed that a mode switch is expected when the skew angles are larger than 50 degree because the sensitivity of the first mode is less than that of second mode, and the buckling load coefficients for two modes are relatively close at $\Psi = 50$. Also, the trends of sensitivities for the two modes at $\Psi = 55$ are consistent to this proposition. In Figure 7.30 and 7.31, buckling mode shapes for the first mode (Mode A) and the second mode (Mode B) are shown for the skew angle of 30 degree. Modes A and B have been the first and the second modes up to $\Psi = 50$ but as it is increased to 55 degree, the mode switch is observed, as it was expected in Figure 7.28. Then Mode B becomes the first mode and the second mode shape is similar to Mode A when the skew angle is larger than some value between 50 and 55 degrees, as illustrated in Figure 7.28. When the sensitivity of buckling load is obtained by finite difference scheme, it would be hard to detect the mode switch in case where a relatively large amount for the design variable variation was being considered near the critical value of design variable.

Table 7.18 Buckling Coefficient and Sensitivity for simply supported isotropic skewed plates, $a/b = 1$

skew angle (degree) Ψ	Primary Mode		Second Mode	
	k	$\frac{\partial k}{\partial \Psi}$	k	$\frac{\partial k}{\partial \Psi}$
0	4.000	0.000015	6.246	0.00012
5	4.041	0.01658	6.296	0.01993
10	4.167	0.03390	6.446	0.03979
15	4.383	0.05288	6.694	0.05985
20	4.700	0.07478	7.045	0.08048
25	5.138	0.1015	7.501	0.1024
30	5.728	0.1364	8.072	0.1268
35	6.524	0.1849	8.776	0.1560
40	7.617	0.2578	9.646	0.1943
45	9.176	0.3757	10.748	0.2503
50	11.517	0.5797	12.208	0.3425
55	14.303	0.5150	15.224	0.9314
60	17.667	0.8812	20.749	1.1802

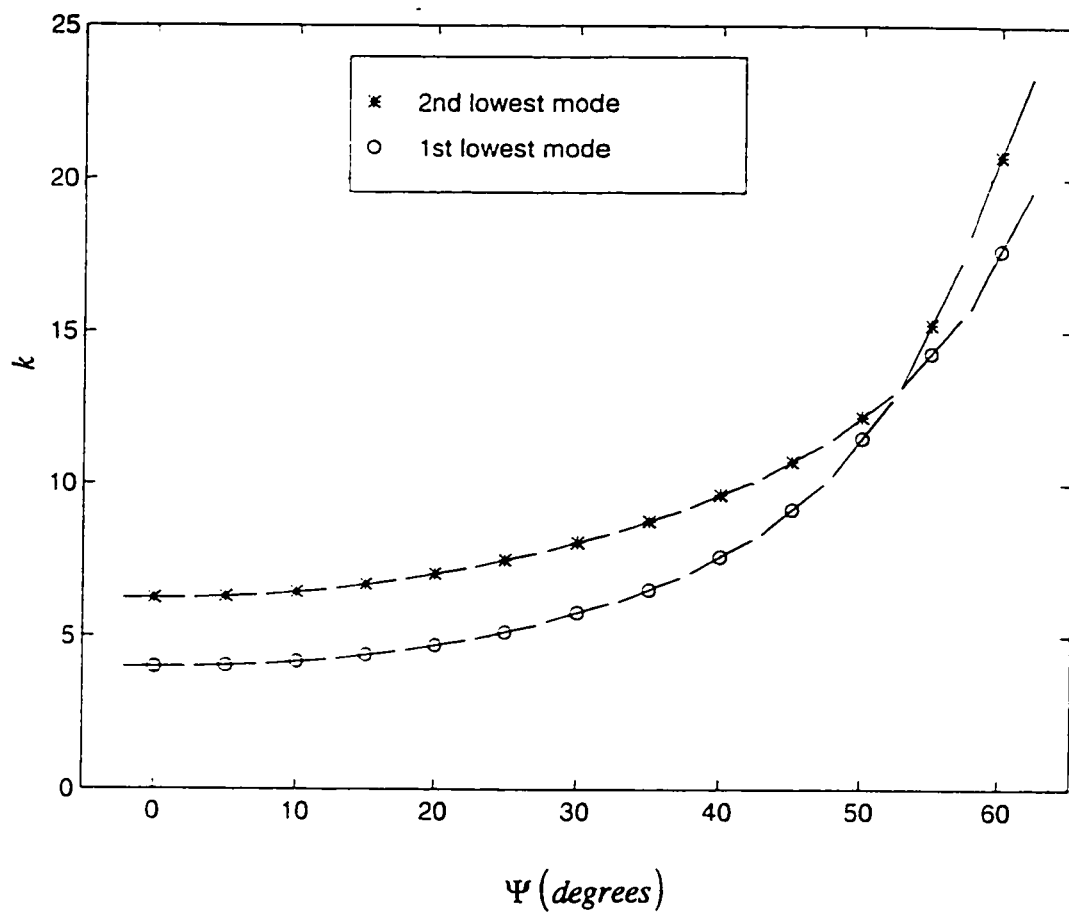


Figure 7.27 Buckling load coefficient and sensitivity for the isotropic skew plate

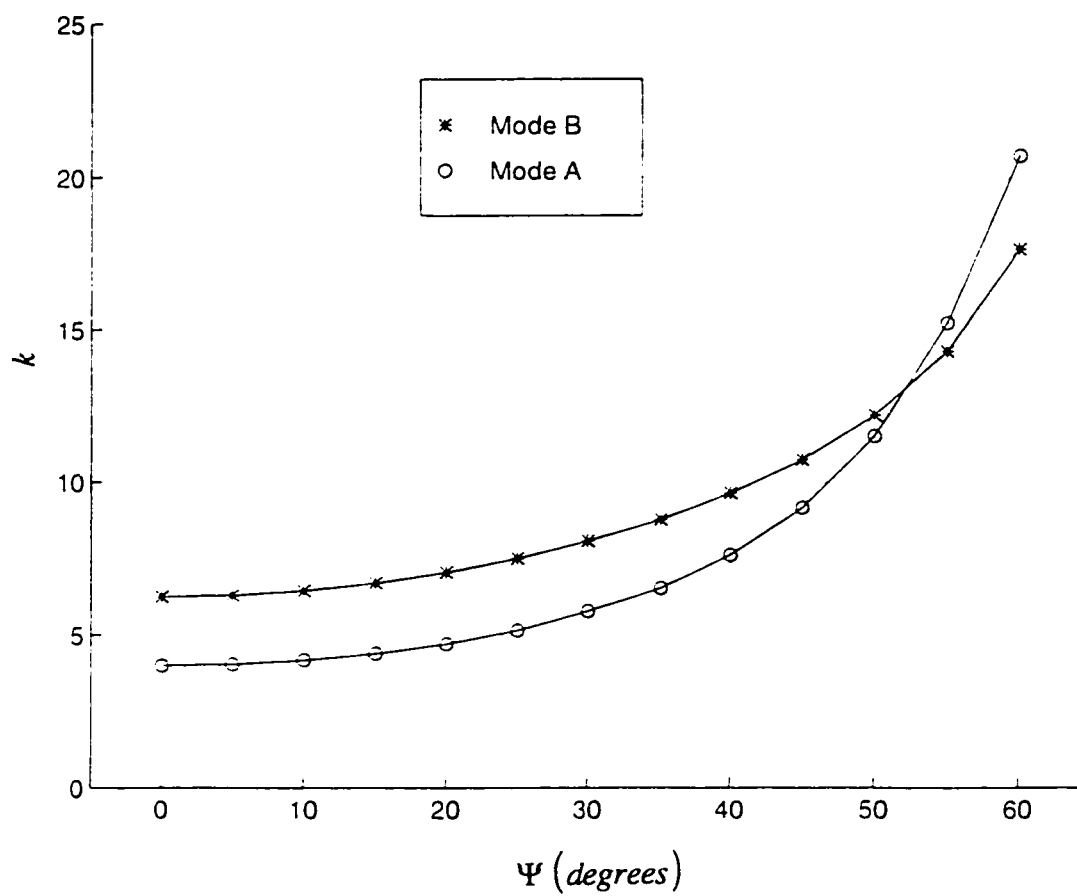


Figure 7.28 Buckling load coefficient and buckling mode for the isotropic skew plate

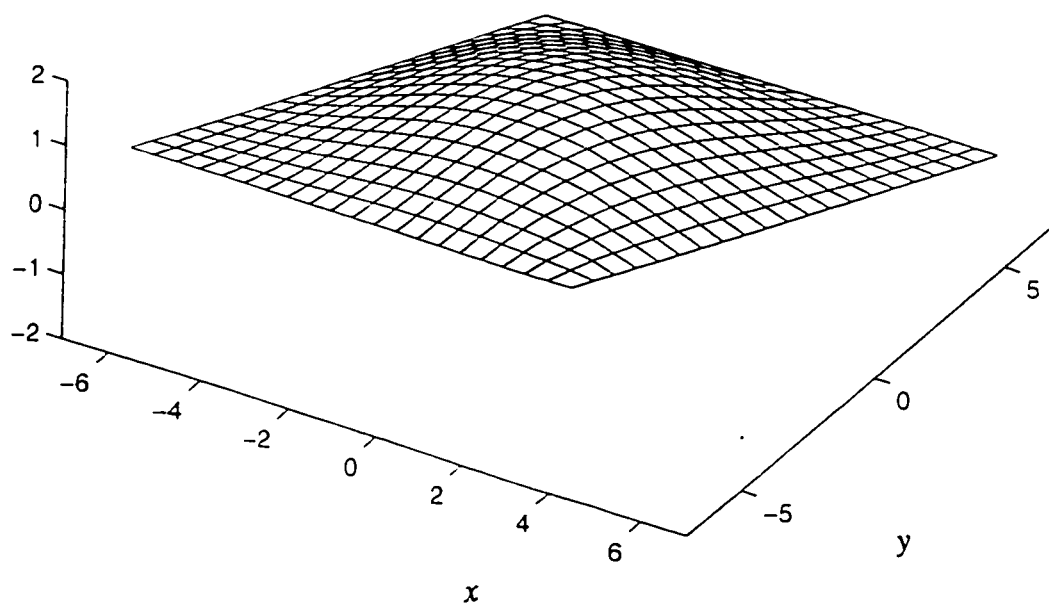


Figure 7.29 Mode shape (Mode A) for the critical mode of the isotropic skew plate ($\Psi = 30$).

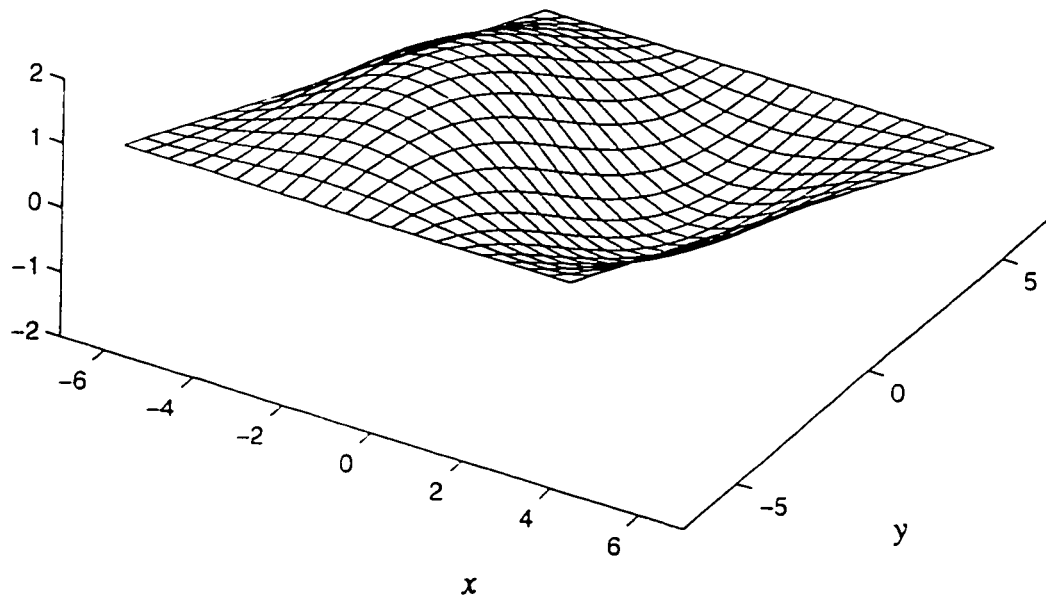


Figure 7.30 Mode shape (Mode B) for the second mode of the isotropic skew plate ($\Psi = 30$).

7.3.2 Orthotropic and Anisotropic Laminated Skew Plates

Numerical results are obtained for the buckling and sensitivity analysis of orthotropic and laminated skew plates. The skew plates are assumed to be simply supported on its edges and subject to uniaxial compression as illustrated in Figure 7.25. The skew plate has a side ratio $a/b = 1$ with $b = 10$. Material properties for the orthotropic plate case are assumed as $D_{11}/D_{22} = 10$, $D_{33}/D_{22} = 0.5$, and $\nu_{12} = 0.25$, with $E_2 = 2.6 \times 10^6$, and a thickness ratio $t/b = 0.01$. For the laminated skew plates, results are obtained for DLP laminate and its material properties can be seen in Table 7.11. Three types of laminated skew plates are considered with fiber orientations of $(+30/-30)_{s_s}$, $(+45/-45)_{s_s}$, and $(+60/-60)_{s_s}$. The critical buckling loads for the orthotropic skew plates are nondimensionalized as

$$k = \frac{N_x b^2}{\pi^2 D_{22}} \quad (7.16)$$

In the sensitivity analysis, the skew angle is chosen as the shape design variable in both cases. The primary mode shapes are same for all skew angles considered and are identical to the mode shape shown in Figure 7.29 for both cases. There is no mode switch. Table 7.19 shows the numerical results for the orthotropic plates with various skew angles and comparisons are made with Fourier series solutions obtained from the Rayleigh-Ritz method (KP78) when they are available. It may be seen that close agreement exists between the two solutions when skew angles are 15 and 30 degree. In Figure 7.31, the analytic sensitivities are depicted as the slopes of buckling loads and they match the calculated buckling loads very well. The variation of buckling loads can be seen in Table 7.20 for the simply supported laminated skew plates and the sensitivity results are depicted in Figure

7.32. Once again, the results of the present analytic sensitivity analysis agree very well with the buckling loads obtained.

Table 7.19 Buckling Coefficient and Sensitivity for simply supported orthotropic skewed plates ($a/b = 1$)

skew angle Ψ (degree)	Series Solution k (KP78)	Present result k	Present result $\frac{\partial k}{\partial \Psi}$
0		13.497	.0000619
5		13.575	.0313
10		13.812	.0637
15	14.38	14.217	.0989
20		14.808	.138
25		15.614	.185
30	17.24	16.680	.244
35		18.083	.322
40		19.948	.432
45	25.27	22.498	.601
50		26.153	.887
55		31.779	1.425
60		41.383	2.579

Table 7.20 Buckling loads and sensitivity for simply supported laminated skewed plates
($a/b = 1$)

Skew Angle Ψ	$(+30/-30)_{s,s}$		$(+45/-45)_{s,s}$		$(+60/-60)_{s,s}$	
	N_x	$\frac{\partial N_x}{\partial \Psi}$	N_x	$\frac{\partial N_x}{\partial \Psi}$	N_x	$\frac{\partial N_x}{\partial \Psi}$
0	447.75	-0.21	502.15	-0.13	425.63	-0.31
5	449.35	0.85	503.68	0.76	426.19	0.56
10	456.33	1.96	510.00	1.96	431.79	1.75
15	469.17	3.21	522.46	3.24	444.45	3.39
20	488.76	4.68	543.29	5.19	466.34	5.43
25	516.53	6.51	575.55	7.85	499.25	7.80
30	554.72	8.89	623.42	11.50	544.92	10.56
35	606.88	12.17	693.09	16.70	605.94	14.00
40	678.92	16.98	794.66	24.51	687.00	18.72
45	781.21	24.55	946.01	37.11	797.31	25.98

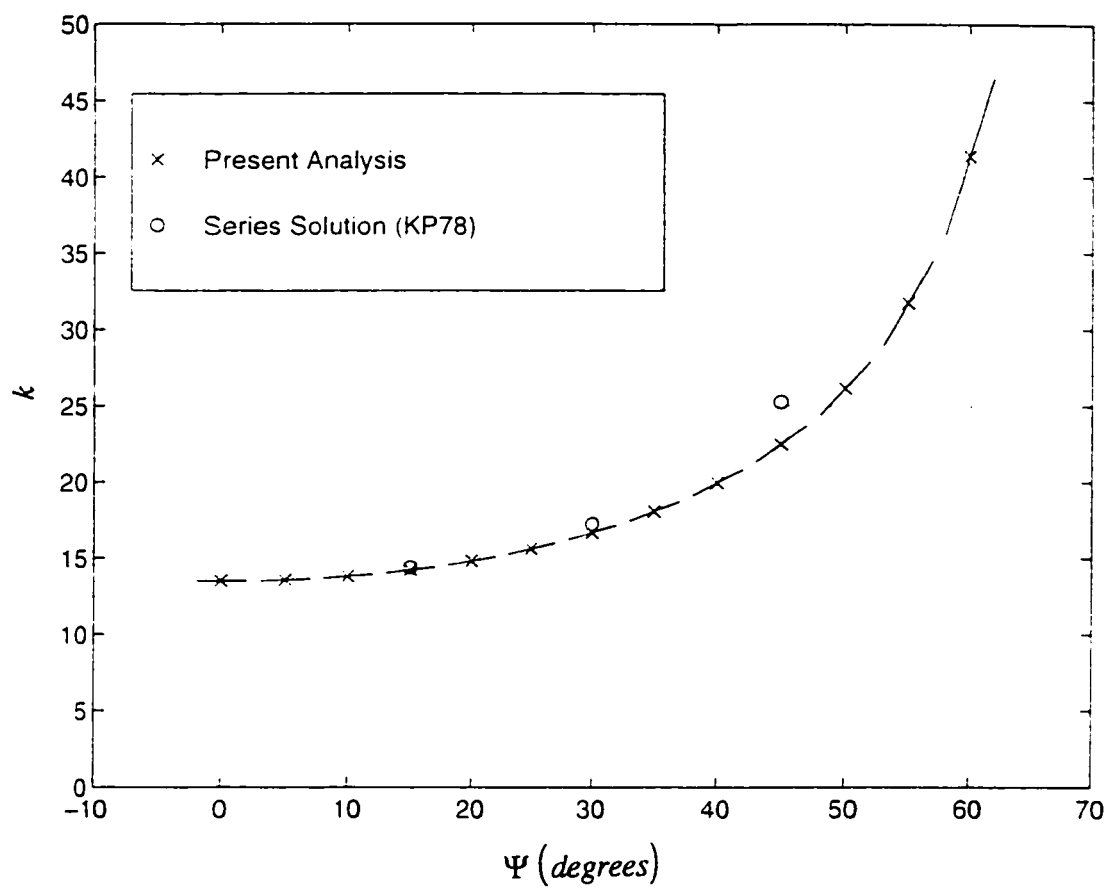


Figure 7.31 Buckling load coefficient and sensitivity for the orthotropic skew plate

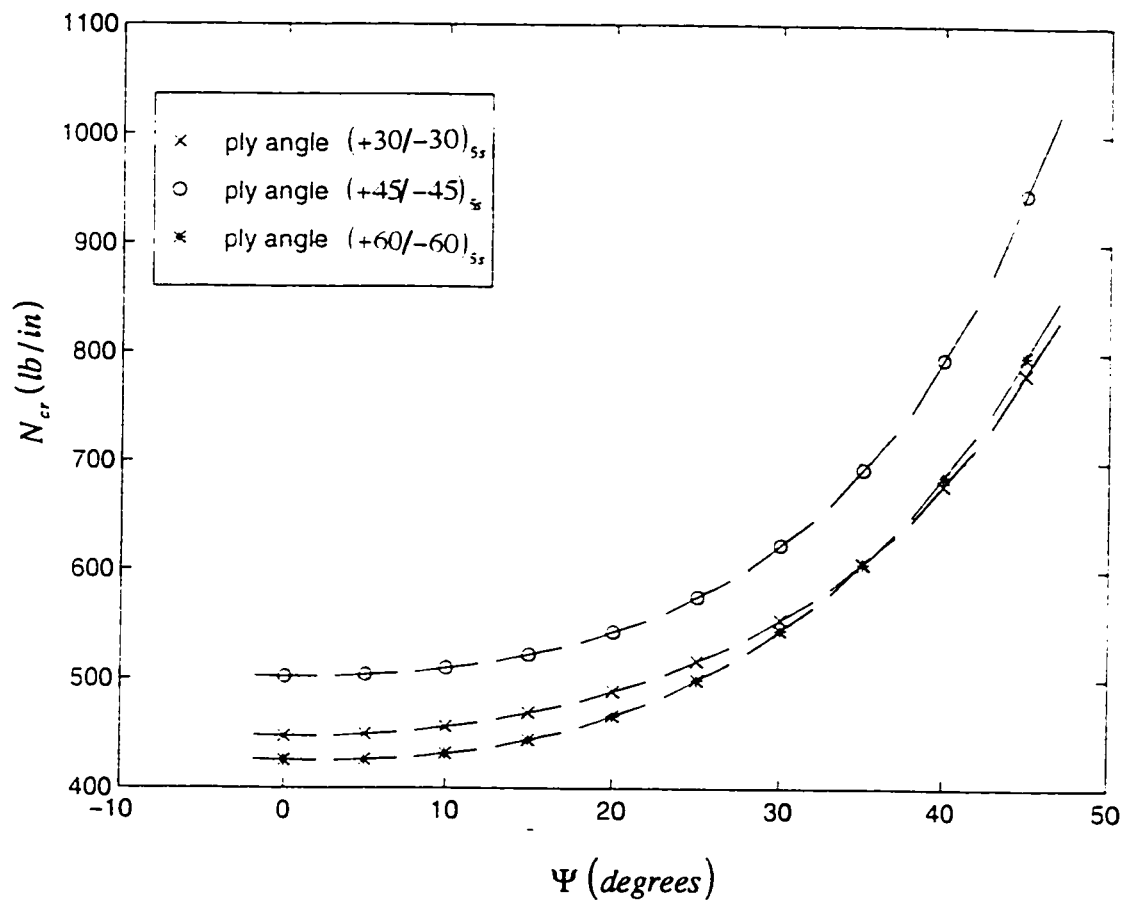


Figure 7.32 Buckling load coefficients and sensitivities for the anisotropic laminated skew plates

7.4 Box Beam under Uniform Compression

In order to assess the buckling behaviour and sensitivity for more complex structure, a box beam with variable section dimensions is examined. As it is illustrated in Figure 7.33, a box beam with width a , length L , height b , and a constant thickness t is used. The box beam is assumed to be simply supported on its open edges in the xy plane and subject to uniaxial compressive force per unit length N in the z direction.

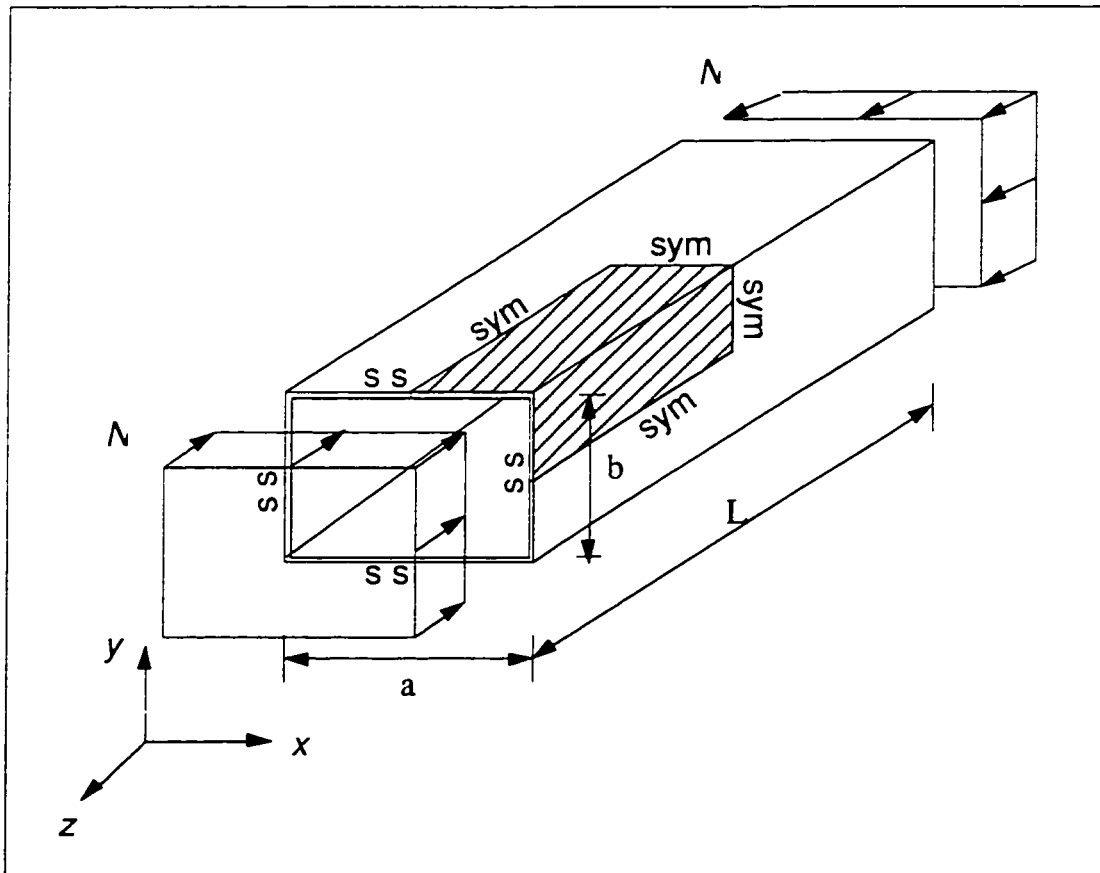


Figure 7.33 Box beam subject to uniform compression

The theoretical buckling stresses for the primary mode are available (BRU65) when the length L is relatively large compared to those of width and height of the box beam. Here the beam is assumed to have a length to width ratio $L/a = 7.0$ and a thickness to width ratio $t/a = 1/100$. From the parametric study, it is observed that the effect of the length on the critical buckling loads of the box beam is not significant with these ratios. The material properties are assumed to be the same as those of isotropic rectangular plate in section 7.1.1.

Since the structure and the applied loads are symmetric, only one eighth of the beam is analyzed. A typical finite element mesh is shown in Figure 7.34. In the finite element analysis the individual panel components are assumed to be connected rigidly so that the undeformed right angles between upper panel and side panel remain right angles as the structure deforms. In the sensitivity analysis, the height of the beam, b , is chosen as the shape design variable. Numerical results for both buckling and sensitivity analysis are shown in Table 7.21 when the design variable b is changed from 0.6 to 1.2 with $a = 1.0$ and comparisons of the buckling load coefficient defined as Eq. (7.17) are made with theoretical solutions available in (BRU65).

$$N_{cr} = \frac{K \pi^2 E t}{12 (1 - \nu^2) a^2} \quad (7.17)$$

The primary buckling mode shapes are found to be same for all design variables considered, and are shown in Figure 7.35. It is observed that very close agreement exists between the two for the given geometries of the box beam. The sensitivity results in Figure 7.36 show that the analytic sensitivity agrees with the trend in calculated buckling loads very well.

Table 7.21 Buckling load coefficient and sensitivity for the box beam

b	Reference k	Present Analysis k	Present Analysis $\frac{dk}{db}$
0.6	5.03	4.972	-1.68
0.7		4.863	-2.06
0.8	4.64	4.631	-2.95
0.9		4.332	-3.77
1.0	4.0	3.960	-4.30
1.1		3.554	-4.33
1.2		3.163	-3.96

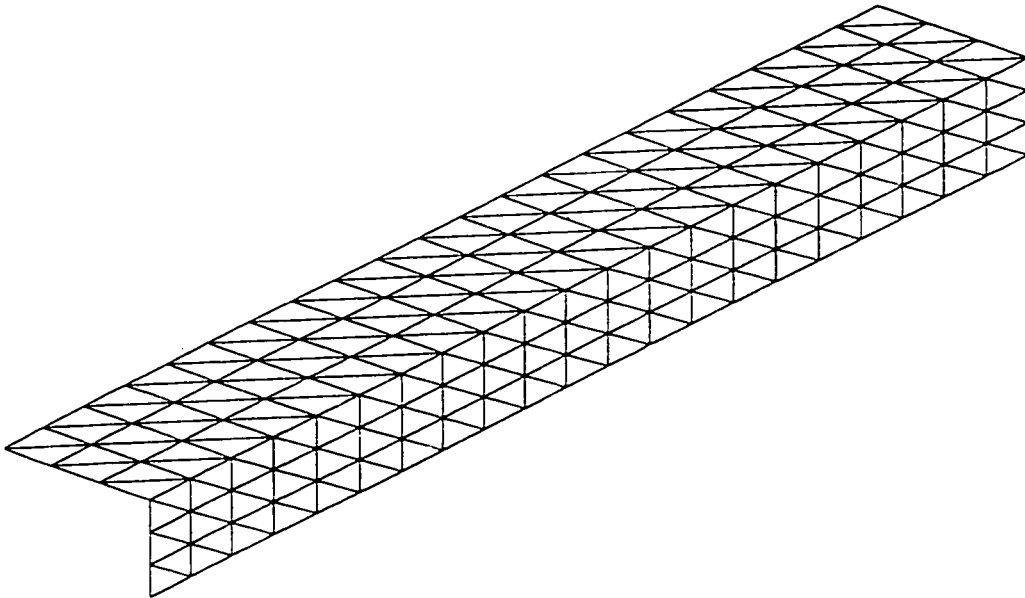


Figure 7.34 Finite element mesh configuration for the box beam

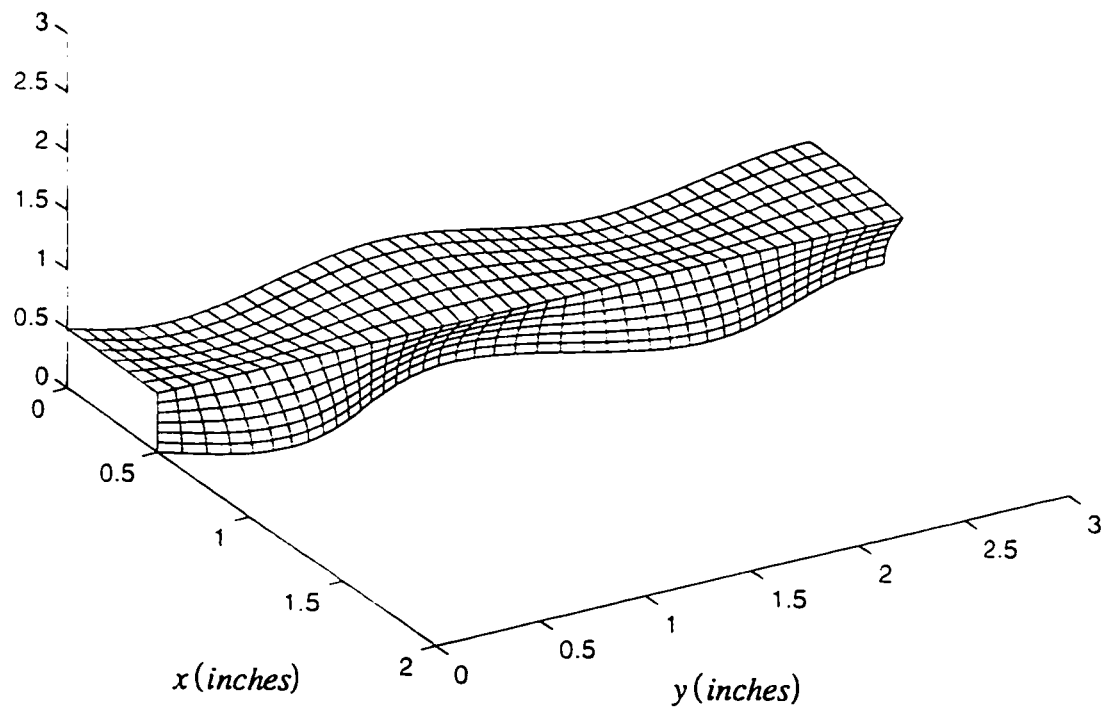


Figure 7.35 Mode shape for the critical mode of the box beam.

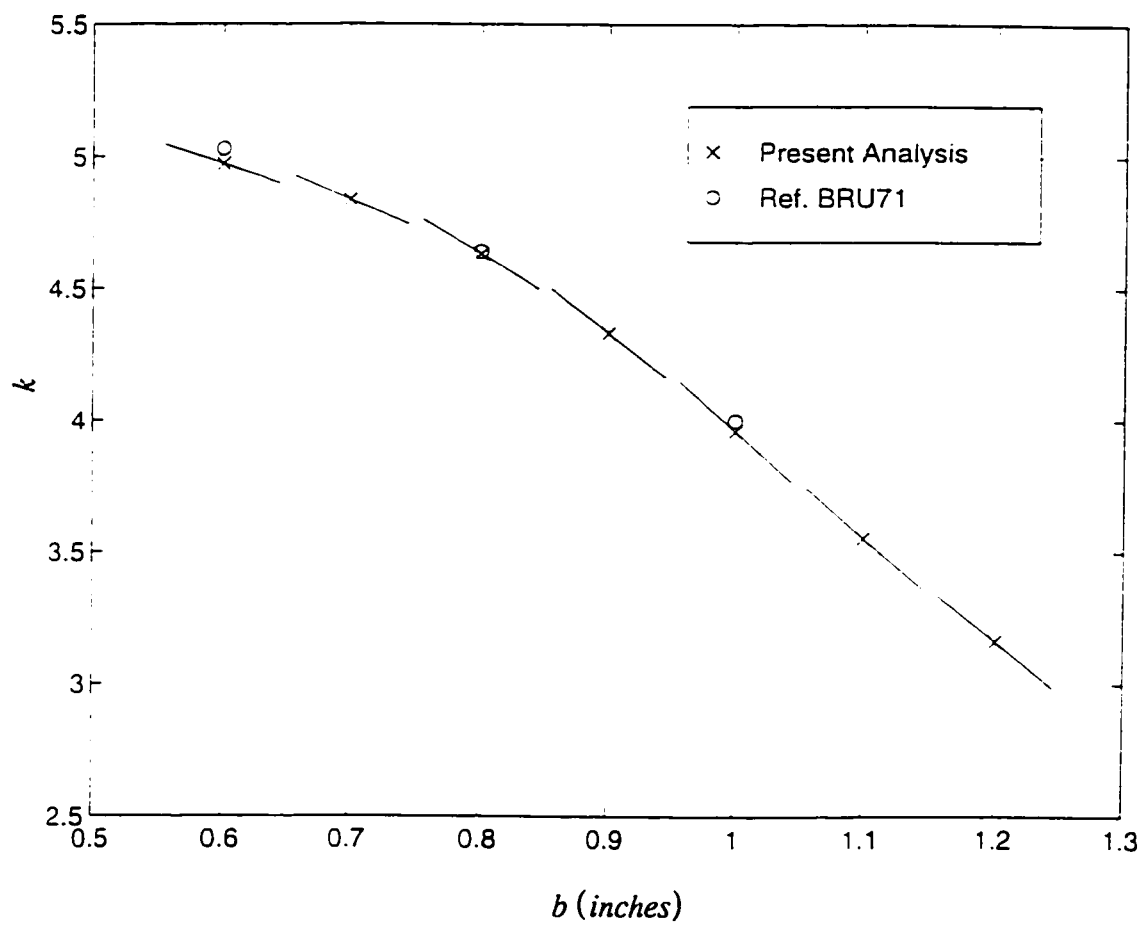


Figure 7.36 Buckling load coefficient and sensitivity for the box beam

7.5 Typical Fighter Wing

The wing of typical fighter airplane was chosen as the next example. It is a low aspect ratio clipped delta wing. The planform and finite element model of the simplified wing is presented in Figures 7.37-7.39. The wing is subjected to the aerodynamic force of 9G pull up. The wing has a conventional built up structure of aluminum with eleven spars and four ribs. A 3.5 % parabolic airfoil is used and no control surfaces are included in the model. In the finite element analysis, 354 flat shell elements were used for the ribs, spar panels as well as wing skin panels. The thicknesses of the shell element range from 0.06 to 0.42 inches. The root of the wing is assumed to be fixed to a rigid fuselage. The total number of degrees of freedom is 2678 which is reduced to 2457 after the fixed boundary conditions are applied at the root of the wing. The model is relatively coarse and is used to assess the behavior of the analytic sensitivity for a complex wing structure. This is considered more important here than resolving details in the structure.

A sweep-back angle α of the leading edge spar is chosen as the shape design variable in the sensitivity analysis. The area of wing planform is kept fixed during the change of the design variable so that the dependence of the buckling behavior on the aerodynamic force is not significant. Figure 7.40 shows how the wing is changed as the design variable is increased from 35.125 to 45.125 degree.

Figure 7.41 shows the deformed shape of the wing under the aerodynamic force when shape design variable α is 35.125 degree (no aeroelastic correction is included). The transverse deflections of the wing tip at the trailing edge are presented in Table 7.22 with their sensitivities when α is varied from 22.125 to 42.125.

Table 7.22 Transver deflection at the trailing edge wing tip and sensitivity

Swept-back angle α (degree)	Wing tip Displacement	Displacement Sensitivity
22.125	8.425	0.106
24.125	8.667	0.136
26.125	8.972	0.172
28.125	9.362	0.214
30.125	9.839	0.265
32.125	10.427	0.326
34.125	11.151	0.402
36.125	12.054	0.497
38.125	13.165	0.618
40.125	14.552	0.772
42.125	16.280	0.971

It is observed that the trailing edge wing tip displacement increases as the sweep angle α is increased. In Figure 7.42, the sensitivity results of the wing tip deflection are illustrated as slopes of the deflection with a variation of design variable α and the good agreement with the curve can be seen.

In order to examine the effect of the design variable on the stress distributions, the local membrane stresses at three Gaussian quadrature points are presented in Table 7.23 for

the wing skin element numbered 338 shown in Figure 7.39. These are obtained with $\alpha = 35.125$ and their sensitivities are also shown in this table.

Table 7.23 Membrane stresses and sensitivities at gaussian points for element 338
($\alpha = 35.125$)

	σ_x	$\frac{\partial \sigma_x}{\partial \alpha}$	σ_y	$\frac{\partial \sigma_y}{\partial \alpha}$	τ_{xy}	$\frac{\partial \tau_{xy}}{\partial \alpha}$
1st Gaussian point	-99.6	-25.9	-199.5	4.5	-245.7	1.1
2nd Gaussian point	1214.7	-20.9	-299.3	15.6	-405.1	-2.4
3rd Gaussian point	217.9	-26.9	15.6	13.1	-26.9	13.7

It is observed that there exists a wide range of membrane stresses in the element. For example, σ_x changes from -99.6 to 1214.7 psi. It can be deduced from this result that the stress distributions over the element have high gradients. Since the L.S.T. membrane element recovers linear stress distributions over the element, and since in the current model the elements are large, a refined mesh would approximate the stress distributions more accurately. However, the object of this study is to assess the behavior of buckling load and its analytic sensitivity while retaining a manageable number of degree of freedom. A refined finite element mesh would exceed the capacity of the computer available and is not attempted here.

The variations of the three local membrane stress components σ_x , σ_y and τ_{xy} at the first Gaussian point of the element are shown in Figure 7.43 with their sensitivities as the design variable changes, and the stresses and sensitivities at three quadrature points can be seen in Figure 7.44 - 7.46. In these figures, small oscillations of the stress components are observed as the design variable α changes, especially for σ_y and τ_{xy} . It is to be noted that uniform stress distributions were approximated in the previous examples and thus this oscillatory behavior of membrane stresses was not observed. It is thought that this oscillatory behavior is mainly due to the insufficient number of elements used for this complicated wing structure with the resulting highly nonlinear stress distribution, as mentioned earlier. However, the relative magnitude of the oscillation is not large compared to the magnitude of the stress, as can be noted in Figure 7.43. That figure also shows that the sensitivities of the stress components are consistent with the global tendency of the stresses regardless of the oscillatory behavior. This can be seen clearly from the slopes of σ_y at the third quadrature point in Figure 7.45, where the stress reaches its maximum at about $\alpha = 40.0$ and by the fact that the sign of the slope changes from minus to plus at this point although there is a small oscillation in the stresses.

The next step is to calculate the buckling load coefficients, and numerical results for the buckling and sensitivity analyses are shown in Table 7.24 for the lowest five modes of the wing with $\alpha = 32.125$. The corresponding buckling mode shapes are shown in Figures 7.47 - 7.52, which are named Mode A, B, C, D and E respectively. It is observed that the buckling coefficients λ , for the first two lowest modes are below 1.0 and that the buckling coefficients for the lowest five modes are close to one another.

Figure 7.24 Buckling load coefficients and sensitivity ($\alpha = 35.125$)

Mode	λ	$\frac{\partial \lambda}{\partial \alpha}$	Mode Shape
1st	0.9180	-0.00455	A
2nd	0.9685	-0.00840	B
3rd	1.1054	-0.00993	C
4th	1.1805	-0.00858	D
5th	1.2090	-0.01387	E

Since the wing buckles at a critical load equal to the critical buckling load coefficient multiplied by the applied aerodynamic load, values of λ less than 1.0 indicate that the wing would have buckled under the given aerodynamic force. In the five lowest modes, the upper wing skin panels between first and second ribs, named sp1, sp2,...sp9, from the trailing edge to the leading edge, buckled, due to the relatively long distance between those two ribs and the compressive loads in those panels induced by the aerodynamic load. It is also noted that the buckling modes do not correspond the buckling of a single isolated panel, but are characterized by the buckling of more than one subcomponent panels, although the interactions are not shown clearly because of the scale used to draw the deformed shape. For example, the upper skin panel sp1 and the adjacent panel sp2 buckle in the Mode A, while the buckling of the three connected panels from sp5 to sp7 is characterized by Mode B.

To compare the buckling load coefficients obtained from this global buckling analysis and a local buckling analysis, a local buckling analysis has also been performed for the isolated panels.

Two upper skin panels located between the first and second ribs are chosen for the local analysis and each panel is assumed to buckle independently from the others. The first one, sp1, is the skin panel attached to the trailing edge spar. The other one sp6 is located between the sixth spar and seventh spar from the trailing edge. The buckling of these two panels are observed dominant in the first and second critical modes of the global buckling analysis as shown in Figure 7.47 and 7.48. The same finite element mesh as the global finite element model is used to obtain the buckling load coefficients of the isolated panels, and the membrane stress distributions of the panel are extracted from the finite element analysis of the global model of the wing. These stresses, which vary linearly in each element, are then used in the formulation of the geometric stiffness matrix. Since the boundaries of the wing skin panels are assumed to be attached to the surrounding rib and spar panels which are not fixed, the boundary conditions for the isolated panels cannot be determined in a unique way. Two sets of boundary conditions are applied for the finite element model of the local panel: simply supported and fixed along all edges. Most previous work regarding the optimization of wing structure with buckling constraints adopted simply supported boundary conditions to the isolated panels (SH79, SM82, RGS94).

Numerical results of the local buckling analysis are shown in Table 7.25 and 7.26 for the skin panel sp1 and sp2. As expected, the critical λ for the isolated skin panel sp1 is closer to the first lowest λ of global analysis and the critical λ for sp6 to the second lowest λ when simply supported boundary conditions are applied. The similarities are also observed in the corresponding mode shapes of the panels. When only the critical mode

is considered as one of the constraints in the optimization, the lowest λ obtained from the local buckling analysis for sp1 will be assumed.

Table 7.25 Comparison of λ between global and local analysis for sp1

	Local Analysis		Global Analysis
	S.S	Fixed	
1st lowest mode	0.879	0.965	0.918
2nd lowest mode	1.076	1.633	
3rd lowest mode	1.469	2.569	

Table 7.26 Comparison of λ between global and local analysis for sp6

	Local Analysis		Global Analysis
	S.S	Fixed	
1st lowest mode	0.950	1.003	
2nd lowest mode	1.221	1.317	0.968
3rd lowest mode	1.459	3.704	

The critical λ obtained from global analysis, 0.918, is in between the ones obtained by applying simply supported and clamped boundary conditions in the local analysis: 0.879 and 0.965, respectively. The buckling load of the panel with clamped boundary condition is higher than the one with simply supported boundary condition as expected, and it can be concluded that the correct boundary conditions of an isolated panel of the wing structure are in between clamped and simply supported. As a result, more efficient design can be

obtained in the design of a wing structure when the global buckling load of the structure is considered instead of the local buckling load of a simply supported isolated panels. This is consistent with the results of the former wing box analysis with a buckling constraint (RGS94) , in that case the optimum weight of a wing box is reduced when global buckling constraints are imposed instead of local ones .

Since a few lowest modes are of major concern in the design of the wing, the buckling coefficients and their sensitivities for the first two modes are obtained as the design variable α changes from 25.125 to 45.125 degree and the numerical results are presented in Table 7.27.

Table 7.27 Buckling load coefficients and sensitivities for the first two critical modes

Swept-back angle α (degree)	First Critical mode		Second Critical mode	
	Coefficient	Sensitivity	Coefficient	Sensitivity
25.125	0.963	- 0.0047	1.035	- 0.00363
27.125	0.958	- 0.0052	1.024	- 0.00532
29.125	0.946	- 0.0058	1.037	- 0.00655
31.125	0.941	- 0.0062	1.002	- 0.00732
33.125	0.917	- 0.00585	1.005	- 0.00822
35.125	0.918	- 0.00455	0.968	- 0.00840
37.125	0.898	- 0.00243	0.953	- 0.00850
39.125	0.903	0.00156	0.949	- 0.00871
41.125	0.912	0.00730	0.920	- 0.00787
43.125	0.903	- 0.00714	0.933	0.0151
45.125	0.890	- 0.00612	0.968	0.0268

In order to see the buckling behavior, both buckling load coefficients and sensitivities are illustrated in Figure 7.52 for those two modes.

Since the geometric stiffness matrix depends on the membrane stresses linearly, as in Eq. (3.56), the oscillatory behavior of the stresses with the change of α has been propagated to the buckling load coefficients as the sweep angle is changed. However, the magnitude of the oscillations is not large compared to λ : and their sensitivities, the slope of the buckling load coefficient curve, are not affected by the oscillation and show reasonable trends of buckling loads in the entire region of the design variables.

It is observed that the signs of their sensitivities change when α is increased from 41.125 to 43.125 degrees. The sensitivities for the two lowest modes are changed from 0.00730 and - 0.00787 to - 0.00714 and 0.0151 for Mode A and B, respectively, as shown in Figure 7.52. The buckling mode shapes for the two modes are identified at each design variable and the results are plotted in Figure 7.53. In this figure, the switch of the two modes is observed as was predicted based on the sensitivity results.

Since the finite difference scheme calculates the sensitivity of an eigenvalue using discrete eigenvalues only, it is necessary to track the intended mode when the design variables are changed, which requires additional computation (EVA93).

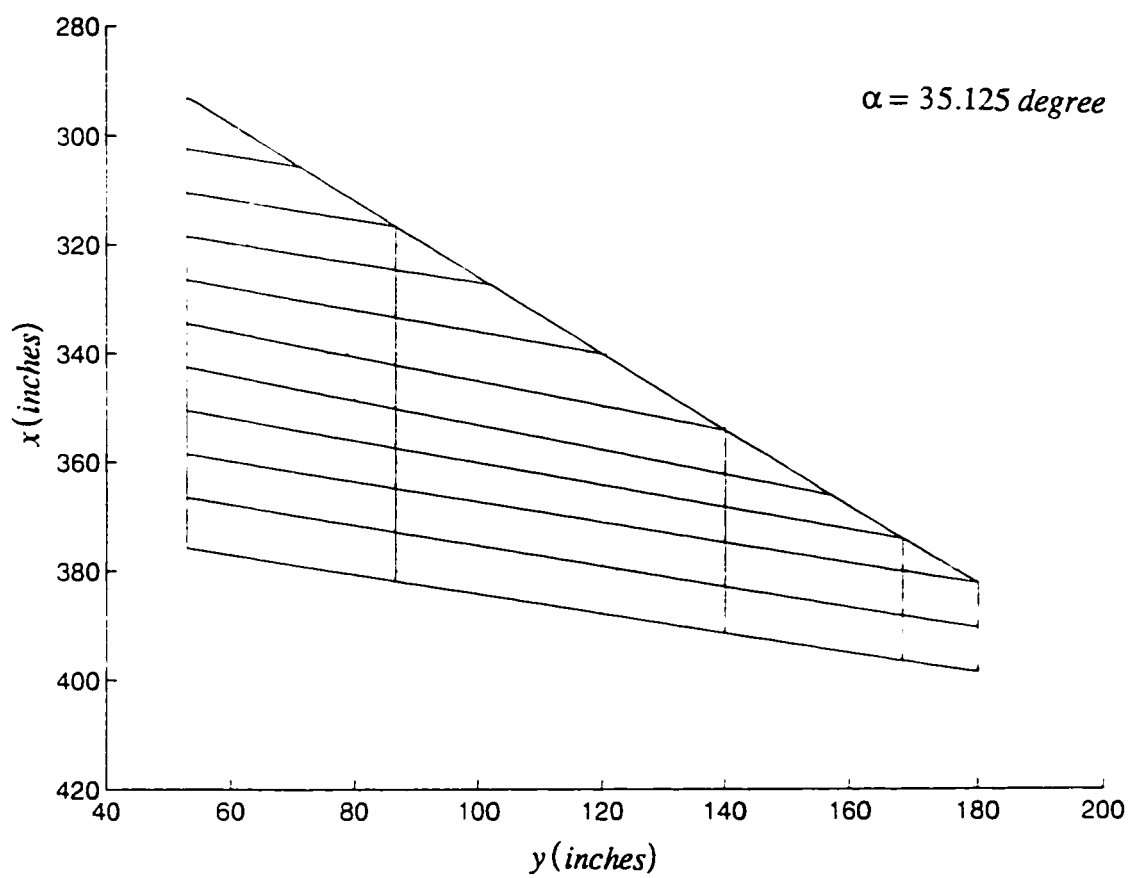


Figure 7.37 Planform for the typical fighter wing

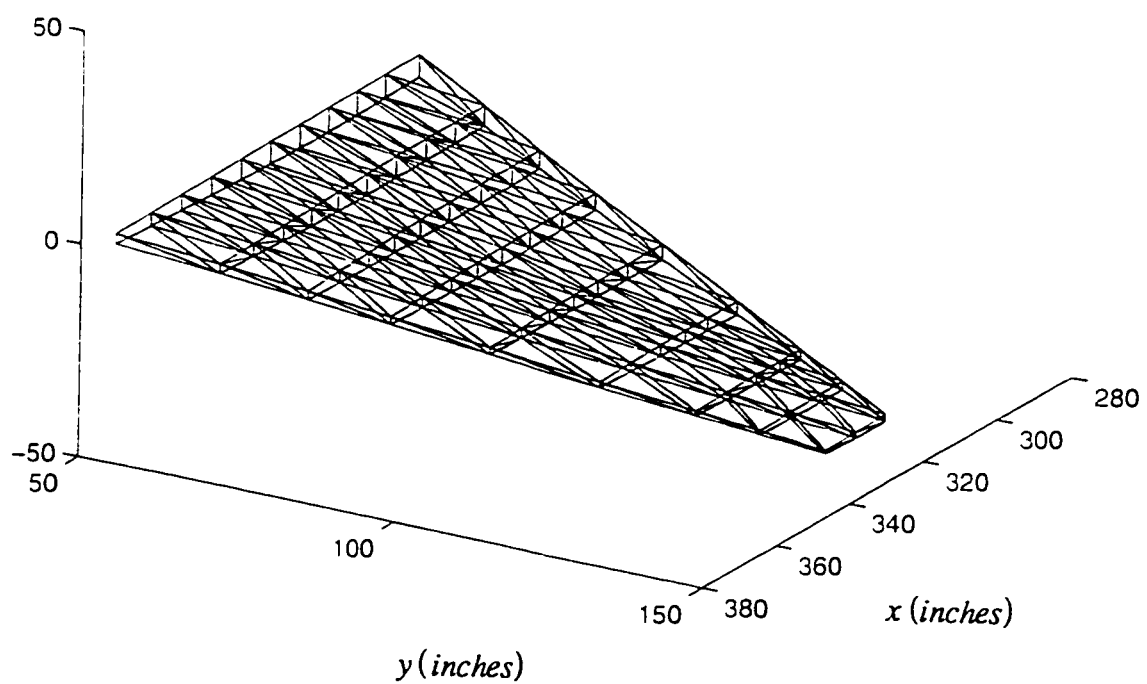


Figure 7.38 Finite element mesh configuration for the typical fighter wing

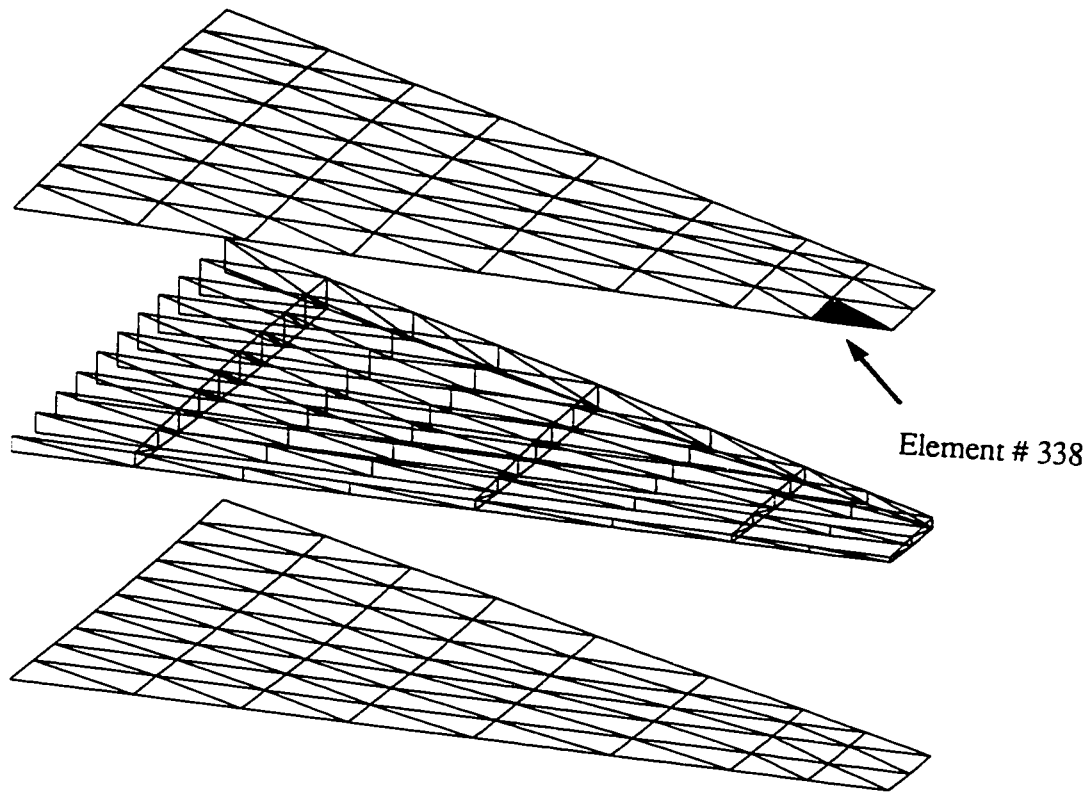


Figure 7.39 Finite element mesh configuration in detail for the typical fighter wing

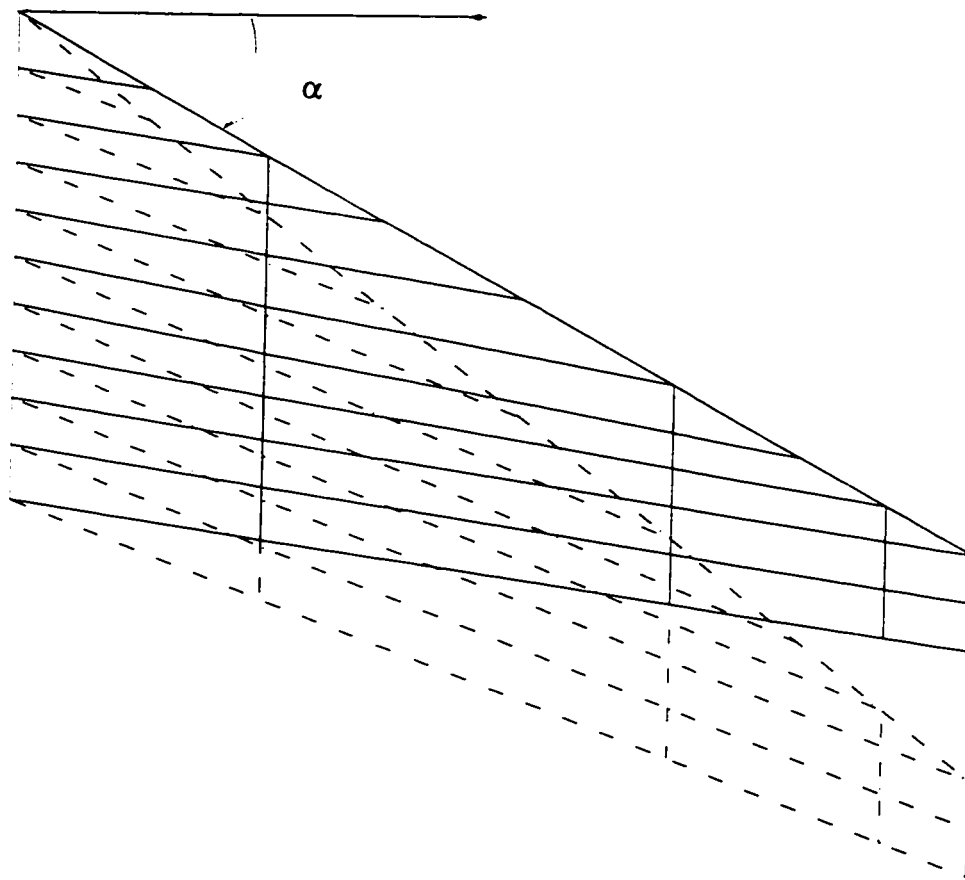


Figure 7.40 Variation of planform for the typical fighter wing

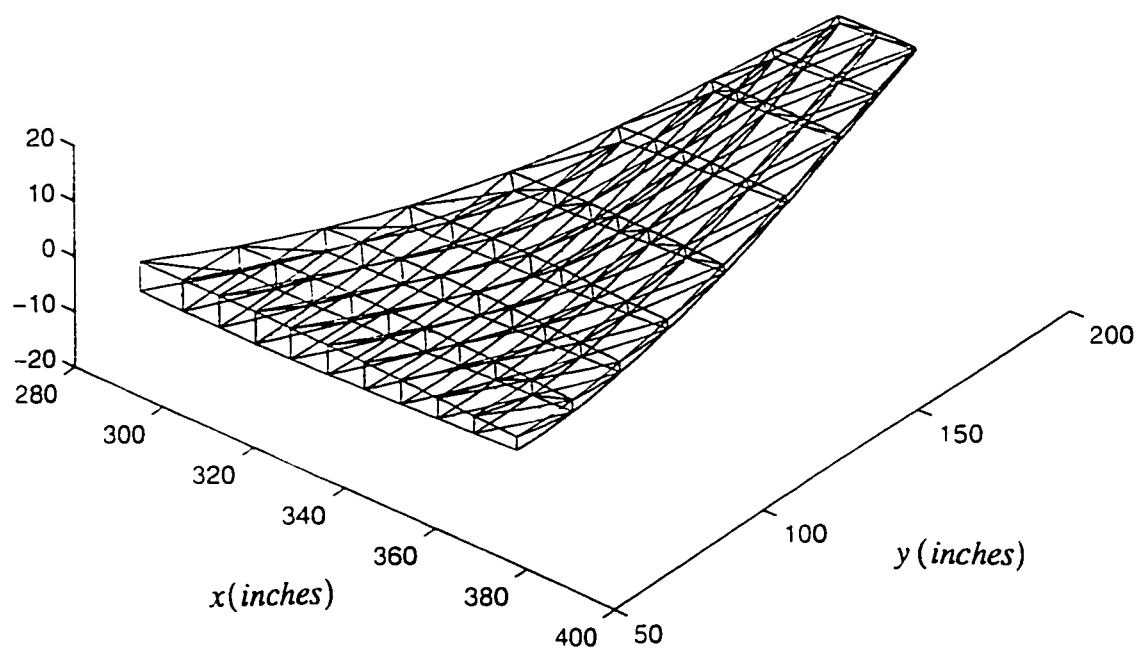


Figure 7.41 Deformed shape of the typical fighter wing under aerodynamic force
(9G pull-up)

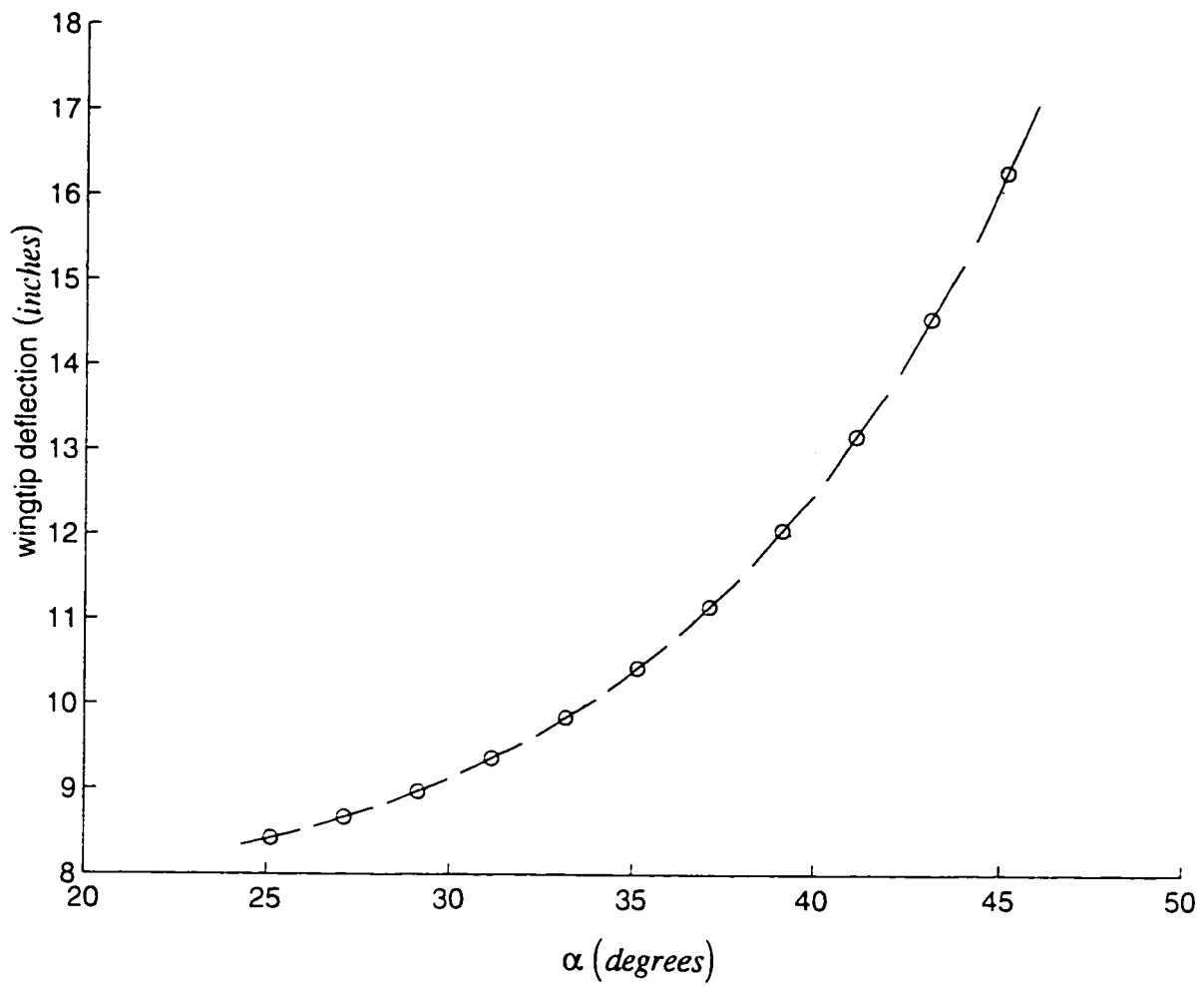


Figure 7.42 Wingtip trailing edge deformation and sensitivity for the typical fighter wing.

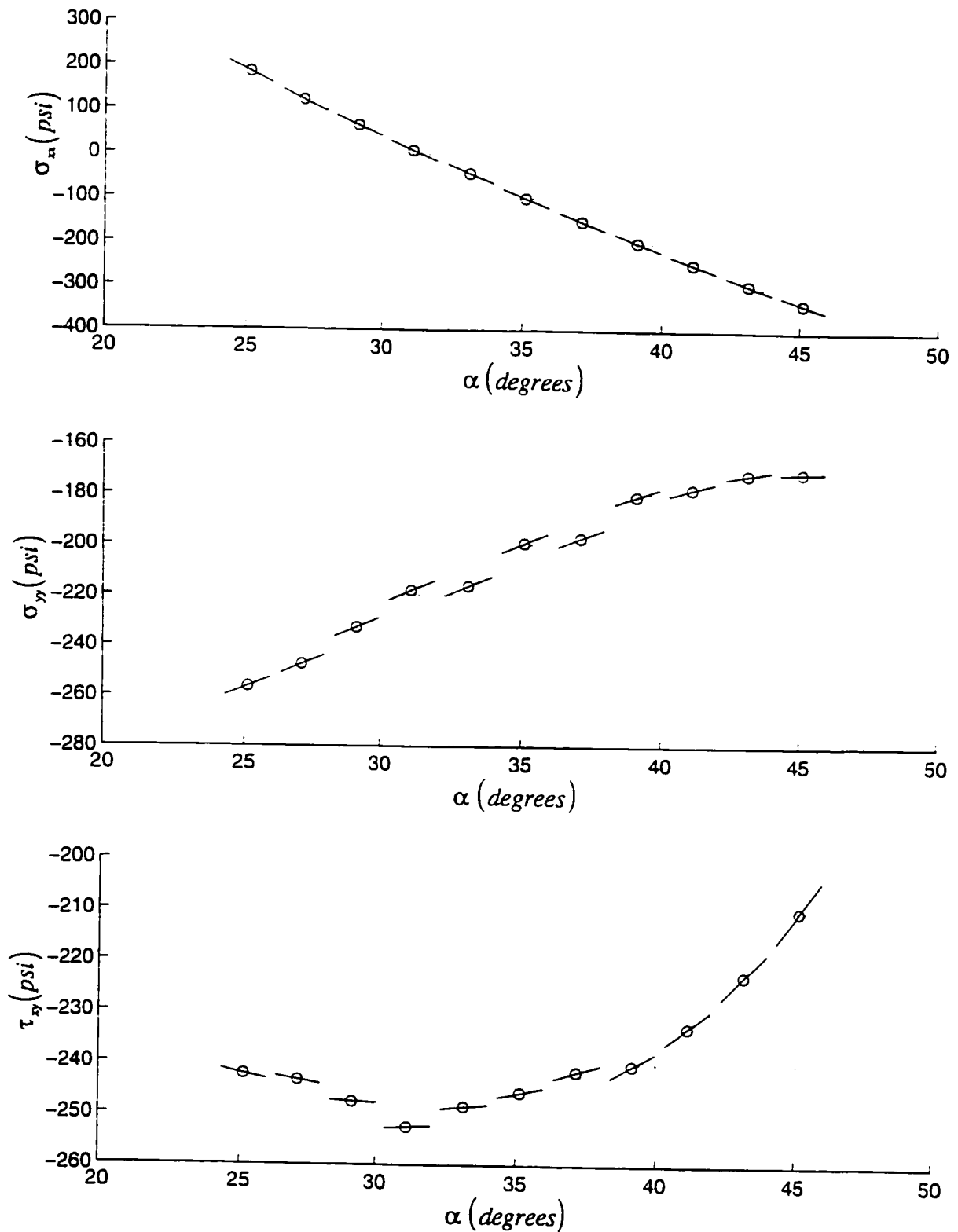


Figure 7.43 Stresses and sensitivities at the element 338 for the typical fighter wing.

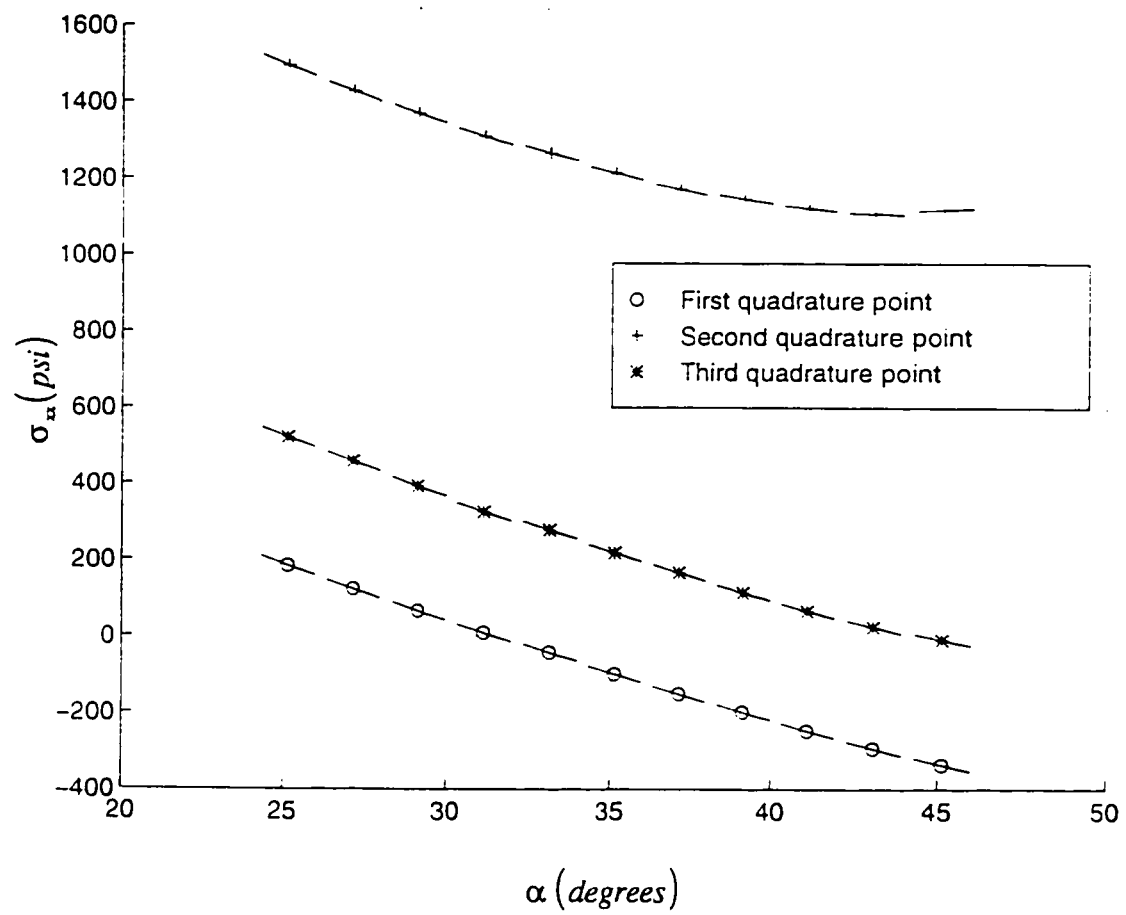


Figure 7.44 Comparison of stress σ_x at the element 338 for the typical fighter wing.

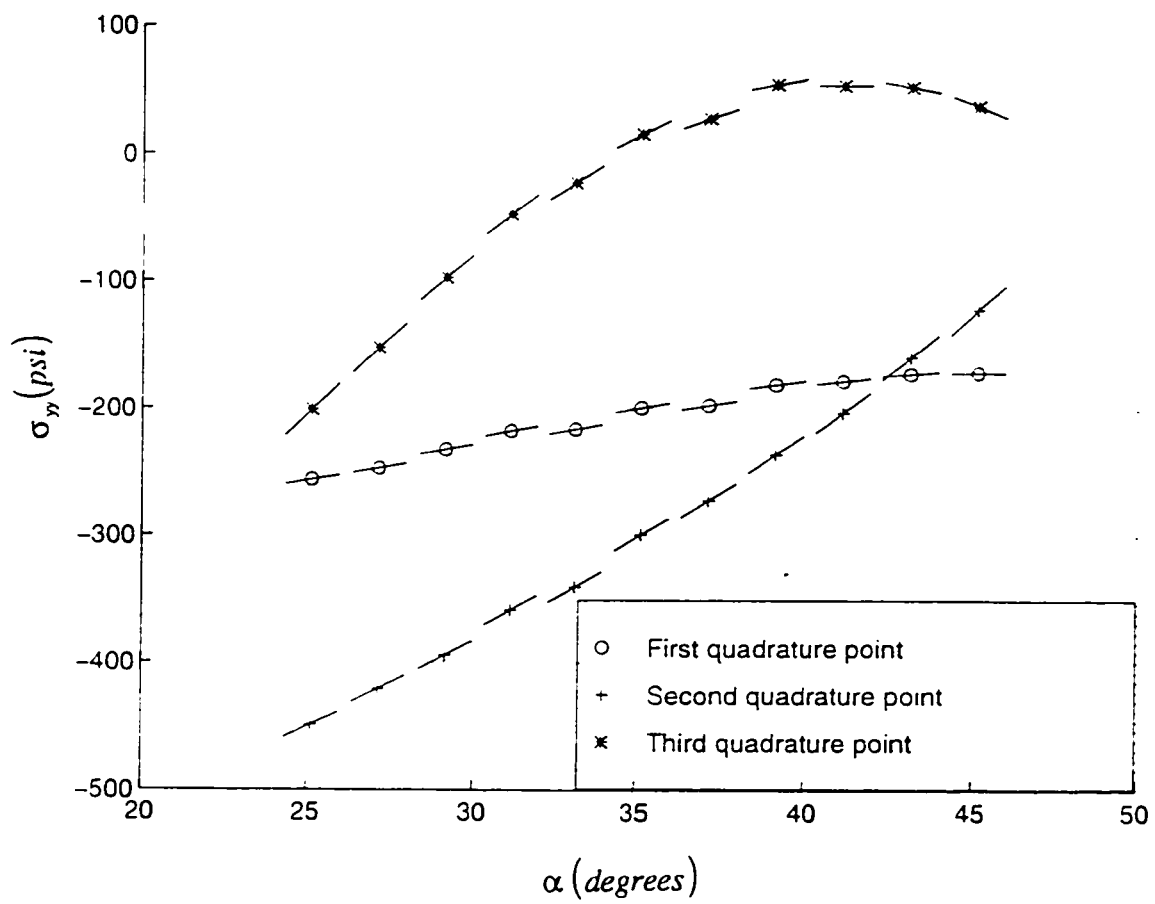


Figure 7.45 Comparison of stress σ_y at the element 338 for the typical fighter wing.

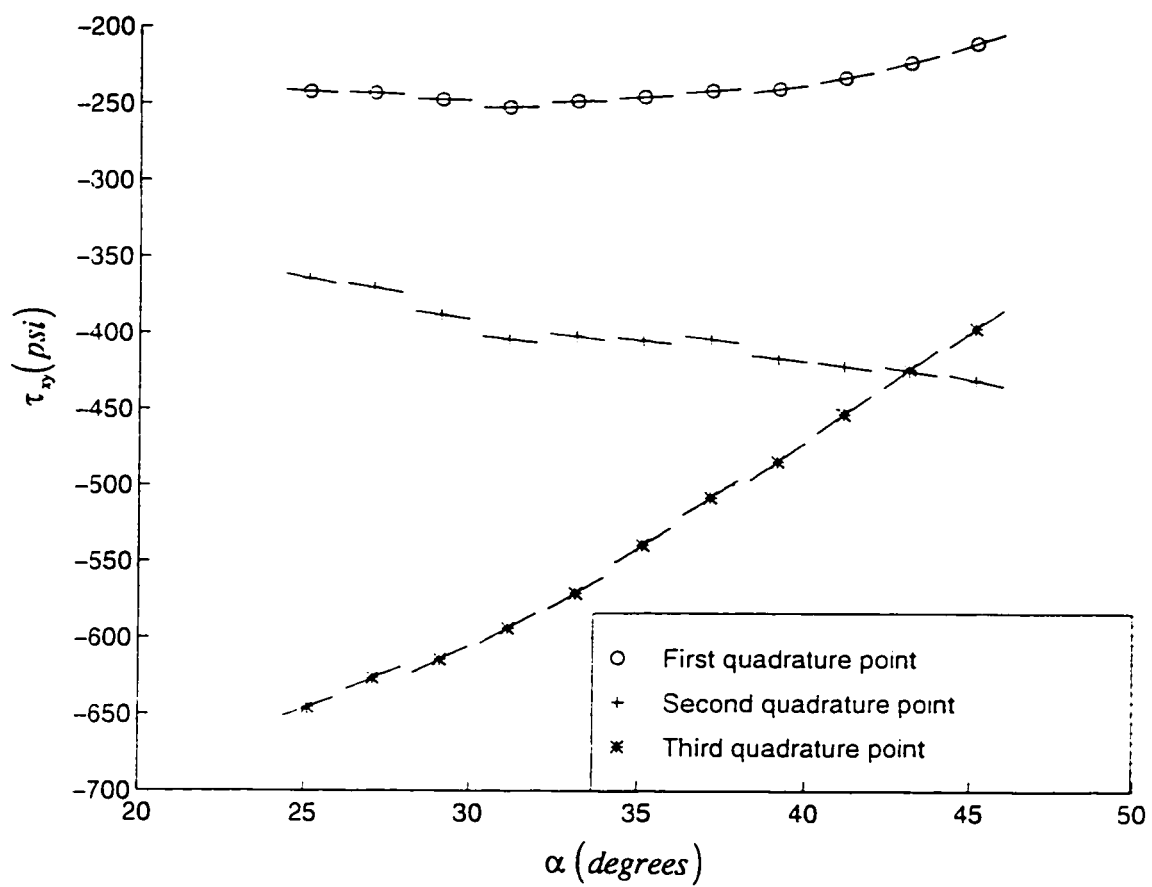


Figure 7.46 Comparison of stress τ_{xy} at the element 338 for the typical fighter wing.

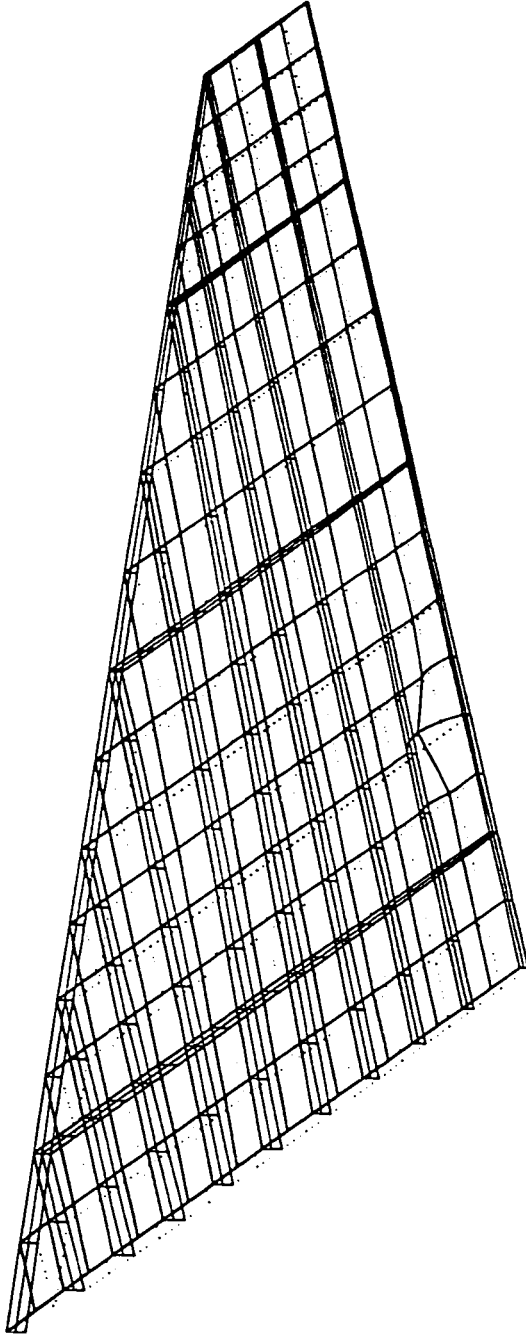


Figure 7.47 Mode shape (Mode A) for the critical mode of the wing ($\alpha = 35.125$).

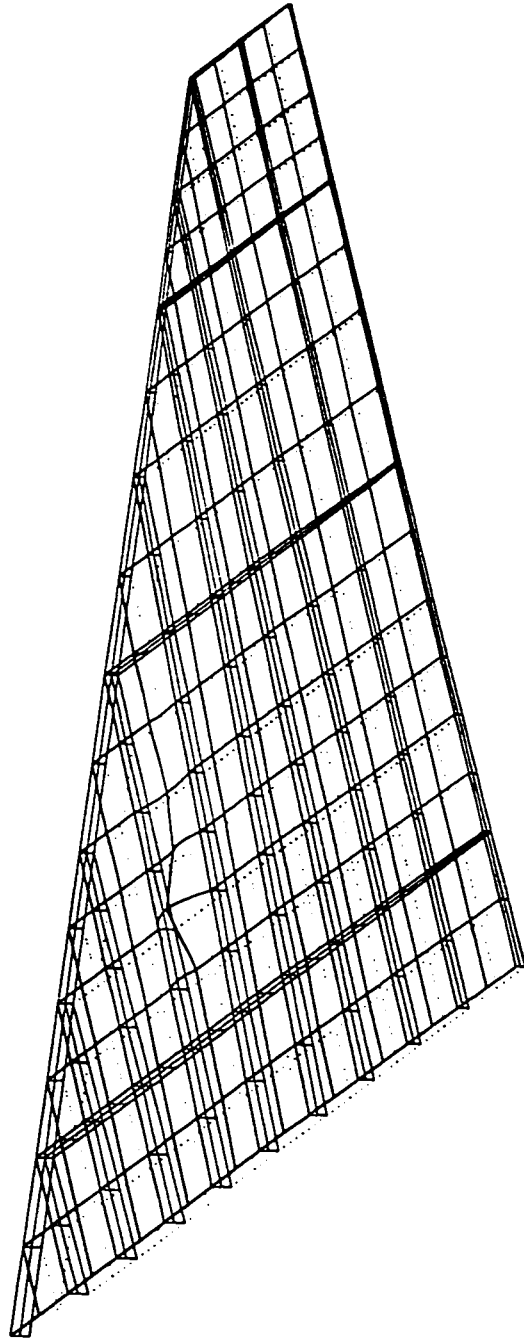


Figure 7.48 Mode shape (Mode B) for the second mode of the wing ($\alpha = 35.125$).

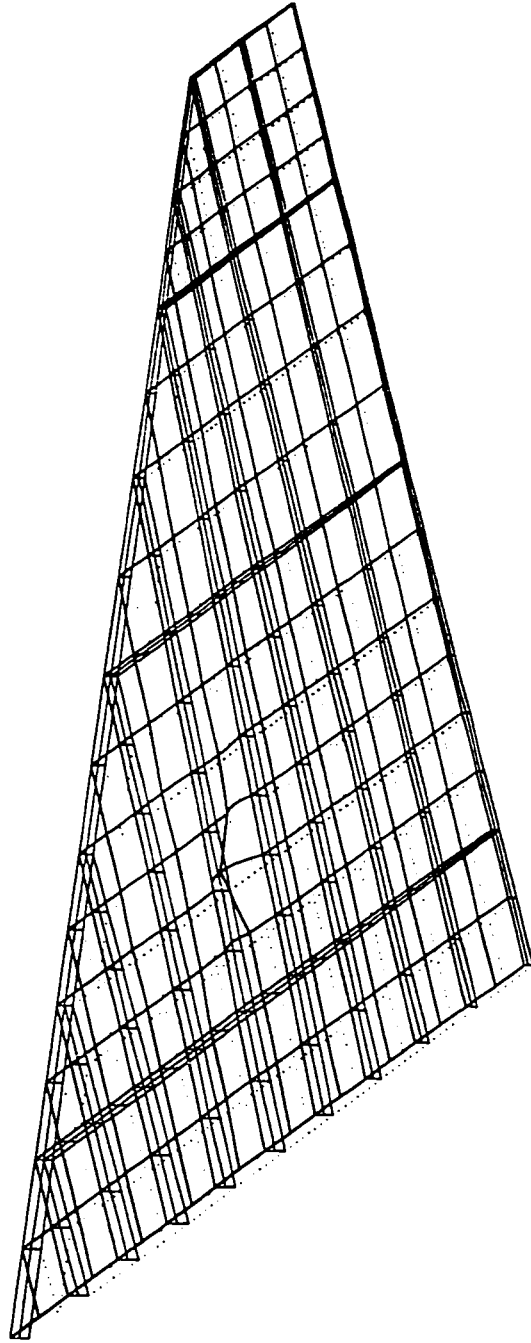


Figure 7.49 Mode shape (Mode C) for the third mode of the wing ($\alpha = 35.125$).

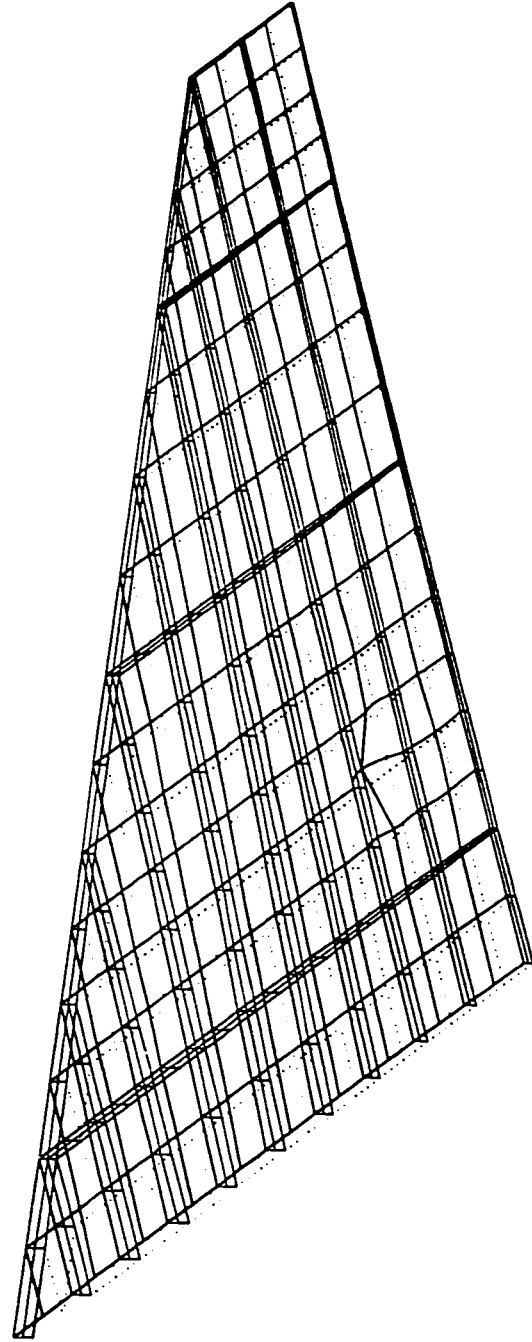


Figure 7.50 Mode shape (Mode D) for the fourth mode of the wing ($\alpha = 35.125$).

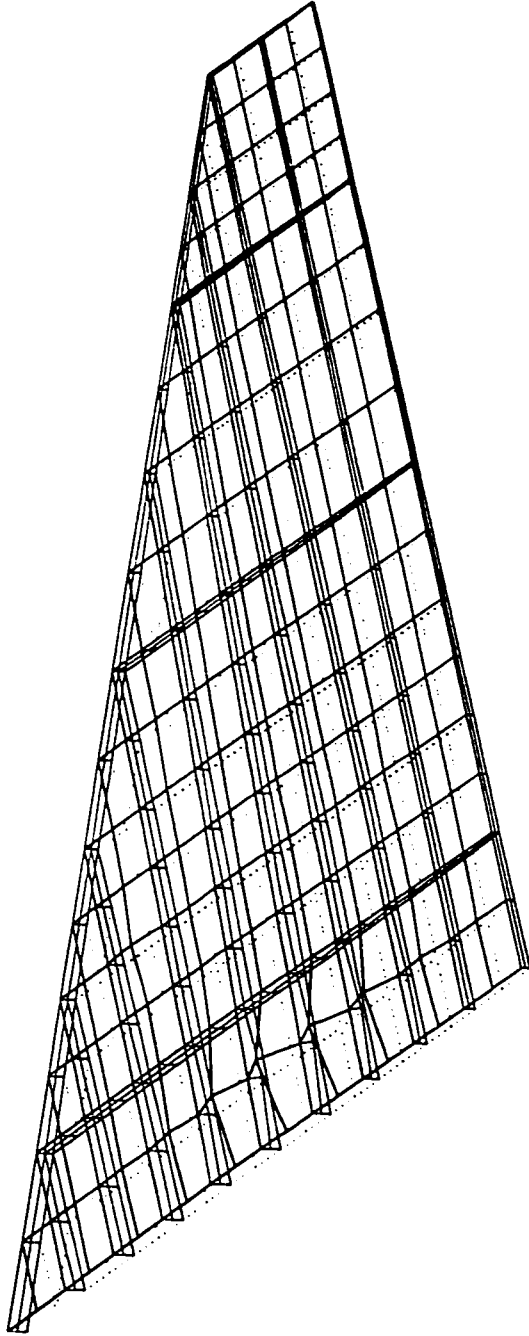


Figure 7.51 Mode shape (Mode E) for the fifth mode of the wing ($\alpha = 35.125$).

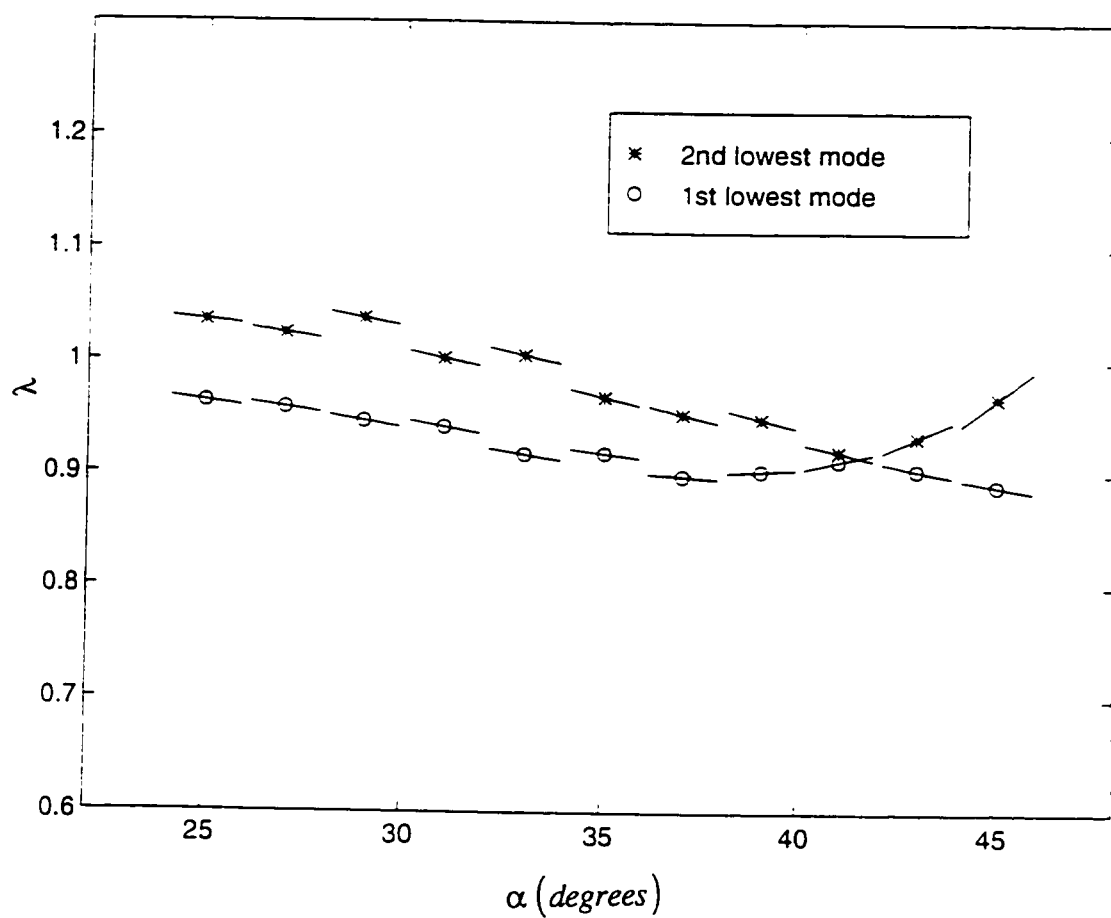


Figure 7.52 Buckling load coefficients and sensitivities for the two lowest modes of the wing

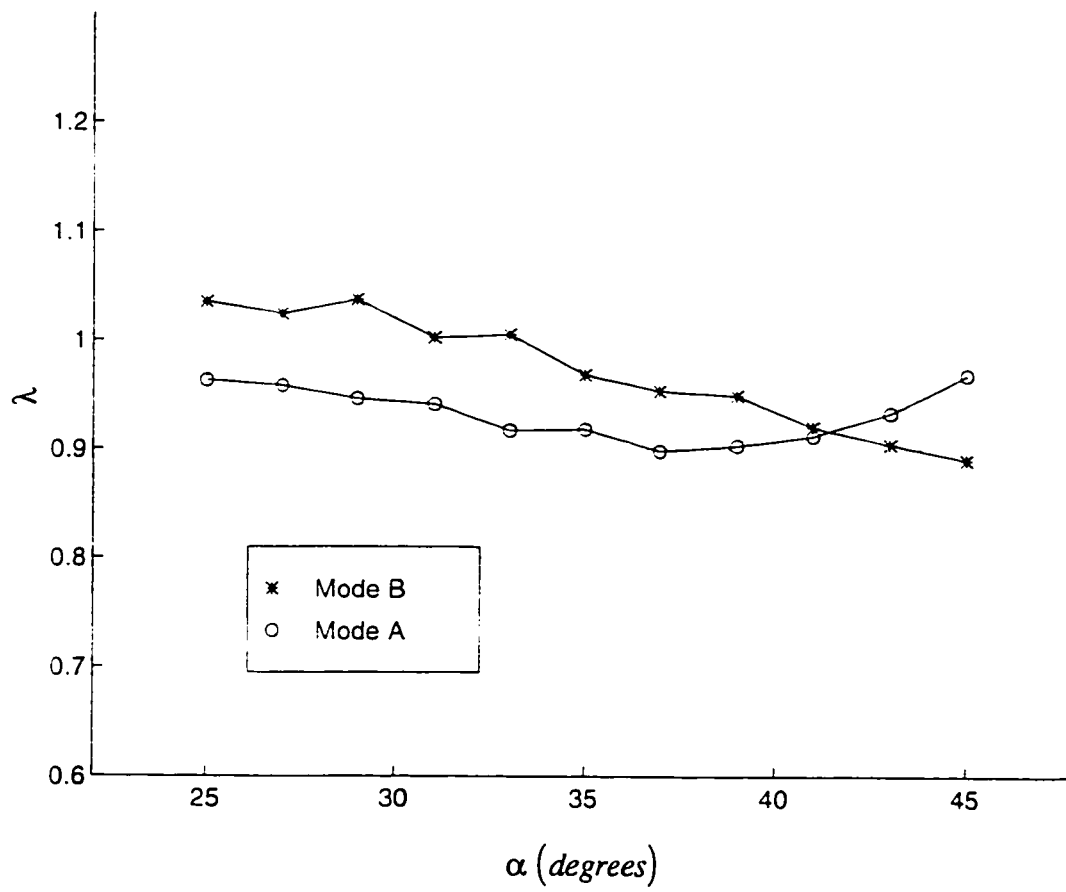


Figure 7.53 Buckling load coefficients and modes for the wing

Chapter 8

Numerical Results (Order Reduction)

Various order reduction methods based on Chapter 6 have been implemented in the existing finite element code. In this chapter, numerical results are presented for the buckling load and its sensitivity obtained from the reduced order eigensystem as the shape design variable changes.

In order to assess the behavior of reduced order models, two examples, a simply supported rectangular plate under uniaxial compression and typical fighter wing from Chapter 7, were examined to address the following issues: 1) the comparison between results from fixed mode and variable mode methods when exact matrices are used for the order reduction (which indicates the accuracy of basis vectors for the approximation of mode shape), 2) the conservative approximation methods for the system matrices when the basis vectors are chosen from fixed mode methods, 3) the comparison between results from reduced order system and Rayleigh quotient approximation.

8.1 Simply supported rectangular plates under uniaxial compression

Since the theoretical solutions are available, simply supported isotropic rectangular plate under uniform compression shown in Figure 7.1 was selected to assess the present capability. In the sensitivity analysis, the length of the plate a is chosen as a shape design variable. The same material properties and thickness are assumed and 4×4 mesh shown

in Figure 7.2 has been used in this section to obtain the buckling load coefficients k and their sensitivities using the reduced order system.

First, full order buckling analysis was carried out for the plate with $a_0 = 12.0$ and $b = 10.0$ and the corresponding mode shapes for the two lowest modes were chosen as the basis vectors for the reduced system in which new system matrices are obtained exactly. Table 8.1 shows the buckling results for the primary mode as the shape design variable a is changed from -35% to 35% of a_0 .

When the design variable is increased by more than 15% and decreased by 35 %, the predicted mode shape obtained from fixed mode method was wrong while this false modeswitch was observed at 35 % increase in the variable mode method. Figure 8.1 shows that the buckling results obtained from variable mode method are better than those from fixed mode method, which indicates the mode shapes are approximated more accurately in variable mode methods as the design variable changes. It is noted that buckling load is overestimated when approximated eigenvectors are used to reduce the order of the matrices. As can be seen in Figure 8.2, the buckling results from reduced system showed good agreement with exact ones when the design variable is changed by a small amount. Comparing the variable mode method, the fixed mode method predicted much worse sensitivity result, which indicates the importance of basis vector sensitivity in the calculations of buckling load sensitivity in Eq. (6.8).

Table 8.1 Comparison of Buckling Load and Sensitivity from order reduction for the rectangular plates

Design variable	Fixed Mode k ($\frac{dk}{da}$)	Variable Mode k ($\frac{dk}{da}$)	Exact k ($\frac{dk}{da}$)
7.8	54.61(-31.1)*	10.81(-7.61)	4.252(-0.26)
8.4	38.29(-23.6)	7.340(-4.22)	4.123(-0.17)
9.0	25.95(-17.6)	5.466(-2.18)	4.045(-0.094)
9.6	16.95(-12.5)	4.544(-1.00)	4.007(-0.034)
10.2	10.75(-8.31)	4.159(-0.35)	4.002(0.015)
10.8	6.815(-4.92)	4.052(-0.044)	4.024(0.057)
11.4	4.721(-2.15)	4.070(0.081)	4.069(0.093)
12.0	4.134(0.12)	4.134(0.12)	4.134(0.12)
12.6	4.794(2.02)	4.218(0.16)	4.217(0.15)
13.2	6.497(3.61)	4.340(0.25)	4.316(0.17)
13.8	9.036(4.75)	4.548(0.45)	4.429(0.20)
14.4	11.77(4.12)*	4.918(0.80)	4.556(0.22)
15.0	14.28(4.41)*	5.547(1.32)	4.694()
15.6	17.09(5.01)*	6.483(1.06)	4.844()
16.2	20.26(5.56)*	6.766(0.54)*	5.005()

* incorrect mode shape

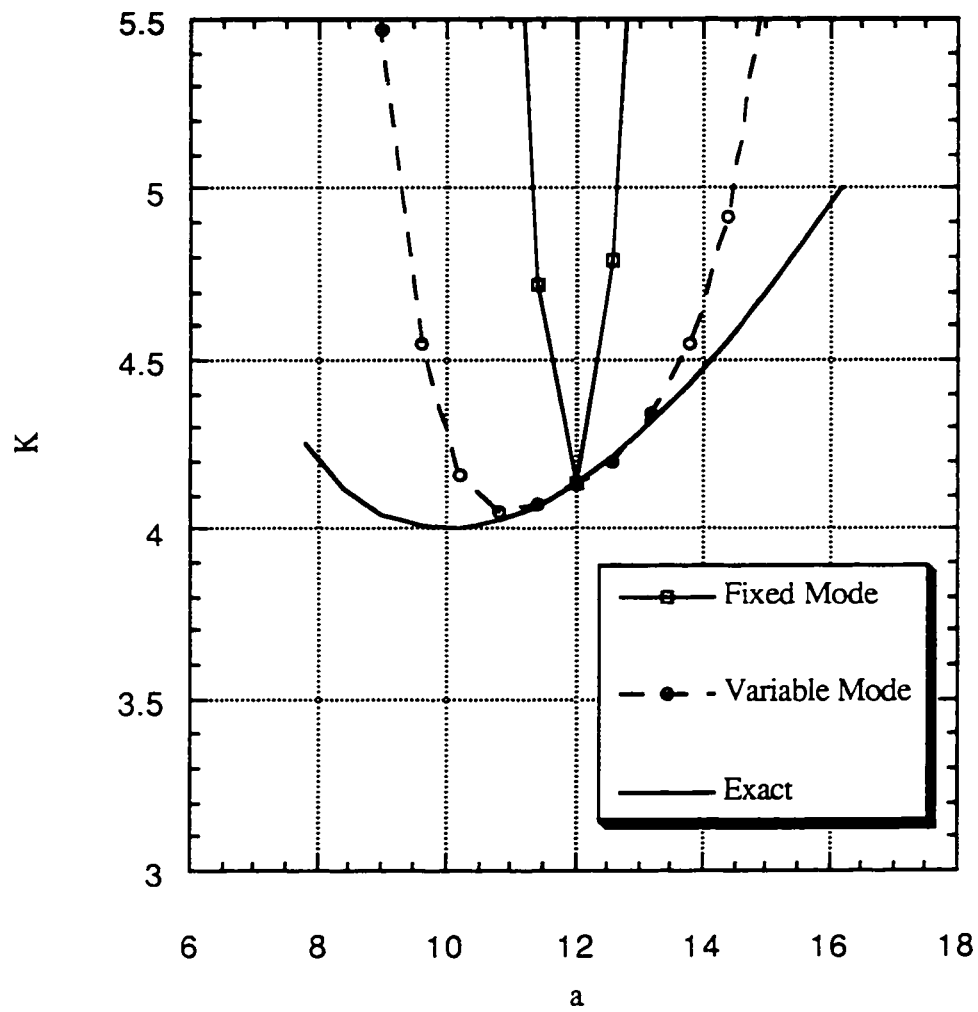


Figure 8.1 The buckling load coefficients from order reduction analysis for the rectangular plate.

Next, the effect of approximate system matrices on the buckling load are examined. The two mode shapes from the buckling analysis at a_0 are chosen as basis vectors and both stiffness and geometric stiffness matrices are approximated using their sensitivities. In Table 8.2, direct, reciprocal and two types of mixed approximation methods have been used to construct system matrices at modified design variable. Direct approximation for stiffness matrix and the reciprocal for geometric stiffness matrix have been used in (LR). In (RL) the geometric stiffness matrix is approximated by direct Taylor series while the stiffness is approximated by reciprocal Taylor series. It is interesting to note that the reduced order system matrices are nearly diagonal in all four approximation methods so that the buckling loads obtained from Rayleigh quotient are identical to the loads obtained from reduced system up to 4 significant digits. It can be explained by the fact that the eigenvectors are orthogonal with respect to the system matrices at reference design variable a_0 and when basis vectors are selected from these eigenvectors, this orthogonality still remains even though system matrices has been changed with the change of design variable. It was confirmed by examining the eigenvectors of reduced system which are composed of one dominant component in magnitude and other components which are as small as 0.1% of the dominant one. If we recall the theoretical results of rectangular plate buckling under uniaxial compression shown in Eq. (7.3), the mode shape changes in a discrete manner as the length of the plate changes so that the contributions of higher modes are small in determining the first mode of elongated plate as long as the critical mode ($m = 1, n = 1$, in this example) isn't changed. In the discussion which follows, the results from the reduced order system are assumed to be identical to those from Rayleigh quotient approximation since both gave identical buckling loads up to 4 significant digits.

When the direct approximation is used for the stiffness matrix, the false mode switches have been detected as a is increased by more than 20% of a_0 and the buckling load are

underestimated than the one obtained using reciprocal approximation of stiffness. This contradicts the prediction of RQA(CAN93) that the reciprocal approximation will result in more conservative estimate of buckling load in sizing design variable case . It can be seen in Figure 8.2 that the mixed method (RL), which is identical to RQA in this example, even overestimated the buckling loads when a is increased. It was found during the calculation that this overestimation is caused by the negative value of $\frac{\partial V}{\partial a}$ which is always positive when sizing design variable is considered. As a result, the linear modal strain energy V is overestimated when reciprocal approximation is used than when it is approximated directly. As it was expected, the lowest estimate of buckling load was obtained from the proposed CRQA(Conservative Rayleigh Quotient Approximation) ,which is identical to the result from mixed method (LR) in this case and it always underestimated the buckling load relative to the exact one.

Table 8.2 Comparison of buckling load from order reduction with first order approximations of system matrices for the rectangular plates (Fixed mode method).

Design variable	Direct	Reciprocal	Mixed (LR)	Mixed (RL)	Exact
7.8	3.7476	3.6124	3.2885	4.1167	4.2521
8.4	3.7900	3.6869	3.4489	4.0515	4.1228
9.0	3.8358	3.7614	3.5961	4.0121	4.0446
9.6	3.8855	3.8358	3.7301	3.9957	4.0067
10.2	3.9394	3.9103	3.8508	4.0003	4.0016
10.8	3.9983	3.9848	3.9583	4.0250	4.0237
11.4	4.0628	4.0592	4.0526	4.0694	4.0690
12.0	4.134	4.134	4.134	4.134	4.134
12.6	4.2120	4.2081	4.2016	4.2187	4.2174
13.2	4.2991	4.2826	4.2562	4.3259	4.3163
13.8	4.3965	4.3571	4.2976	4.4574	4.4295
14.4	4.5060	4.4316	4.3258	4.6162	4.5559
15.0	4.6302*	4.5060	4.3408*	4.8065	4.6944
15.6	4.7720*	4.5805	4.3425*	5.0335	4.8445
16.2	4.9357*	4.6550*	4.3311*	5.3048*	5.0054

* incorrect mode shape

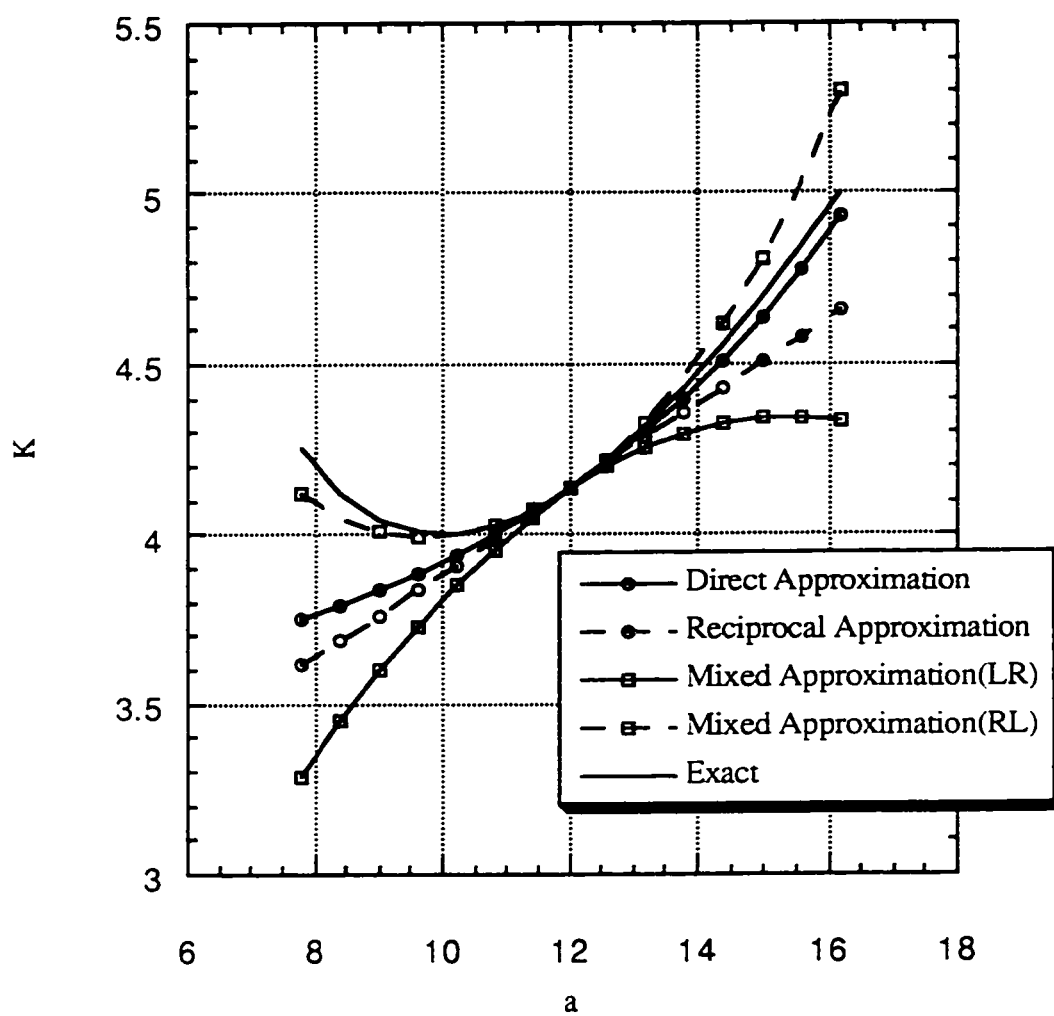


Figure 8.2 The buckling load coefficients from order reduction analysis with first order approximation of system matrices for the rectangular plate.

8.2 Typical Fighter Wing

The wing of typical fighter in Chapter 7 has been reexamined to see the effect of the order reduction on the buckling analysis of this complex structure. The same finite element mesh of Figure 7.38 has been used and during the modification of the shape design variable α , which is the sweep angle of the leading edge spar. The same aerodynamic load (9G pull-up) was applied in the finite element model. The buckling mode shapes and their sensitivities are obtained at the reference design variable $\alpha_0 = 35.125$ by solving full order analysis with 2457 degrees of freedom.

Since the buckling load for the lowest three modes are close to each other, the mode shapes for the three lowest modes shown in Figures 7.47 - 7.49 are chosen as basis vectors in the following order reduction analysis. Table 8.3 shows the numerical results for the first mode obtained from reduced system matrices when the system matrices are calculated exactly at modified design variable and those are compared with the result from full order buckling analysis. The exact solutions obtained from full order analysis show that mode switch between first and second modes occurred when α is changed from 41.125 to 43.125 degree. The three mode shapes obtained from fixed mode method showed false modeswitchs when the amount of α decreased or increased is larger than 4 degrees. Also it is found that the predicted buckling loads within these allowable limits are all higher than the ones obtained from the variable mode methods and also higher than exact ones as shown in Figure 8.3. However, the results obtained from variable mode method showed very good agreement for the all variations of α considered. Mode switch predicted at full order analysis was exactly captured and both the buckling loads and sensitivities obtained from reduced system also showed good agreement with full order analysis results. From accuracy point of view, variable mode method is more desirable than fixed mode method

but it requires the additional decomposition of full order matrix $[B]$ in Eq. (5.33) to calculate mode shape sensitivities.

The buckling loads are presented in Table 8.4 when the system matrices are approximated using sensitivity results at the reference design variable and the three mode shapes are selected as basis vectors. In all approximation cases, the mode switches expected at $\alpha = 43.125$ are not captured and it is found that the resulting reduced system matrices are nearly diagonal so that the solutions obtained from reduced system matrices are almost identical to the ones from Rayleigh quotient method, which is similar to the former example. Again, the numerical results in Table 8.4 are assumed to be obtained from Rayleigh quotient method in the following. The sensitivity results at the reference variable show that the sensitivity of linear modal strain energy is negative and the sensitivity of geometric modal strain energy is positive. In this case, the CRQA is identical to the linear approximations of system matrices. As shown in Figure 8.4, the smoothed buckling loads are predicted as α changes between 27.125 and 41.125 degrees although the buckling results from full order analysis has an oscillatory behavior with respect to α . The buckling loads predicted by CRQA are all lower than any other results as it was expected.

Table 8.3 Comparison of buckling load and sensitivity from order reduction for the wing

Design variable	Fixed Mode $\lambda \left(\frac{\partial \lambda}{\partial a} \times 10^{-2} \right)$	Variable Mode $\lambda \left(\frac{\partial \lambda}{\partial a} \times 10^{-2} \right)$	Exact $\lambda \left(\frac{\partial \lambda}{\partial a} \times 10^{-2} \right)$
27.125	1.0725(-1.767)*	0.9665(-0.864)	0.9584(-0.526)
29.125	1.0664(-1.627)*	0.9488(-0.759)	0.9457(-0.586)
31.125	0.9952(-3.316)	0.9412(-0.675)	0.9407(-0.625)
33.125	0.9306(-1.934)	0.9178(-0.594)	0.9176(-0.586)
35.125	0.9180(-0.455)	0.9180(-0.455)	0.9180(-0.455)
37.125	0.9169(1.538)	0.8991(-0.229)	0.8989(-0.243)
39.125	0.9639(-0.212)	0.9041(0.276)	0.9028(0.156)
41.125	0.9481(0.107)*	0.9196(1.231)	0.9127(0.731)
43.125	0.9547(0.605)*	0.9112(-0.309)	0.9037(-0.714)

* incorrect mode shape

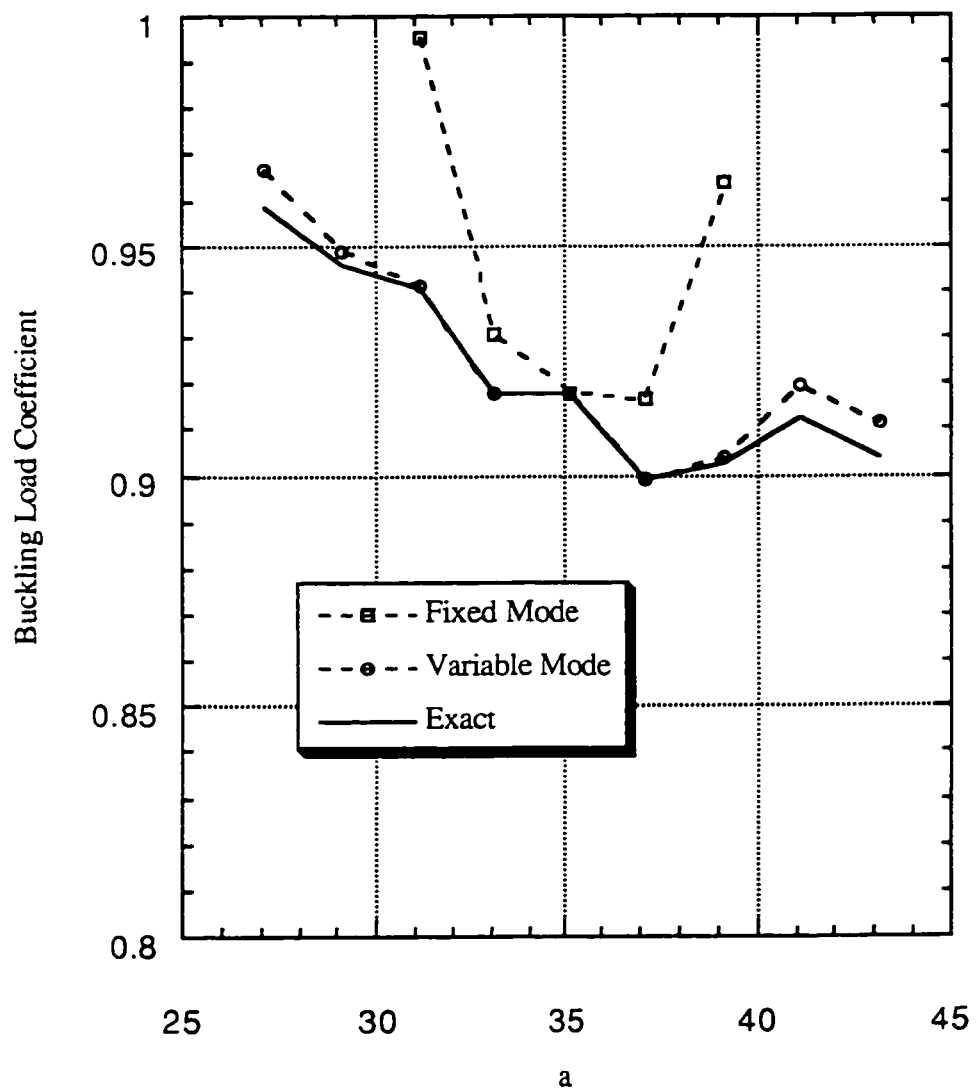


Figure 8.3 The buckling load coefficients from order reduction analysis for the wing.

Table 8.4 Comparison of Buckling Load from order reduction with first order approximations of system matrices for the wing (Fixed mode method).

Design variable	Direct	Reciprocal	Mixed (LR)	Mixed (RL)	Exact
27.125	0.9550	0.9662	0.9598	0.9614	0.9584
29.125	0.9457	0.9514	0.9481	0.9490	0.9457
31.125	0.9364	0.9387	0.9374	0.9377	0.9407
33.125	0.9271	0.9277	0.9274	0.9275	0.9176
37.125	0.9089	0.9094	0.9091	0.9092	0.8989
39.125	0.9000	0.9018	0.9001	0.9010	0.9028
41.125	0.8910	0.8949	0.8926	0.8933	0.9127
43.125	0.8822*	0.8887*	0.8849*	0.8861*	0.9037

* incorrect mode shape

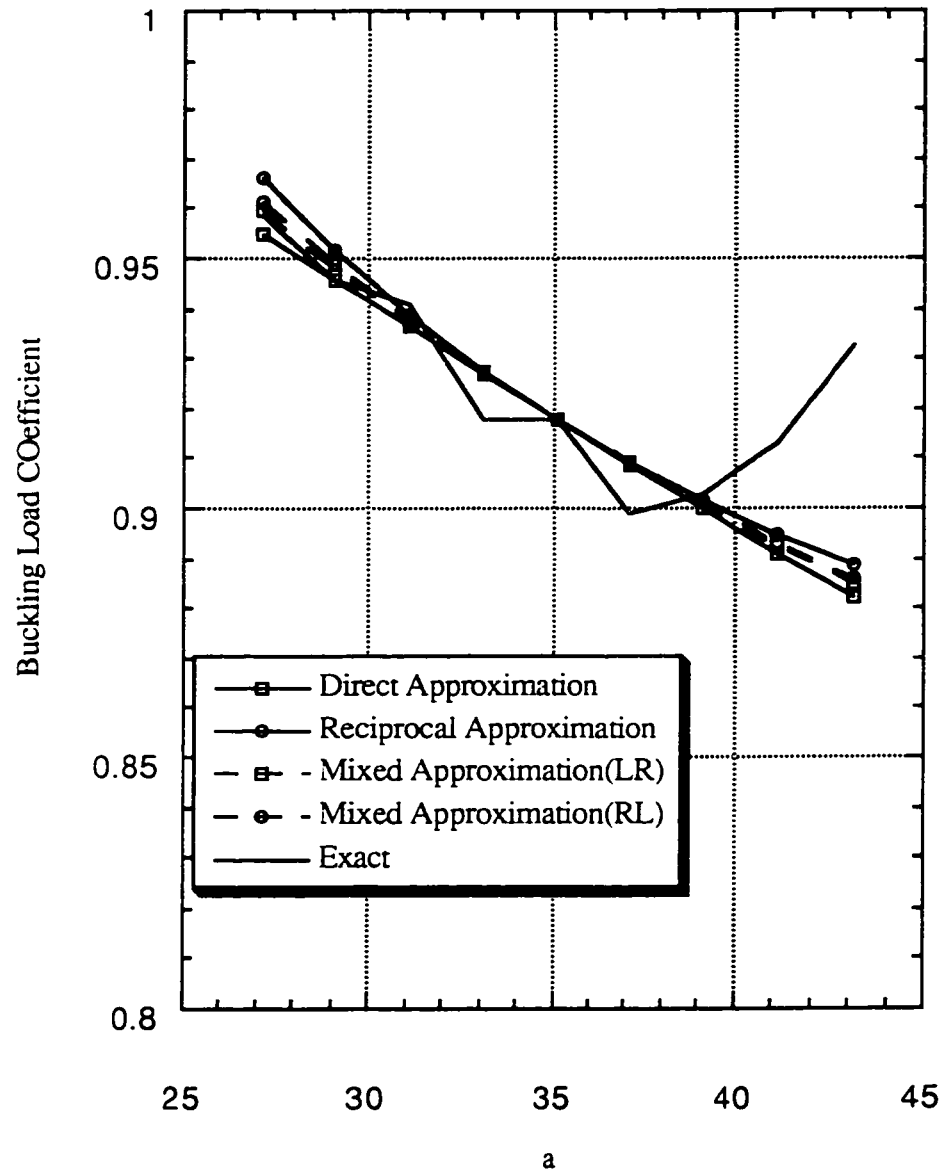


Figure 8.4 The buckling load coefficients from order reduction analysis with first order approximation for system matrices of the wing.

Chapter 9

Conclusions

The mathematical formulation of the flat triangular DKL/LST shell element was modified and adapted in order to obtain explicit closed form expressions for the element stiffness and geometric stiffness matrices in terms of sizing, material and shape design variables. Automated symbolic derivation and closed form expressions for area integrals were used in the formulations. The resulting equations were used to derive explicit expressions for the analytic sensitivities of stiffness and geometric stiffness matrices with respect to shape design variables. With analytic shape sensitivities of system matrices and corresponding buckling loads at hand, the resulting new computer capability makes it possible to construct buckling constraint approximations for Approximation-Concept based structural optimization. The simplicity of the shell elements used and the elimination of the need to carry out numerical integration, lead to computational savings, especially when repetitive analyses have to be carried out during shape design optimization of typical airframes. The new capability can capture both local and global modes of buckling failure with the same finite element model. Sub-component interaction during buckling can, thus, be taken into account during the shape optimization of wing and fuselage structures. In the results presented in this study and in the work supporting it, accuracy of the buckling predictions as well as accuracy of the analytic sensitivities were demonstrated. Low level numerical noise, leading to non-smooth buckling predictions when shape design variables were changed was detected, and found to be caused by non-smoothness of element in-plane stresses. While

the stiffness matrix and deformation static solutions were found to be smooth, the non-smooth stresses led to non-smooth geometric stiffness matrix, and, hence, to non-smooth buckling eigenvalues. At the same time, the analytic shape sensitivities were found to be always accurate, leading to an efficient and reliable design oriented structural modeling capability.

The availability of reliable sensitivity information for the buckling eigenvalues makes it possible to construct direct, reciprocal or hybrid (conservative) approximations of these eigenvalues (to be used with Approximation Concepts based Structural Optimization). In addition to those, alternative order reduction techniques were studied, including fixed-mode and variable-mode methods with different Taylor series approximations for the stiffness and geometric stiffness matrices, as well as Rayleigh Quotient approximations. When small move limits are used limiting the design to stay close to the base (reference) design, all these approximations lead to good accuracy of buckling load prediction. When the move limits are allowed to be large, a variable-mode approach in the case of a fighter wing box lead to better accuracy when the exact K and KG matrices are used. When system matrices were approximated using various combinations of direct and reciprocal or hybrid Taylor series, no single candidate emerged as considerably more accurate than the others. The subject of order reduction and approximations in large scale buckling calculations is still in need of more research.

Subjects for further study and extensions of this work include application of analytical shape sensitivity to mesh adaptation; order reduction and computational speed-up of buckling predictions for large scale built-up structures, application of the present technology to stiffened panel design optimization; addition of mass matrix computation and

structural dynamic effects; and development of a design oriented nonlinear structural analysis technique for sizing, material and shape optimization.

BIBLIOGRAPHY

(AH86) Adelman, H.M., and Haftka, R.T., "Sensitivity Analysis of Discrete Structural Systems", *AIAA Journal*, Vol. 24, No.5, pp. 823-832, 1986.

(AHA92) Ausman, J.D., Hangen, J.A., and Acevedo, D.A., "Application of a Local Panel Buckling Constraint within Automated Multidisciplinary Structural Analysis and Design", AIAA 92-1116, 1992 Aerospace Design Conference, February 3-6, 1992, Irvine, CA.

(ALL84) Allman, D.J., "A Compatible Triangular Element Including Vertex Rotations For Plane Elasticity Analysis", *Computers and Structures*, Vol. 19, pp. 1-8, 1984.

(AR86) Antona, E., and Romeo, G., "Analytical and Experimental Investigation on Advanced Composite Wing Box Structures in Bending Including Effects of Initial Imperfections and Crushing Pressure", ICAS-86-4.2.3, 15th Congress of the International Council of the Aeronautical Sciences, London, England, September 1986, pp. 255-261.

(ARO95) Arora, J.S., "Structural Design Sensitivity Analysis: Continuum and Discrete Approaches", *Advances in Structural Optimization*, edited by Herskovits, J., Kluwer Academic Publishers, Dordrecht, 1995.

(BB86) Bennet, J.A., and Botkin, M.E., *The Optimum Shape*, Plenum Press, New York, 1986.

(BBH80) Batoz, J.L., Bathe, K.J. and Ho, J.W., "A Study of Three node Triangular Plate Bending Elements", *International Journal for Numerical Methods in Engineering*, Vol. 15, pp. 1771-1812., 1980.

(BCH88) Barthelemy, B., Chon, C.T., and Haftka, R.T., "Accuracy Problems Associated With Semi-Analytical Derivatives of Static Response", *Finite Elements in Analysis and Design*, Vol. 4, pp. 249-265, 1988.

(BH81) Bathe, K.J. and Ho, J.W., "A Simple and Effective Element for Analysis of General Shell Structures", *Computers and Structures*, Vol. 13., pp. 673-681, 1981

(BHW94) Bartholomew, P., Harris, J., and Wellen, H., "The Integration of Local Design of Composite Panels into Overall Structural Design", *AIAA Paper 94-4354*, 1994.

(BL88) Brockman, R.A., "Sensitivity Analysis with Plates and Shell Finite Elements", *International Journal for Numerical Methods in Engineering*, Vol. 26, pp. 1129-1143, 1988.

(BOT81) Botkin, M.E., "Shape Optimization of Plate and Shell Structures", *AIAA Journal*, Vol. 20, No. 2, pp. 268-273, 1982.

(BOT94) Botkin, M.E., "Shape Optimization With Buckling and Stress Constraints", *AIAA Journal*, Vol. 34, No. 2, pp. 423-425, 1994.

(BRO87) Brockman, R.A., "Geometric Sensitivity Analysis with Isoparametric Finite Elements", *Communications in Applied Numerical Methods*, Vol. 3, pp. 495-499, 1987.

(BRU75) Bruhn, E.F., *Analysis and Design of Flight Vehicle Structures*, Tri State Offset Company, 1973, Chapter C5.

(CAN90) Canfield, R.A., "High Quality Approximation of Eigenvalues in Structural Optimization", *AIAA Journal*, Vol. 28, No. 6., June 1990, pp. 1116-1122.

(CAN93) Canfield, R.A., "Design of Frames Against Buckling Using a Rayleigh Quotient Approximation", *AIAA Journal*, Vol. 31, No. 6, June 1993, pp. 1143-1149.

(CGZ89) Cheng, G., Gu, Y., and Zhou, Y., "Accuracy of Semi-Analytic Sensitivity Analysis", *Finite Elements in Analysis and Design*, Vol. 6, pp. 113-128, 1989.

(CH83) Choi, K.K., and Haug, E.J., "Shape Design Sensitivity Analysis of Elastic Structures", *Journal of Structural Mechanics*, Vol. 11, No. 2, pp. 231-269, 1983.

(CHA) Chamis, C.C., "Buckling of Anisotropic Composite Plates", *Proceedings of the American Society of Civil Engineers, journal of the Structural Division*, Oct., pp. 2119-2139, 1969.

(CHE92) Chen, H.C., "Evaluation of Allman Triangular Membrane Element Used in General Shell Analysis", *Computers and Structures*, Vol. 43, pp. 881-887, 1992.

(CMP89) Cook, Robert D. ; Malkus, Davis S. ; Plesha, Michael E. , *Concepts and Applications of Finite Element Analysis*, 3rd Ed., Wiley, 1989

(CTZY90) Chang, T.Y., Tanh, H.Q., Zheng, D. and Yuan, M.W., "Application of Symbolic Method to Hybrid/Mixed Finite Elements and Computer Implementation", *Computers and Structures*, Vol. 35, No. 4, pp. 293-299, 1990.

(DI86) Ding, Y., "Shape Optimization a Literature Survey", *Computers and Structures*, Vol. 24, pp. 985-1004, 1986.

(DMM86) Dhatt, G., Marcotte, L. and Matte, Y., "A New Triangular Discrete Kirchhoff Plate/Shell Element", *International Journal for Numerical Methods in Engineering*, Vol. 23, pp. 453-470, 1986.

(EKE92) Ertas, A., Krafcik, J.T., and Ekwaro-Osire, S., "Performance of an Anisotropic Allman/DKT 3-node Thin Triangular Flat Shell Element", *Composites Engineering*, Vol.2, pp. 269-280, 1992.

(ESH92) Eschenauer, H.A., Schuhmacher, G., and Hartzheim, W., "Multidisciplinary Design of Composite Aircraft Structures by Lagrange", *Computers&Structures*, Vol. 44, No. 4, pp. 877-893, 1992.

(EVA93) Eldred, M.S., Venkayya, V.B., and Anderson, W.J., "Mode Tracking Issues in Optimization", AIAA-93-1416-CP, 1993.

(FDB89) Farad, M., Dhatt, G. and Batoz, J.L., "A New Discrete Kirchhoff Plate/Shell Element with Updated Procedures", *Computers and Structures*, Vol. 31, No. 4, pp. 591-606, 1989

(FM71) Fox, R.L., and Miura, H., "An Approximate Analysis Technique for Design Calculation", *AIAA Journal*, Vol. 9, No. 1, 1971.

(GR91) Gilewski, W., Radwanska, M., "A survey of finite element models for the analysis of moderately thick shells", *Finite Elements in Analysis and Design*, Vol.9, pp. 1-21, 1991

(HA93) Harvey, M.S., "Automated Finite Element Modeling of Wing Structures for Shape Optimization", M.Sc. thesis, Department of Aeronautics and Astronautics, University of Washington, Seattle, Washington, 1993.

(HCK86) Haug, E.J., Choi, K.K., and Komkov, V., *Design Sensitivity Analysis of Structural Systems*, Academic Press, New York, 1986.

(HGK90) Haftka, R.T., Gurdal, Z., and Kamat, M.P., *Elements of Structural Optimization*, 2nd Ed., Kluwer Academic Publishers, 1990.

(HG86) Haftka, R.T., and Grandhi, R.V., "Structural Shape Optimizations-A Survey", *Computer Method in Applied Mechanics and Engineering*, Vol. 57, pp.91-106, 1986.

(HG91) Haftka, R.T., and Gurdal, Z., *Elements of Structural Optimization*, 3rd Edition, Kluwer Academic Publishers, Dordrecht, Boston, London 1991.

(HMR90) Hornung, G., Mathias, D.W., and Rohle, H., "optimization of Wing Type Structures including Stress and Buckling Constraints", presented at the Third Air Force / NASA Symposium on Recent Advances in Multidisciplinary Analysis and Optimization September 24 - 26, 1990, San Francisco, CA

(JK85) Jeyachandrabose, C., and Kirkhope, J., "Explicit Formulation for a high Precision triangular Laminated Anisotropic Thin Plate Finite Element", *Computers and Structures*, Vol. 20, No. 6, pp. 991-1007, 1985.

(JKA95) Jaunky, N., Knight, N.F., and Ambur, D.R., "Buckling of Arbitrary Quadrilateral Anisotropic Plates", *AIAA Journal*, Vol. 33, No. 5, pp. 938-944, 1995.

(JON75) Jones, R.M., *Mechanics of Composite Materials*, McGraw-Hill Book Company, New York, 1975.

(KF79) Korncoff, A.R., and Fenves, S.J., "Symbolic Generation of Finite Element Stiffness Matrices", *Computers and Structures*, Vol. 10, pp. 119-124, 1979.

(KP78) Kennedy, J.B., and Prabhakara, M.K., "Buckling of Simply Supported Orthotropic Skew Plates", *Aeronautical Journal*, Vol. 29, pp. 161-174, 1978.

(KRP95) Krishna Reddy, A.R., and Palaninathan, R., "Buckling of Laminated Skew Plates", *Thin-Walled Structures*, Vol. 22, pp. 241-259, 1995.

(KXWL93) Kitipornchai, S., Xiang, Y., Wang, C.M., and Liew, K.M., "Buckling of Thich Skew Plates", *International Journal for Numerical Methods in Engineering*, Vol. 36, pp. 1299-1310, 1993.

(LIV94) Livne, E., "Analytic Sensitivities for Shape Optimization in Equivalent Plate Structural Wing Model", *Journal of Aircraft*, Vol. 31, pp. 961-969, 1994.

(LL97) Langelaan, J.W., and Livne, E., "Analytic Sensitivities and Design Oriented Structural Analysis for Airplane Fuselage Shape Synthesis", *Computers and Structures*, Vol. 62, No. 3, pp. 505-519, 1997.

(LM95) Livne, E., and Milosavljevic, R., "Analytic Sensitivity and Approximation of Skin Buckling Constraints in Wing-Shape Synthesis", *Journal of Aircraft*, Vol. 32, No. 5, pp. 1102-1113, 1995.

(LP87) Lecina, G., and Petiau, C., "Advances in Optimal Design with Composite Materials", in *Computer Aided Optimal Design: Structural and Mechanical Systems*, C.A. Mota Soares, editor, Springer Verlag, Berlin, 1987, pp. 943-953.

(LT95) Liu, M.L., and To, W.S., "Vibration of Structures By Hybrid Strain-Based Three-Node Flat Triangular Shell Elements", *Journal of Sound and Vibration*, Vol. 184, No. 5, pp. 801-821, 1995.

(MC83) McCullers, L.A., "Automated Design of Advanced Composite Structures", in *Mechanics of Composite Materials*, Zvi Hashin, editor, Pergamon Press, 1983, pp. 119-133.

(MK85) Meek, J.L. and Tan, H.S. "A Discrete Kirchhoff Plate Bending Element with Loof Nodes", *Computers and Structures*, Vol. 21, No. 6, pp.1197-1212, 1985.

(MK86a) Meek, J.L. and Tan, H.S. "A Faceted Shell Element with Loof Nodes", *International Journal for Numerical Methods in Engineering*, Vol. 23, pp. 49-67, 1986.

(MK86b) Meek, J.L. and Tan, H.S. "Instability Analysis of Thin Plates and Arbitrary Shells Using A Faceted Shell Element with Loof Nodes", *Computed Methods in Applied Mechanics and Engineering*, Vol. 57, pp. 143-170, 1986.

(MKN80) Mizusawa, T., Kajita, T., and Naruko, M., "Analysis of Skew Plate Problems with Various Constraints", *Journal of Sound and Vibration*, Vol. 73, No. 4, pp. 575-584, 1980.

(NA79) Noor, A.K., and Andersen, C.M., "Computerized Symbolic Manipulation in Structural Mechanics-Progress and Potential", *Computers and Structures*, Vol. 10, pp. 95-118, 1979.

(NEL76) Nelson, R.B., "Simplified Calculation of Eigenvector Derivatives", *AIAA Journal*, Vol. 14, No. 9, pp.1201-1205, 1976.

(NOO81) Noor, A.K., "Recent Advances in Reduction Methods for Nonlinear Problems", *Computers and Structure*, Vol. 13, pp. 31-44, 1981.

(RG93) Ragon, S.A., and Gurdal, Z., "Effects of Geometric Nonlinearities on the Response of Optimized Box Beam Structures", *AIAA Paper 93-1412*, 34th AIAA/ASME/ASCE/AHS/ASC Structures, Structural Dynamics and Materials Conference, April 1993, La Jolla, CA.

(RGS94) Ragon, S.A., Gurdal, Z.,and Starnes, J.H.,Jr., "Optimization of Composite Box-Beam Structures Including the Effects of Subcomponent Interaction", *Proceedings of the AIAA/ASME/ASCE/AHS/ASC 35th Structures, Structural Dynamics, and Materials Conference(Hilton Head, SC)*, AIAA, Washington, DC, pp. 818-828, 1994.(AIAA Paper 94-1410)

(SCH81) Schmit, L.A., "Structural Synthesis - Its Genesis and Development", *AIAA Journal*, Vol. 19, October 1981, pp. 1249-1263.

(SC86) Stolarski, H.K., and Carpenter, N.J., "An Alternative Formulation of the Geimetric Stiffness Matrix for Plate Elements", *Computers and Structurea*, Vol. 24, No. 6, pp. 935-940, 1986.

(SH79) Starnes, J. H., Jr., and Haftka, R. T., "Preliminary Design of Composite Wings for Buckling, Stress and Displacement Constraints", *Journal of Aircraft*, Vol 16, pp. 564-570, 1979.

(SK92) Singhvi, S., and Kapania, R.K., "Analytical Shape Sensitivities and Approximations of Modal Response of Generally Laminated Tapered Skew Plates", AIAA 92-2391, Proceedings of the 33th AIAA/ASME/ASCE/AHS/ASC Structures, Structural Dynamics and Materials Conference, Dallas, Texas, April 1992.

(SM82) Schmit, L.A., and Mehrinfar, M., "Multilevel Optimum Design of Structures with Fiber-Composite Stiffened-Panel Components", AIAA Journal, Vol. 20, No. 1, pp. 138-147, 1982.

(SR78) Schmit, L.A., and Ramanathan, R.K., "Multilevel Approach to Minimum Weight Design including Buckling Constraints", AIAA Journal, Vol. 16, No. 2, February 1978, pp. 97-104.

(TD87) Talbot, M., and Dhatt, G., "Three Discrete Kirchhoff Elements for Shell Analysis with Large Geometrical Non-linearities and Bifurcation", Engineering Computation, Vol. 4, pp.15-22, 1987

(TG61) Timoshenko, S.P., and Gere, J.M., *Theory of Elastic Stability*, McGraw-Hill Book Company, New York, 1961.

(W91) Wolfram, S., *Mathematica, a System for Doing Mathematics by Computer*, Addison Wesley, second edition 1991.

(WBNL92) Wang, B.P., BABU, D., Nambiar, R.V., and Lawrence, K.L., "Shape Design Sensitivity Analysis Using Closed-Form Stiffness Matrix For Hierarchic triangular Element", Computers and Structures, Vol. 43, No. 1, pp. 69-75, 1992.

(WHI87) Whitney, J.M., *Structural Analysis of Laminated Anisotropic Plates*, Technomic Publishing Company, Lancaster, PA, 1987.

(WTT53) Wittrick, W.H., "Buckling of Oblique Plates with Clamped edges under Uniform Compression", Aeronautical Journal, Vol. 4, pp. 151-163, 1953.

(WLA92) Wang, C.M., Liew, K.M., and Alwis, A.M., "Buckling of Skew Plates and Corner Condition for Simply Supported Edges", J. Eng. Mech. ASCE, Vol. 118, pp. 651-662, 1992.

(WSG85) Wang, S., Sun, Y., and Gallagher, R.H., "Sensitivity Analysis in Shape Optimization of Continuum Structures", Computers and Structures, Vol. 20, No. 5, pp. 855-867, 1985.

(YB86) Yang, R.J., and Botkin, M.E., "Comparison between the Variational and Implicit Differentiation Approaches to Shape Design Sensitivities", AIAA Journal, Vol. 24, No. 6, pp. 1027-1032, 1986.

(YSL90) Yang, H.T.Y., Saigal, S., and Liaw, D.G., "Advances of thin shell elements and some applications-version I", Computers and Structures, Vol.35, No.4, pp.481-504, 1990.

(ZT91) Zienkiewicz, O. C. , Taylor, R. L. , *The Finite Element Method*, 4th Ed., vol. 2, McGraw-Hill, 1991

Appendix A

Explicit Expressions for $[A]$, $[C_x]$ and $[C_y]$

In this appendix, matrices $[A]$ in Eq.(3.14) , $[C_x]$ and $[C_y]$ in Eq.(3.20) are presented following the reference (MT86). Matrix $[A]$ is obtained by substituting the area coordinates of six Loof nodes and center node, shown in Figure 3.1, to Eq.(3.13) in the following way.

$$[A] = \begin{bmatrix} 1 & \alpha_1 & \alpha_2 & \alpha_1^2 & \alpha_1\alpha_2 & \alpha_2^2 & (2\alpha_1^3 + 3\alpha_1^2\alpha_2 - 3\alpha_2^2\alpha_1 - 2\alpha_2^3) \\ 1 & \alpha_2 & \alpha_1 & \alpha_2^2 & \alpha_1\alpha_2 & \alpha_1^2 & (2\alpha_2^3 + 3\alpha_2^2\alpha_1 - 3\alpha_1^2\alpha_2 - 2\alpha_1^3) \\ 1 & 0 & \alpha_1 & 0 & 0 & \alpha_1^2 & -2\alpha_1^3 \\ 1 & 0 & \alpha_2 & 0 & 0 & \alpha_2^2 & -2\alpha_2^3 \\ 1 & \alpha_2 & 0 & \alpha_2^2 & 0 & 0 & 2\alpha_2^3 \\ 1 & \alpha_1 & 0 & \alpha_1^2 & 0 & 0 & 2\alpha_1^3 \\ 1 & \alpha_3 & \alpha_3 & \alpha_3^2 & \alpha_3^2 & \alpha_3^2 & 0 \end{bmatrix} \quad (A.1)$$

where

$$\alpha_1 = \frac{1}{2} + \frac{1}{2\sqrt{3}} \quad \alpha_2 = \frac{1}{2} - \frac{1}{2\sqrt{3}} \quad \alpha_3 = \frac{1}{3} \quad (A.2)$$

Following Ref. (MT86), $[C_x]$ and $[C_y]$ are presented using nodal locations in the local coordinate system. By attaching node 1 to the origin of local coordinate system (Figure 3.5), the geometry of triangular element can be determined by only three non-zero nodal

locations, x_2 , x_3 and y_3 as shown in Figure A.1. Thus both matrices are expressed in terms of the three non-zero nodal locations.

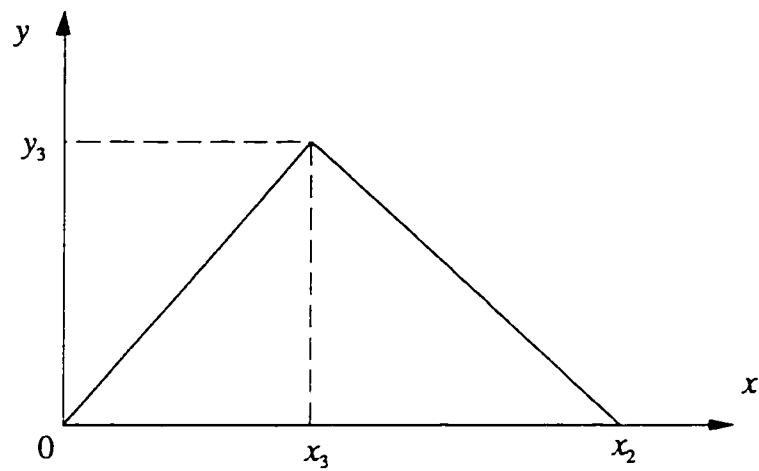


Figure A.1 Area Coordinate

$$[C_2] = \begin{bmatrix}
 \frac{x_2}{c_1 l_{12}^2} & \frac{x_2}{c_2 l_{12}^2} & 0 & -\frac{x_2}{c_3 l_{12}^2} & 0 & 0 & 0 & 0 & 0 & 0 & 0 & 0 & 0 \\
 -\frac{x_2}{c_2 l_{12}^2} & -\frac{x_2}{c_1 l_{12}^2} & 0 & \frac{x_2}{c_3 l_{12}^2} & 0 & 0 & 0 & 0 & 0 & 0 & 0 & 0 & 0 \\
 0 & -\frac{x_2 - x_3}{c_1 l_{23}^2} & -\frac{x_2 - x_3}{c_2 l_{23}^2} & 0 & \frac{x_2 - x_3}{c_3 l_{23}^2} & 0 & 0 & 0 & \frac{y_3}{l_{23}} & 0 & 0 & 0 & 0 \\
 0 & \frac{x_2 - x_3}{c_2 l_{23}^2} & \frac{x_2 - x_3}{c_1 l_{23}^2} & 0 & 0 & 0 & 0 & 0 & 0 & \frac{y_3}{l_{23}} & 0 & 0 & 0 \\
 -\frac{x_3}{c_2 l_{13}^2} & 0 & 0 & 0 & 0 & 0 & \frac{x_3}{c_3 l_{13}^2} & 0 & 0 & 0 & -\frac{y_3}{l_{13}} & 0 & 0 \\
 \frac{x_3}{c_1 l_{13}^2} & 0 & 0 & 0 & 0 & 0 & -\frac{x_3}{c_3 l_{13}^2} & 0 & 0 & 0 & 0 & 0 & -\frac{y_3}{l_{13}} \\
 a_1 & a_2 & a_3 & 0 & -\frac{2y_3}{c_4 Det} & \frac{2y_3}{c_4 Det} & \frac{2y_3}{c_4 Det} & 0 & 0 & -\frac{y_3}{c_5 l_{23}} & -\frac{y_3}{c_5 l_{23}} & \frac{y_3}{c_5 l_{13}} & \frac{y_3}{c_5 l_{13}}
 \end{bmatrix}$$

(A.3)

$$\begin{aligned}
[C_y] = & \begin{bmatrix}
0 & 0 & 0 & 0 & 0 & 0 & \frac{x_2}{l_{12}} & 0 & 0 & 0 & 0 & 0 \\
0 & 0 & 0 & 0 & 0 & 0 & 0 & \frac{x_2}{l_{12}} & 0 & 0 & 0 & 0 \\
0 & -c_1 \frac{y_3}{l_{23}^2} & -c_2 \frac{y_3}{l_{23}^2} & 0 & c_3 \frac{y_3}{l_{23}^2} & 0 & 0 & 0 & 0 & -\frac{x_2 - x_3}{l_{23}} & 0 & 0 \\
0 & c_2 \frac{y_3}{l_{23}^2} & c_1 \frac{y_3}{l_{23}^2} & 0 & -c_3 \frac{y_3}{l_{23}^2} & 0 & 0 & 0 & 0 & -\frac{x_2 - x_3}{l_{23}} & 0 & 0 \\
c_2 \frac{y_3}{l_{13}^2} & 0 & 0 & 0 & 0 & -c_3 \frac{y_3}{l_{13}^2} & 0 & 0 & 0 & 0 & -\frac{x_3}{l_{13}} & 0 \\
-c_1 \frac{y_3}{l_{13}^2} & 0 & -c_2 \frac{y_3}{l_{13}^2} & 0 & c_3 \frac{y_3}{l_{13}^2} & 0 & 0 & 0 & 0 & 0 & 0 & -\frac{x_3}{l_{13}} \\
a_4 & a_5 & a_6 & -c_4 \frac{2x_2}{Det} & c_4 \frac{2(x_2 - x_3)}{Det} & c_4 \frac{2x_3}{Det} & -c_5 \frac{x_2}{l_{12}} & -c_5 \frac{x_2}{l_{12}} & c_5 \frac{x_2 - x_3}{l_{23}} & c_5 \frac{x_2 - x_3}{l_{23}} & c_5 \frac{x_3}{l_{13}} & c_5 \frac{x_3}{l_{13}}
\end{bmatrix} \quad (A.4)
\end{aligned}$$

where

$$c_1 = 2.1547004 \quad c_2 = 0.1547004 \quad c_3 = 2.3094008 \quad c_4 = 1.3333334 \quad c_5 = 0.16666667 \quad (A.5)$$

$$l_{12} = \sqrt{x_2^2} \quad l_{23} = \sqrt{(x_2 - x_3)^2 + y_3^2} \quad l_{13} = \sqrt{x_3^2 + y_3^2} \quad Det = x_2 \cdot y_3 \quad (A.6)$$

$$\begin{aligned}
a_1 &= 0.3333328 \left[\frac{-x_2}{l_{12}^2} - \frac{x_3}{l_{13}^2} + \frac{2y_3}{Det} \right] & a_2 &= 0.3333328 \left[\frac{x_2}{l_{12}^2} + \frac{x_2 - x_3}{l_{23}^2} - \frac{2y_3}{Det} \right] & a_3 &= -0.3333328 \left[\frac{x_2 - x_3}{l_{23}^2} - \frac{x_3}{l_{13}^2} \right] \\
a_4 &= -0.3333328 \left[-\frac{y_3}{l_{13}^2} + \frac{2(x_2 - x_3)}{Det} \right] & a_5 &= 0.3333328 \left[\frac{y_3}{l_{23}^2} - \frac{2x_3}{Det} \right] & a_6 &= 0.3333328 \left[\frac{-y_3}{l_{23}^2} - \frac{y_3}{l_{13}^2} + \frac{2x_2}{Det} \right]
\end{aligned} \quad (A.7)$$

Appendix B

Transformation Matrix

Explicit expression of transformation matrix (Eq.3.59) in terms of global nodal locations are presented in this appendix, followed by the derivation of the sensitivities of both transformation matrix and element nodal coordinates in local axes with respect to global nodal locations in global axes.

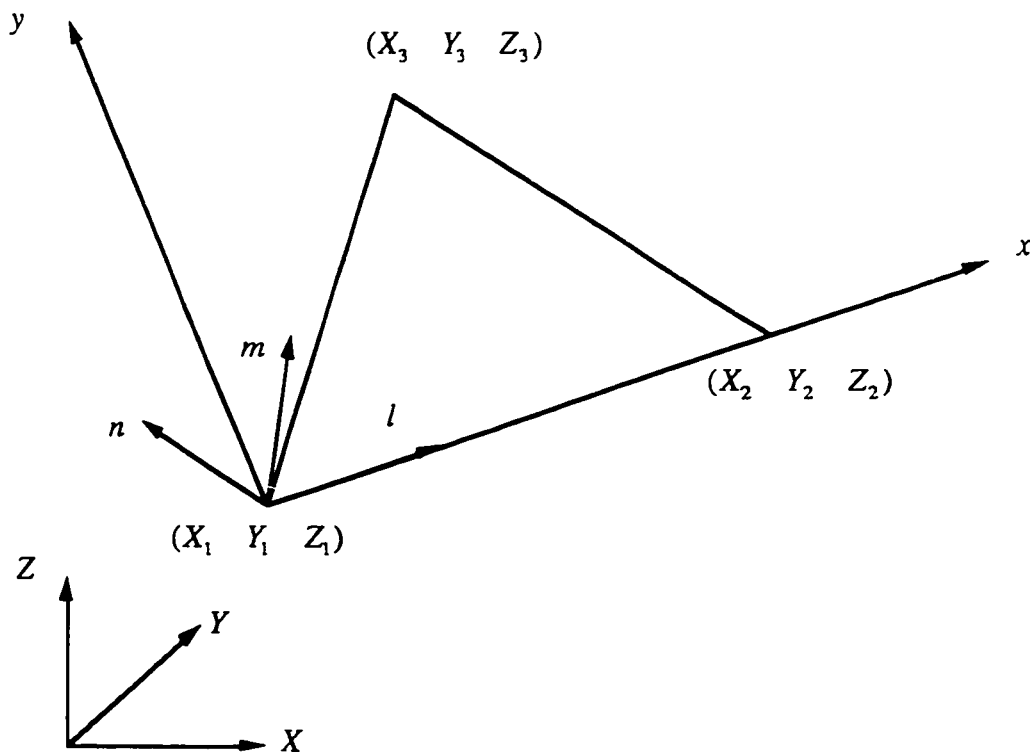


Figure B.1 Transformation from global coordinate to local coordinate system.

Local axes are attached to triangular element so that the node 1 is at the origin, the x axis passes through nodes 1 and 2, and the y axis is perpendicular to the x axis (Figure B.1). The element is in the x, y plane of the local axes. Local x, y plane of the element can be expressed in terms of nodal coordinates in global axes using two vectors, $\{H\}$ and $\{G\}$ which are defined in Eq.(3.58) as

$$\{H\} = \begin{Bmatrix} X_2 - X_1 \\ Y_2 - Y_1 \\ Z_2 - Z_1 \end{Bmatrix} \quad \{G\} = \begin{Bmatrix} X_3 - X_1 \\ Y_3 - Y_1 \\ Z_3 - Z_1 \end{Bmatrix} \quad (\text{B.1})$$

The transformation matrix consists of the three orthonormal vectors, l , m and n in Figure B.1, which are

$$\begin{aligned} \{l\} &= \frac{\{H\}}{\|\{H\}\|} = \begin{Bmatrix} c_x \\ b_x \\ a_x \end{Bmatrix} \frac{1}{\sqrt{c_x^2 + b_x^2 + a_x^2}} \\ \{n\} &= \frac{\{H\} \times \{G\}}{\|\{H\} \times \{G\}\|} = \begin{Bmatrix} c_z \\ b_z \\ a_z \end{Bmatrix} \frac{1}{\sqrt{c_z^2 + b_z^2 + a_z^2}} \\ \{m\} &= \{n\} \times \{l\} = \frac{1}{\sqrt{c_z^2 + b_z^2 + a_z^2} \sqrt{c_x^2 + b_x^2 + a_x^2}} \begin{Bmatrix} b_z a_x - a_z b_x \\ a_z c_x - c_z a_x \\ c_z b_x - c_x b_z \end{Bmatrix} \end{aligned} \quad (\text{B.2})$$

where

$$c_x = X_2 - X_1 \quad b_x = X_2 - Y_1 \quad a_x = Z_2 - Z_1 \quad (\text{B.3})$$

$$\begin{aligned} c_z &= (Y_2 - Y_1)(Z_3 - Z_1) - (Z_2 - Z_1)(Y_3 - Y_1) \\ b_z &= (Z_2 - Z_1)(X_3 - X_1) - (X_2 - X_1)(Z_3 - Z_1) \\ a_z &= (X_2 - X_1)(Y_3 - Y_1) - (Y_2 - Y_1)(X_3 - X_1) \end{aligned} \quad (\text{B.4})$$

When the nodal coordinates in global axes are defined as follows ,

$$\{\Psi\} = \{X_1 \ Y_1 \ Z_1 \ X_2 \ Y_2 \ Z_2 \ X_3 \ Y_3 \ Z_3\} \quad (\text{B.5})$$

the derivatives of these unit vectors with respect to Ψ_j are

$$\frac{\partial\{l\}}{\partial\Psi_j} = \left[\begin{array}{c} \left(\frac{\partial c_x}{\partial\Psi_j} \right) \\ \left(\frac{\partial b_x}{\partial\Psi_j} \right) \\ \left(\frac{\partial a_x}{\partial\Psi_j} \right) \end{array} \right] \sqrt{c_x^2 + b_x^2 + a_x^2} - \left[\begin{array}{c} c_x \\ b_x \\ a_x \end{array} \right] \frac{c_x \frac{\partial c_x}{\partial\Psi_j} + b_x \frac{\partial b_x}{\partial\Psi_j} + a_x \frac{\partial a_x}{\partial\Psi_j}}{\sqrt{c_x^2 + b_x^2 + a_x^2}} \left\{ \frac{1}{c_x^2 + b_x^2 + a_x^2} \right\} \quad (\text{B.6})$$

$$\frac{\partial\{n\}}{\partial\Psi_j} = \left[\begin{array}{c} \left(\frac{\partial c_z}{\partial\Psi_j} \right) \\ \left(\frac{\partial b_z}{\partial\Psi_j} \right) \\ \left(\frac{\partial a_z}{\partial\Psi_j} \right) \end{array} \right] \sqrt{c_z^2 + b_z^2 + a_z^2} - \left[\begin{array}{c} c_z \\ b_z \\ a_z \end{array} \right] \frac{c_z \frac{\partial c_z}{\partial\Psi_j} + b_z \frac{\partial b_z}{\partial\Psi_j} + a_z \frac{\partial a_z}{\partial\Psi_j}}{\sqrt{c_z^2 + b_z^2 + a_z^2}} \left\{ \frac{1}{c_z^2 + b_z^2 + a_z^2} \right\} \quad (\text{B.7})$$

$$\frac{\partial\{m\}}{\partial\Psi_j} = \frac{\partial\{n\}}{\partial\Psi_j} \times \{l\} + \{n\} \times \frac{\partial\{l\}}{\partial\Psi_j} \quad (\text{B.8})$$

Since the three nodal coordinates in local axes are defined as

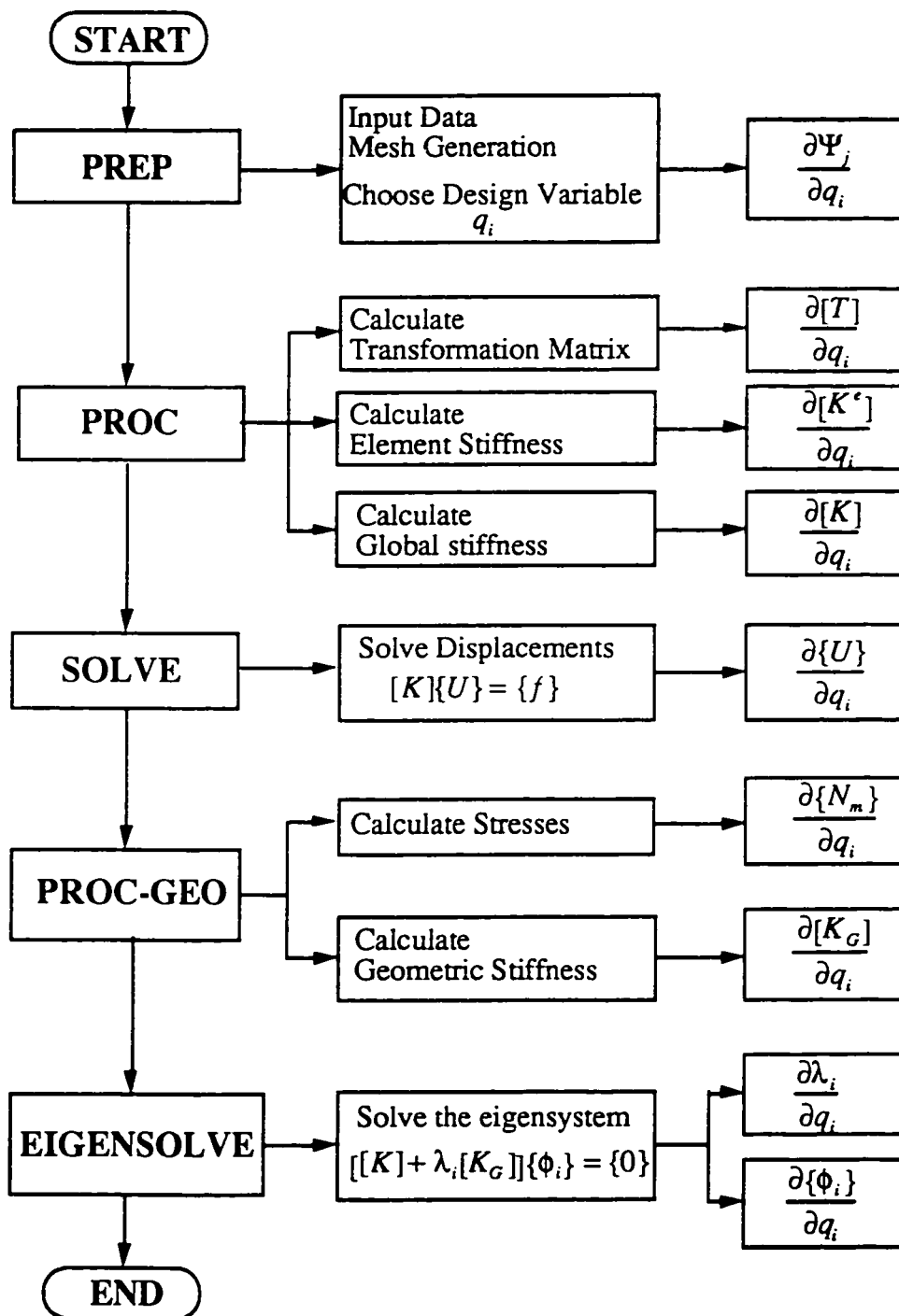
$$x_2 = \{l\}^T \{H\} \quad x_3 = \{l\}^T \{G\} \quad y_3 = \{m\}^T \{G\} \quad (\text{B.9})$$

Similarly, the derivatives of nodal coordinates in local axes with respect to Ψ_j are

$$\begin{aligned} \frac{\partial x_2}{\partial\Psi_j} &= \frac{\partial\{l\}^T}{\partial\Psi_j} \{H\} + \{l\}^T \frac{\partial\{H\}}{\partial\Psi_j} \\ \frac{\partial x_3}{\partial\Psi_j} &= \frac{\partial\{l\}^T}{\partial\Psi_j} \{G\} + \{l\}^T \frac{\partial\{G\}}{\partial\Psi_j} \\ \frac{\partial y_3}{\partial\Psi_j} &= \frac{\partial\{m\}^T}{\partial\Psi_j} \{G\} + \{m\}^T \frac{\partial\{G\}}{\partial\Psi_j} \end{aligned} \quad (\text{B.10})$$

Appendix C

Flow Chart



Appendix D

MATHEMATICA Code for Analytic Integrations

This appendix presents an example of the MATHEMATICA code developed to carry out the analytic integration. In this code, the explicit formulation of $[\bar{K}^m]$ in Eq.(4.8) is derived using the capability of MATHEMATICA for symbolic computations, and stored in an array "kmbar".

```
=====

bb=Table[0,{i,3},{j,14}];
x1=0; y1=0; y2=0;
x12=x1-x2; x13=x1-x3; x23=x2-x3; y13=y1-y3; y23=y2-y3;

plx={0,y23,-y13,2*y23*s,t*y23-s*y13,-2*y13*t,
      y23*(6 s^2+6 s t-3 t^2)-y13*(3 s^2-6s t -6 t^2)};
ply={0,-x23,x13,-2*x23*s,-t*x23+s x13,2 x13 t,
      -x23*(6 s^2+6 s t-3 t^2)+x13*(3 s^2-6s t -6 t^2)};

Do[ bb[[1,i]]=plx[[i]];
    bb[[2,i+7]]=-ply[[i]];
    bb[[3,i]]=ply[[i]];
    bb[[3,i+7]]=-plx[[i]] ,{i,1,7});

DM={{d1,d12,0},{d12,d2,0},{0,0,d3}};
test=Tp[bb].DM.bb;
intval={1/2,1!/3!,1!/3!,2!/4!,1! 1!/4!,2!/4!,3!/5!,2! 1!/5!,2! 1!/5!,3!/5!}
```

,4!/6!,3! 1!/6!,2! 2!/6!,3! 1!/6!,4!/6!);

```
result=Table[0,{i,14},{j,14}];
```

```
t=.;s=.
```

```
coe={1,s,t,s^2,s t,t^2,s^3,s^2 t,s t^2,t^3,s^4,s^3 t,s^2 t^2,s t^3,t^4};
```

```
Do[
```

```
  nt=Expand[test[[i,j]]];
```

```
  z=Table[0,{i,1,15}];
```

```
  z[[15]]=Coefficient[nt,t^4];
```

```
  z[[14]]=Coefficient[nt,s t^3];
```

```
  z[[13]]=Coefficient[nt,s^2 t^2];
```

```
  z[[12]]=Coefficient[nt,s^3 t];
```

```
  z[[11]]=Coefficient[nt,s^4];
```

```
  z[[10]]=Expand[Coefficient[nt,t^3]-z[[14]] s];
```

```
  z[[9]]=Coefficient[nt,s t^2];
```

```
  z[[8]]=Coefficient[nt,s^2 t];
```

```
  z[[7]]=Expand[Coefficient[nt,s^3]-z[[12]] t];
```

```
  z[[6]]=Expand[Coefficient[nt,t^2]-z[[9]] s-z[[13]] s^2];
```

```
  z[[5]]=Coefficient[nt,s t];
```

```
  z[[4]]=Expand[Coefficient[nt,s^2]-z[[8]] t-z[[13]] t^2];
```

```
  z[[3]]=Expand[Coefficient[nt,t]-z[[5]] s-z[[8]] s^2-z[[12]] s^3];
```

```
  z[[2]]=Expand[Coefficient[nt,s]-z[[5]] t-z[[9]] t^2-z[[14]] t^3];
```

```
  z[[1]]=Expand[nt-Sum[z[[i]]*coe[[i]],{i,2,15}];
```

```
  result[[i,j]]=Factor[z.intval];
```

```
  ,{i,1,14},{j,1,14}]
```

```
kmbar=result;
```

```
=====
```

VITA

Name: Youngwon Shin

Date of Birth: June 15, 1966

Place of Birth: Kwangju, Korea

Education

- Bachelor of Science: Department of Aeronautics, Seoul National University, February 1988
- Master of Science in Engineering: Department of Aeronautics, Seoul National University, February 1990
- Doctor of Philosophy: Department of Aeronautics and Astronautics, University of Washington, December 1997